Project THEMIS
Technical Report No. 16

Turbulent Flow Over a Wavy Boundary

by

P. S. Beebe and J. E. Cermak

This research project was
jointly sponsored by

U.S. Department of Interior
Office of Water Resources Research
Contract No. 14-01-0001

and

U.S. Department of Defense
Office of Naval Research
Contract No. N00014-68-A-0493-0001

Fluid Dynamics and Diffusion Laboratory
College of Engineering
Colorado State University
Fort Collins, Colorado

May 1972

CER71-72PSB-JEC44

ABSTRACT

TURBULENT FLOW OVER A WAVY BOUNDARY

An experimental study was made of turbulent flow over a wavy surface. Sinusoidal waves of three sizes were used to explore the variations of flow with wave size. Measurements of mean and turbulent velocities were taken with a two-wire method. Local heat transfer rates and pressures on the wavy surface were also measured.

An equilibrium turbulent boundary layer, which conforms to Rotta's and Clauser's self-preservation requirements, develops in the region far downstream from the first wave. In the lower portion of this layer, the mean velocity is represented by the logarithmic velocity profile when the form-drag measurements of skin friction are used to determine the shift-in-origin. The roughness function is related to the wave height since the wavy surface is shown to be a "k" type surface. The velocity defect profile in the logarithmic form extends to higher values of $yu_*/\delta^* U_\infty$ than those for smooth wall flows. Eddy viscosity results support the assumed logarithmic velocity variation in the lower part of the boundary layer. Measurements of shear stress by either the two-wire or the heated-film method disagree with the form drag measurements of skin friction.

The wavy surface is an extended surface windbreak since it reduces the overall wind speed above the surface and creates vortices between the waves. However, surface shear stresses are increased, and the erosion rate of field waves is a function of wave height.

TABLE OF CONTENTS

TABLE OF CONTENTS - (Continued)

TABLE OF CONTENTS - (Continued)

LIST OF TABLES

LIST OF FIGURES

LIST OF FIGURES - (Continued)

LIST OF FIGURES - (Continued)

LIST OF SYMBOLS

Symbol	Definition	Dimension
a	Wave amplitude	L
C_f	Skin friction coefficient	--
G	Clauser shape parameter	--
h	Wave height	L
H	Boundary layer shape parameter	--
k	Thermal conductivity	$HL^{-1}T^{-1}\Theta^{-1}$
K_m	Eddy viscosity	L^2T^{-1}
ℓ,L,W	Characteristic lengths	L
n,A,B	Hot-wire calibration constants	--
M,P	Heated-film calibration constants	--
p	Pressure	$ML^{-1}\,T^{-2}$
Pr	Prandtl number	--
T	Temperature	Θ
u,v	Velocity in x and y directions	LT^{-1}
u',v'	Fluctuations in u and v	LT^{-1}
$\tilde{u},\tilde{v}$	Wave-induced velocities	LT^{-1}
u_*	Friction velocity	LT^{-1}
U_{eff}	Effective hot-wire cooling velocity	LT^{-1}
x	Distance along wavy surface	L
y	Distance perpendicular to mean wave surface	L
z_o	Equivalent sand-grain roughness	L
α	Temperature-resistance coefficient	Θ^{-1}
β,γ	Angles in hot-wire response equations	--
δ	Total boundary layer thickness	L

Chapter I

INTRODUCTION

Turbulent flow over rough surfaces is a fundamental problem in mechanics, as these surfaces exist in nature and are created by man. Fluids flowing in piping systems, over river beds, open fields and cities all encounter surfaces which are rough. Practical considerations in man's efforts to control heat, mass and momentum transfer from many such rough surfaces provide the impetus to conduct basic, controlled studies of these turbulent flows. Two examples of rough surfaces where basic knowledge is needed are buildings in large urban areas, which affect pollution dispersion, and open fields, which allow soil erosion. The latter topic is the basis for part of this thesis.

Studying rough surface flows involves detailed analyses and measurements, but in addition, there are a myriad of surface geometries which could be investigated. For this thesis, a wavy (sinusoidal) surface was chosen. Wavy surfaces are a particular form of two-dimensional roughness with geometric parameters of wave-amplitude a and wave-length λ. Although flows over wavy surfaces have been investigated in the past (10,49,61), the primary interest was in studying mechanisms of water-wave generation (36,37). A basic study of a wavy surface modelling an open, corrugated (or micro-ridged) field has not been conducted. Besides providing fundamental understanding of rough surface turbulent boundary layers, such a study can also explore the potentials of micro-ridges as extended surface windbreaks.

Flow over a wavy (sinusoidal) surface is investigated in this thesis with the objectives of:

1. studying the wavy surface turbulent boundary layer,
2. correlating wavy surface results with other rough surface studies,
3. employing new measurement techniques to the flow in question, and
4. examining the potentials of wavy surfaces as surface windbreaks.

Previous experimental rough surface studies used sand, screens, and square-bar roughness elements (3,31,42,43), but a study of a wavy surface with steep waves had not been reported. In addition, analyses have not covered the case of a wavy surface which may generate "surface induced flows" (18,23,54). An aim of this study is to treat the wavy surface as a particular form of roughness, which requires new techniques for its analysis. Also, many waves (> 20) are used so that the flow will reach an equilibrium configuration, thus avoiding transitional flows (3,4).

1.1 Rough Surface Turbulent Boundary Layers

The classical study of flow over rough surfaces was conducted by Nikuradse (50) on sand-roughened pipe walls. Since then, the concept of equivalent sand grain roughness has been used to classify rough surfaces. However, very little distinction was made among flows over various types of surface roughnesses. Recently, more detailed experiments investigated flow over two-dimensional roughness elements of various spacings.

As in smooth wall experiments, velocities are compared to the logarithmic velocity profile. However, shear stress and origin shift are inter-related in the logarithmic profile and need to be determined independently of each other. Perry et al. (53) were able to classify rough surface flows into two broad areas: a "d" type characterized by flows skimming over the roughness elements, and a "k" type characterized by widely-spaced roughness elements. The second of these two types of flows has received the majority of experimental and theoretical analysis by Clauser (17,18), Doenecke (24), Betterman (8), Liu et al. (42), Antonia and Luxton (2,3,4), Perry and Joubert (52), and Hama (31). There are also isolated studies of closely-spaced roughness elements by Morris (48), Liu et al., and Perry et al.

In general, a typical roughness length k , or the equivalent sand grain roughness z_o ($\simeq k/30$) was used to describe a rough surface. However, Perry et al. showed that closely spaced roughness elements can <u>not</u> be characterized by the roughness size k , but should be classified by the origin shift εk . More detailed analyses will help clarify the important parameters of rough surface flows so that computational schemes can be extended to any surface geometry.

1.2 Measurement Techniques

Two principal sets of measurements are conducted in this study. One set consists of wall shear stress and the other consists of mean and turbulent velocity measurements. The combination of these two measurement sets aides in understanding rough wall flow and its relationship to other turbulence studies.

1.2.1 <u>Shear Stress Measurements</u> - Previous turbulent boundary layer studies relied on indirect measurements of wall shear stress (21,31). Using the logarithmic velocity profile, these methods assume a priori the location of the origin for vertical distances. Thus, the shear stress is dependent on the choice of origin. Recently Perry et al. (53) and Antonia and Luxton (3,4) used a method which is independent of velocity profile assumptions or origin locations. This method involves measurements of form drag on separate roughness elements and was used to obtain data for this thesis. In addition, a small heated film provided a second method of determining the surface shear stress. The use of a heated film in turbulent flow measurements was documented by Bellhouse and Schultz (6,7) and Brown(11).

1.2.2 Turbulence Measurements - Mean and turbulent velocity profile measurements were obtained using a new, two-wire technique (36) which did not rely on linear response assumptions. This method allows the measurement of flow fields with large magnitude and direction changes. Very few turbulence measurements have been made in other rough wall turbulent boundary layer studies. Logan and Jones (43), Corrsin and Kistler (21) and Antonia and Luxton provide the few studies available for reference and comparison.

1.3 Surface Windbreaks

A wavy surface turbulent boundary layer can be used to study the atmospheric surface layer flow over an open field (55). Open, windswept fields are very suseptible to wind erosion (15), and any obstacle which retards the general flow field will reduce the destructive force of the wind. Usually, rows of trees, fences, or hedges are used to reduce wind force on crops (16,25,41). However, successive rows of such obstacles are needed to maintain the windbreak's "effective zone of influence" over large areas (22,66). Recently, the concept roughening the ground to prevent soil and snow from blowing was used (15). These "surface windbreaks" act to reduce further the wind velocity between major windbreaks, such as tree rows.

The potential of this type of surface windbreak was established by Marlatt and Hyder (47). However, a more detailed study is necessary to clarify the important features of surface windbreaks. Hsu (34) demonstrated the importance of wind shear on sand transport, since surface shear stress starts the soil moving. A wind-tunnel study will provide basic information about the flow structure. This information can be used for design input; but it still may be difficult to tailor a wavy surface to a particular field application.

Chapter II

THEORETICAL AND EMPIRICAL BACKGROUND

This chapter outlines the equations of motion from which theoretical and empirical correlations have been developed for turbulent flow over any boundary. Particular attention is given to the logarithmic velocity profile for equilibrium layers over various rough surfaces and to the correct determination of shear stress. The variation of shear stress near a wavy surface is discussed with its relation to eddy viscosity and the logarithmic velocity profile. The local similarity concept is also reviewed.

2.1 General Equations of Motion

The turbulent boundary layer equations for steady two-dimensional mean flow are (57)

$$\bar{u}\,\frac{\partial \bar{u}}{\partial x} + \bar{v}\,\frac{\partial \bar{u}}{\partial y} = -\frac{1}{\rho}\frac{\partial p}{\partial x} + \nu\,\frac{\partial^2 \bar{u}}{\partial y^2} - \frac{\partial(\overline{u'v'})}{\partial y} - \frac{\partial(\overline{u'^2} - \overline{v'^2})}{\partial x} \quad , \tag{2.1}$$

$$p/\rho = (p_\infty/\rho) - \overline{v'^2} \quad , \tag{2.2}$$

and

$$\frac{\partial \bar{u}}{\partial x} + \frac{\partial \bar{v}}{\partial y} = 0 \quad , \tag{2.3}$$

where an overbar represents time averaging. Turbulent velocity components are represented by u' and v' . Total shear stress acting on a horizontal layer of fluid is

$$\tau = -\rho\,\overline{u'v'} + \mu\,\frac{\partial \bar{u}}{\partial y} \quad . \tag{2.4}$$

Except for small distances above surfaces, $-\rho\,\overline{u'v'} \gg \mu \frac{\partial \bar{u}}{\partial y}$. The Reynolds stress terms in the equations of motion ($-\rho\overline{u'v'}$, $\overline{u'^2}$, $\overline{v'^2}$) prevent a deductive analytical solution.

If the bounding surface is wavy, an additional shear stress may be created (54). This stress is called a surface-induced shear stress and is given by

$$\tau_s = -\rho\tilde{u}\tilde{v} \quad , \tag{2.5}$$

where $\tilde{u}$ and $\tilde{v}$ are surface-induced velocities such that

$$\int_x^{x+\lambda} \tilde{u}\,dx' = \int_x^{x+\lambda} \tilde{v}\,dx' = 0 \tag{2.6}$$

for any elevation y above the wavy surface. Velocities $\tilde{u}$ and $\tilde{v}$ decay rapidly above the wavy surface. The addition of this shear gives

$$\tau = -\rho\overline{u'v'} - \rho\,\tilde{u}\tilde{v} \quad . \tag{2.7}$$

The importance of the surface-induced shear stress is well established for moving water waves (36), but not for stationary roughened surfaces.

2.2 Boundary-Layer Flows over a Rough Wall

Turbulent shear flow considered in two dimensions and with steady mean velocities can be represented by the "law of the wall" for a considerable region near the smooth wall where $y = 0$:

$$\bar{u}/u_* = f(yu_*/\nu) \quad , \tag{2.8}$$

where u_* is called the shear velocity and is equal to $(\tau/\rho)^{\frac{1}{2}}$, where τ is the wall shear stress (20). For values of $yu_*/\nu > 50$, the universal law becomes

$$\bar{u}/u_* = (1/\kappa) \ln \frac{yu_*}{\nu} + C_1 \tag{2.9}$$

where κ and C_1 are experimentally determined constants. The derivation of the logarithmic law above can be accomplished by several methods. Malkus (46) used dimensional arguments, while assumptions involving a region of constant stress near the wall were used by van Driest (23) and Reichardt (35). Coles (19) suggested that the "law of the wall" be expanded to include a function

$$h(x,y) = \frac{\Pi}{\kappa} w(y/\delta) \tag{2.10}$$

which would describe the flow outside of the logarithmic portion. Normally the logarithmic region is less than 0.2 times the total boundary-layer thickness. The logarithmic velocity profile can not be deduced from the turbulent boundary layer equations, but is an experimentally verified correlation (19).

The value of u_* or $u_*/U_\infty = \sqrt{C_f/2}$ plays a very important role in the turbulent boundary layer, since the wall shear stress extracts energy from the turbulent boundary layer. Also, all length ratios in a turbulent shear flow are dependent on the value of $\sqrt{C_f/2}$ since

$$\delta^* = \sqrt{C_f/2}\,\Delta \tag{2.11}$$

and $$\theta = \delta^*(1 - G\sqrt{C_f/2}), \tag{2.12}$$

where $$\Delta = \delta \int_0^\infty \frac{(U_\infty - \bar{u})}{u_*}\, d\left(\frac{y}{\delta}\right) \tag{2.13}$$

and $$G = \int_0^\infty \frac{(\bar{u} - U_\infty)^2}{{u_*}^2}\, d\left(\frac{y}{\Delta}\right) \tag{2.14}$$

The length Δ is determined from the profile of the velocity defect

$(U_\infty - \bar{u})/u_*$ vs. y/δ , and the parameter G is a shape factor which will be discussed in Section 2.3.

Introducing roughness at the wall increases wall friction. Consequently, the logarithmic wall law is shifted downward and to the right (Fig. 1). Roughness changes the wall law to

$$\bar{u}/u_* = A \ln \frac{yu_*}{\nu} + C - \frac{\Delta u}{u_*} \quad , \tag{2.15}$$

where $\Delta u/u_*$ is called the roughness function and measures the shift of the logarithmic velocity profile. For fully rough flow (viscous stresses negligible), the logarithmic law must be independent of the viscosity; thus Eq. (2.15) gives

$$\Delta u/u_* = A \ln \frac{ku_*}{\nu} + D \quad , \tag{2.16}$$

where k specifies a size of the roughness. The form of the roughness function above was first given by Clauser (15) and was used in many studies (8,31,42,52). Roughness elements used in these studies were screens or square bars perpendicular to the mean flow.

Recently, Perry et al. (53) extended the analysis of rough wall flows to cover roughness elements of various spacings, as opposed to the previous concept of simple "roughness". Their analysis proceeds along the following lines (See Fig. 2). The inner flow is characterized by a velocity u_* and a roughness length k such that

$$\bar{u}/u_* = f(y/k) \quad . \tag{2.17}$$

Flow further away from the wall is assumed to follow the logarithmic law:

$$\frac{\bar{u}}{u_*} = \frac{1}{\kappa} \ln \left[\frac{(y_T + \varepsilon k)}{\nu} u_*\right] - \frac{\Delta u}{u_*} + A \quad , \tag{2.18}$$

where εk is an "origin shift" for displacement y_T. At some distance above the surface, these velocities blend along a horizontal line. Equating velocities at $y_T = \alpha k$ then gives

$$\frac{\Delta u}{u_*} = \frac{1}{\kappa} \ln \left[\frac{u_*(\alpha k + \varepsilon k)}{\nu}\right] + C_1 \tag{2.19}$$

Equating velocity derivatives from Eqs. (2.17) and (2.18) gives ε proportional to α . Thus

$$\frac{\Delta u}{u_*} = \frac{1}{\kappa} \ln \frac{k u_*}{\nu} + C_2 \quad , \tag{2.20}$$

where C_2 is a new constant. A surface which gives $\Delta u/u_* \propto \ln k$ is called a "k" type surface by Perry et al. (53). Such a surface is characterized by widely spaced roughness elements, or roughness elements which do not trap vortices between themselves.

For closely spaced roughness elements, or rough surfaces which trap vortices between the roughness elements, the flow "skims" over the elements which do not protrude into the boundary layer flow. For such flows, α would be expected to be small. Thus, for $\alpha \rightarrow 0$,

$$\frac{\Delta u}{u_*} = \frac{1}{\kappa} \ln \frac{\varepsilon k u_*}{\nu} + C_1 \quad . \tag{2.21}$$

Given any rough surface, the dependence of $\Delta u/u_*$ on the roughness size, shape or orientation can not be predicted. For shallow waves or roughness elements with wide spacing, the roughness function may be related to the wave height h which could then be substituted for length k in the above equations.

However, as the waves are made steeper for a given wavelength, or shorter for a given height, the roughness function may become a function of the origin shift εh . Thus, one objective of this study is to determine the relationship between roughness function and roughness length for wavy surfaces.

For smooth wall turbulent boundary layer flows, there is no origin shift εh . Friction velocities can then be determined by various methods (59). Roughening the surface introduces an indeterminate origin for y . If the slope of the line u vs. $\ln y$ is used to determine u_* , arbitrary choices of the y-origin result in arbitrary friction velocities. The momentum integral equation could be used to determine u_* , but momentum integrals may give unreliable estimates of wall friction. Perry and Joubert (52) used two other approaches: a wake-alignment method for adverse pressure gradient flows and an "approximate" method (trial and error). Their conclusion was that a better method is desirable.

Measurements of u_* independent of εh are needed. One method used (3,53) involves measurement of the "form drag" of one roughness element. Referring to Fig. 3, the shear stress τ_e is related to the form drag by the x-momentum balance

$$\frac{\tau_e}{\frac{1}{2}\rho U_\infty^2} \cong \frac{1}{\lambda}\int \frac{p_w\ \hat{n}\cdot\hat{\imath}}{\frac{1}{2}\rho U_\infty^2}\, ds \tag{2.22}$$

where the integration of the wall pressure p_w is taken over the wave surface S . The flow pattern in two successive wave troughs is assumed to be the same, so the integration does not involve momentum fluxes across surfaces AB and CD. Also, frictional forces are assumed to be negligible compared to pressure forces along the surface.

Shear stress τ_e is the "effective shear stress" acting over one wavelength. If the mean streamlines are wavy, effective shear stress τ_e contains the average over one wavelength of the surface induced Reynolds stress $-\rho\tilde{u}\tilde{v}$;

$$\tau_e = \langle -u'v' \rangle + \langle -\rho\, \tilde{u}\tilde{v} \rangle \quad , \tag{2.23}$$

where $\langle\ \rangle$ represents an average over one wavelength. If surface BC is close to the wave crests, $\langle -\rho\, \tilde{u}\tilde{v} \rangle$ may contribute substantially to τ_e.

Using τ_e, effective friction coefficients C_f are determined such that $C_f = \tau_e/\frac{1}{2}\rho U_\infty^2$. The logarithmic velocity profile can be written as

$$\frac{\bar{u}}{u_\infty} = \sqrt{C_f/2}\,\left[\frac{1}{\kappa} \ln \frac{(y_T + \varepsilon h)u_*}{\nu} + A - \frac{\Delta u}{u_*}\right] \tag{2.24}$$

so that the origin shift εh is not arbitrary. The slope of the logarithmic profile is then fixed and ε can be easily determined. When the data $(u/U_\infty$ vs. $y_T + \varepsilon h)$ gives a straight line of slope $(1/\kappa)\sqrt{C_f/2}$ for $(y_T + \varepsilon h)/\delta < 0.2$, the "correct" value of ε has been determined. Thus, the form drag method for measuring u_* provides a means of removing the ambiguity in defining the origin shift.

The eddy viscosity is defined as

$$K = \frac{\tau/\rho}{\partial u/\partial y} \quad , \tag{2.25}$$

analogous to the kinematic viscosity (44). Since K has dimensions of velocity times length, assuming $K = \kappa u_* y$ gives

$$u = \frac{1}{\kappa} u_* \ln y + \text{constant} \quad , \tag{2.26}$$

where u_* is the friction velocity, y is the distance above the surface, and κ is an empirical constant. For rough surfaces, the origin of y is not known; but if the ratio $(\tau/\rho)/(\partial u/\partial y)$ varies linearly with distance above the surface, then the velocity will vary with $\ln(y_T + \varepsilon h)$, where εh is an origin shift for y. The variation of K with height can be determined from the direct measurements of τ and $\partial u/\partial y$. Thus, the logarithmic velocity profile assumptions can be verified.

2.3 Similarity Requirements

Similarity solutions to the boundary layer equations result in profiles which are similar in shape after proper scaling by a velocity and a length. These profiles are also called equilibrium solutions. Clauser (18) showed that velocity profiles which have a shape parameter G independent of distance x are equilibrium profiles. Shape parameter G is given by

$$G = \int_0^\infty [(U_\infty - \bar{u})^2/u_*^2]\, d(y/\Delta) \tag{2.27}$$

with

$$\Delta = \int_0^\infty [(U_\infty - \bar{u})/u_*]\, dy \quad . \tag{2.28}$$

Rotta (57) also analyzed the parameters which give equilibrium profiles for the turbulent boundary layer. For equilibrium profiles, he showed that the following must hold:

$$u_*/U_\infty = \text{constant} \quad , \tag{2.29}$$

$$\frac{d}{dx}\left(\frac{U_\infty \delta^*}{u_*}\right) = \text{constant} \quad , \tag{2.30}$$

and
$$\frac{\delta^*}{\tau_w}\frac{dp}{dx} = \text{constant} \quad . \tag{2.31}$$

A wavy surface meets the above three conditions if $U_\infty \propto (x - x_o)^m$ with $m > 0$ and the surface is "rough", or if $U_\infty \propto \exp[\mu(x - x_o)]$ with $\mu > 0$ and the waves are of constant height.

If a turbulent boundary layer is an equilibrium layer, then universal relations can be established for the variation of mean velocity and Reynolds shear and normal stresses. The turbulent flow over the wavy surface will be compared to the equilibrium conditions to clarify the universal relations which presently exist for rough surface flows.

2.4 Turbulence in Boundary Layers

Turbulent intensities, $\sqrt{\overline{u'^2}}/U_\infty$ and $\sqrt{\overline{v'^2}}/U_\infty$, and the turbulent shear stress, $-\rho\overline{u'v'}$, can be determined from the complete solution of the averaged Navier-Stokes equation. Since a complete solution is not available, empirical correlations which relate to other measured quantities are used. The intensities for turbulent boundary layers over rough surfaces have rarely been reported, and empirical correlations do not exist. However, solution of the equation

$$\bar{u}\frac{\partial \bar{u}}{\partial x} + \bar{v}\frac{\partial \bar{u}}{\partial y} = \frac{\partial(-\overline{u'v'})}{\partial y} \tag{2.32}$$

by Townsend (64) gives

$$-\overline{u'v'} = u_*^2 \exp\left[-b(y/\delta)^2\right] \tag{2.33}$$

where $$b = \frac{\delta U_\infty}{2K} \frac{d\delta}{dx} , \qquad (2.34)$$

and the velocity defect is assumed to be a function of y/δ only; that is

$$\frac{U_\infty - \bar{u}}{u_*} = f(y/\delta) \quad . \qquad (2.35)$$

However, this particular solution may not be applicable to rough wall studies since the velocity defect may not be a function of y/δ near the surface (18). Klebanoff's measurements (39) give the value of $b = 1.77$. The same value was obtained by Liu et al. (41) for flow over square-bar roughness elements.

The shear stress profile above a smooth wall was obtained by Coles (20) using the universal law. The shear stress is given by

$$\frac{\tau}{\tau_w} = 1 + \frac{1}{u_*^2} \int (\bar{u} \frac{\partial \bar{u}}{\partial x} + \bar{v} \frac{\partial \bar{u}}{\partial y}) \, dy \quad . \qquad (2.36)$$

The logarithmic velocity profile

$$\frac{\bar{u}}{u_*} = \frac{1}{\kappa} \ln \left(\frac{u_* y}{\nu}\right) + 5.1 + \frac{\Pi}{\kappa} w(y/\delta) \quad , \qquad (2.38)$$

where $w(y/\delta)$ is the wake function, and the velocity defect profile

$$\frac{U_\infty - \bar{u}}{u_*} = -\frac{1}{\kappa} \ln \frac{y u_*}{\nu} + 1.38 \, [2 - w(y/\delta)] \quad , \qquad (2.38)$$

are substituted into Eq. (2.36). From the above three equations, the shear stress is determined for a smooth wall flow.

The aim here is not to discuss analyses for smooth wall flows, but rather to show that very little has been done on rough wall studies. Even in Rotta's extensive paper (57), rough wall analyses are discussed only briefly. Before smooth wall analyses are carried over to the wavy surface flow, the basic assumptions underlying the analyses must be tested. Such testing is an important part of this study.

2.5 Summary

The theoretical and empirical correlations given in this chapter emphasize the need for performing careful experiments on rough wall flows. Then, analyses can be conducted with as firm a basis as smooth wall analyses and computations schemes are conducted today. To that objective, a wavy surface is examined in a thick turbulent boundary layer.

Chapter III

EXPERIMENTAL APPARATUS AND PROCEDURES

The apparatus, instrumentation, calibrations, and procedures used in the experiment are described in this chapter. Two principal sets of measurements were involved: measurements of heat flux and pressure on the wavy surface, and mean and turbulent velocity measurements above the waves.

3.1 Waves

The wave forms selected were sinusoidal, with constant wavelength of 4.2 in and amplitudes of 0.85 in (wave A), 0.5 in (wave B), and 0.25 in (wave C). Each wave was milled from styrofoam with a mill-head cutter. A cross-sectional view of the waves, a mill-head cutter, and a plexiglas wave form used to determine fractional wave positions is shown in Fig. 4.

3.2 Wind Tunnel

The experimentation was conducted in the C.S.U. low-speed wind tunnel with a test section length of 30 ft and a cross sectional area 6 ft by 6 ft (see Fig. 5). Modifications made in the tunnel are shown in Fig. 6. A false floor made of plywood was placed 4 in above the wind tunnel floor so that the mean wave surface was at false floor level. A row of 1 in wire brushes was placed at the upstream end of the tunnel to thicken the boundary layer on the floor, and an aluminum sheet was attached upstream from the brushes to smooth flow from the tunnel contraction. A plywood sheet was fitted to the last wave trough to smooth transitional flow. The waves began approximately 22 ft from the brushes. All joints and edges were taped for continuity, and the entire wave surface was covered with felt to insure uniformity. Measurements were made at positions corresponding to the -5th, 1st, 5th, 10th, 15th, 20th, 24th, 25th, and 27th crest. (Fig. 6).

3.3 Wall Pressure

Wall pressure was measured by a 1/32 in dia pressure tap placed at various positions on the 27th wave with free stream static pressure above the wave crest as reference. Pressure differences (between free stream and wall, or across a pitot-static tube) were measured by a calibrated M.K.S. Baratron pressure meter, type 77. Total horizontal force was also measured on the 26th, 27th, and 28th wave of each wave size with a floating-plate strain-gage balance developed by Hsi and Nath (33).

3.4 Wall Heat Flux

Wall heat flux was measured by a point source of heat using a Disa 55A90 flush-mounted film (1 mm x 0.2 mm) operated at a small overheat by a Disa 55D01 constant resistance anemometer. The overheat ΔT equals the difference between the film temperature, T_f , (assumed constant on the film surface) and ambient temperature, T_a . The overheat was usually set between 15° and 45° C. The resistance ratio R_h/R_c was determined for a specific overheat by

$$R_h/R_c = 1 + \alpha\, \Delta T \quad , \tag{3.1}$$

where R_h and R_c are respectively the hot and cold resistances and α is the temperature-resistance coefficient equal to 0.3%/°C (calibrated). Ambient temperature of the tunnel air was measured by a Yellow Springs Tele-Thermometer Model 405.

3.5 Shear Stress Measurements

The flush-mounted heated film can be used to measure wall shear stress. Bellhouse and Schultz (6,7) and Brown (11) showed that the calibration relating shear stress and heat flux is

$$I^2R/\Delta T = M\,\tau^{1/3} + P \tag{3.2}$$

for zero pressure gradient flows. Brown extended the calibration to flows with a pressure gradient, and the calibration changes to

$$\tau + K\,\frac{dp}{dx}\left(\frac{\Delta T}{I^2R}\right) = M'\left(\frac{I^2\,R}{\Delta T}\right)^3 \tag{3.3}$$

For measurements on the wavy surface, a calibration was obtained by mounting the film to a circular cylinder. The film was first mounted in a sheet of rubber gasket material so that the substrate of the film would be the same on both the cylinder and the waves. Using this procedure, the calibration should not change when the film is moved from the cylinder to the waves. The Reynolds number for the calibration flow was 1×10^5 , and average values of shear stress τ on the cylinder were taken from several sources (1,27,58,60). (see Table 1).

Two typical calibrations are shown in Fig. 7. The intercept P is a function of the overheat ΔT . Thus, instead of calibrating the films as $I^2R/\Delta T$ vs. $\tau^{1/3}$, the calibration relation was rewritten as

$$I^2R = \tau^{1/3}\;(A + B\Delta T + C(\Delta T)^2) + (D + E\Delta T + F(\Delta T)^2)\;. \tag{3.4}$$

The film calibration is then a function of the overheat ΔT and the shear stress $\tau^{1/3}$. For a series of I^2R , ΔT and $\tau^{\frac{1}{3}}$ values, coefficients A, B, C, D, E and F can be determined. Least-square estimates of the coefficients ($\pm$10%) are:

$$A = -3.9 \times 10^{-2} \qquad D = 7.0 \times 10^{-2}$$

$$B = 5.6 \times 10^{-3} \qquad E = 5.7 \times 10^{-4}$$

$$C = -8.0 \times 10^{-5} \qquad F = 1.5 \times 10^{-5} \quad .$$

The calibration relation and coefficients above are for the Disa probe and for $15^\circ < \Delta T < 45^\circ C$ only. A procedure similar to the one above was used by Bellhouse and Schultz (6) for calibrating films.

The slope of the calibration is (11)

$$M = kW[(\rho\ Pr)/(1.9\ \mu^2)]^{\frac{1}{3}}\ L^{\frac{2}{3}} \quad , \qquad (3.5)$$

where L and W are respectively the streamwise length and lateral width of the film surface. The effective length Le for transferring heat to the fluid may not be the same as the physical length of the film surface. However, if the slope M from a calibration is known, the effective length can be determined from Eq. (3.5). Using a typical slope of $M = 2 \times 10^{-3}$ (watts/°C)/psf and $We/W \simeq Le/L$, $Le = 2L$, in agreement with Brown (11). In addition, the slope M is a weak function of temperature (6) and the coefficient of $\tau^{\frac{1}{3}}$, $A + B\Delta T + C(\Delta T)^2$, gives the correct variation of M with temperature.

3.6 Mean Velocity and Turbulence Measurements

Mean velocity was measured by pitot-static tubes and a M K.S. Baratron pressure meter. One 1/8 in O.D. tube was placed 35 wavelengths upstream of the waves for reference velocity monitoring. A second 1/16 in O.D. tube was moved vertically on the tunnel carriage to determine velocity profiles. The mean and turbulent velocity components above the waves were also measured with a two-wire probe (Flow Corporation Model 23) in conjunction with Disa 55D01 anemometers. The wires were tungsten with $d = 0.00035$ in and $\ell = 0.040$ in. The hot-wire probe and pitot-static tubes are shown in Fig. 8.

The velocities from the hot wires were determined by the following technique (see Fig. 9). The calibration of the wires is $I^2R/\Delta T$ vs. U , where U is the velocity measured by a pitot-static tube. Typical calibrations are given in Fig. 10. The hot-wires were approximately $\pm$ 45° from a horizontal reference line, as shown in Fig. 9. The instantaneous values of $I^2R/\Delta T$ were determined by the recorded signals of each wire. Here I is the total current through a wire of operating resistance R , and ΔT is the overheat in °C. The cooling relation

$$I^2R/\Delta T = B\, U^n_{eff} + A \tag{3.6}$$

was assumed to apply instantaneously so that the velocity U_{eff} could be determined for every value of $I^2R/\Delta T$ for each wire. The same technique was used by Frenkiel and Klebanoff (28) for grid turbulence and by Karaki and Hsu (36) for wind water-wave turbulence measurements.

The effective cooling velocity for a wire is

$$U^2_{eff} = U^2(\sin^2\beta + k^2 \cos^2\beta) \quad , \tag{3.7}$$

where U is the total velocity. Equation (3.7) is accurate to terms of order k^4 (14). A calibration of U_{eff} vs. β at a constant value of U gave a k value of 0.33 ± 0.03 . This value of k agrees well with values reported by Champagne et al. (13) for wires with length-to-diameter ratios of 110. The values of A, B, and n were determined for each calibration.

Using Eq. (3.7) restricts the angle β to $20^\circ < \beta < 160^\circ$ for each wire, and for the two wires used here, the velocity vector must remain in a 50° cone between the wires. Any data set which contained a velocity vector outside of this cone was disregarded, which placed an upper limit on the turbulent intensity that can be measured by this procedure.

At a particular instant, the values of U and β_1 (or β_2) are determined by a procedure given in Appendix A. Instantaneous values of u and v are then calculated. Subsequently, the turbulent values of $u' = u - \overline{u}$ and $v' = v - \overline{v}$ are obtained. (An overbar represents temporal averaging.) The maximum vertical intensity is then

$$v'/u = \tan 25^\circ = 0.47 \quad . \tag{3.8}$$

There is no analogous upper physical limit to u'/u, but Freymuth (29) showed that u'/u is limited to approximately 0.64 by the electronic response of the anemometer amplifiers.

3.7 Analog-to-Digital Conversion

Voltages from the anemometers were recorded using an Ampex FR 1300 tape recorder at 15 ips. A schematic showing the data collection method is given in Fig. 11. Recordings were made of both the AC and the total voltage signals from each anemometer. Data were also recorded using a root-mean-square meter and a digital voltmeter for cross-checking purposes.

The analog signals were later digitized at 4000 samples/sec, a rate sufficiently high to avoid aliasing the energy spectrum (9,26, 63). For most profiles, the record length was 6.5 sec for both digitizing and computation cost reasons. However, longer records (19.5 sec) were taken for selected data. The length of digitized record needed to establish stable statistics was difficult to determine a priori, and the problem of stable velocity values will be discussed in Chapter IV.

Chapter IV

RESULTS AND DISCUSSION

Turbulent boundary layer flow over a wavy surface is discussed in this chapter. Two principal sets of measurements are presented: measurements directly related to the wavy surface, and measurements of the turbulent boundary layer flow. The inter-relationship between these measurement sets is examined; wavy surface results and other rough wall turbulent boundary layer results are compared; and the windbreak effect of the wavy surface is discussed.

Part 1: Wall Measurements

4.1 Flow Pattern Between Waves

Observations of the flow pattern were first made on the wave set with the largest amplitude, wave A, and then on the set with the smallest amplitude, wave C, to obtain a qualitative comparison of pattern characteristics. The pattern between waves was visualized by releasing titanium tetrachloride smoke into the air flow near the wave surface. The pattern observed consisted of a single, slowly-rotating vortex as indicated in Figs. 12 and 13. Flow in this vortex was unsteady, and most important, sections of the vortex along the trough were shed into the flow above the waves.

For wave A, the vortex fills the area between crests so that the flow "skims" over the waves. The streamline pattern for the vortex of wave A is suggested in Fig. 14. Area "a" is the most unsteady region of flow between the crests. Flow re-attaches to the wave in this area and makes pressure measurements difficult. The vortex is generally in area "v". Area "s" is very close to the wave crest and is the region where flow separates from the surface, as shown in Fig. 12 The vortex of wave A completely fills the trough (flow above the wave does not penetrate into the trough), so the flow "skims" over the wave crests. Such a flow fits the definition of "skimming" flow established by Morris (48) and Liu et al. (42). Flow over wave A also fits the definition of "k" type flow given by Perry et al. (53), as the vortices are intermittently shed. The analysis of the roughness function given in Section 2.2 then suggests that the roughness length "k", or more presisely the wave amplitude a, is the important length for the boundary layer flow. Extrapolating from the observations of flow over wave A, a wave with $a/\lambda >> 0.2$ would provide increased windbreak protection by trapping vortices between the waves.

The vortex of wave C is smaller than that of wave A (see Fig. 13), and it forms and sheds intermittently along the trough. In areas where a vortex does not exist, the boundary layer flow appears (qualitatively) to follow the wave contour. Therefore, the boundary layer flow for wave C is characterized by the length "k" and cannot be characterized as a "skimming" flow. Qualitatively, vortices are shed into the boundary layer more frequently from wave C than from wave A. However, no estimate of vortex shedding frequency can be made for the wave surface. The implications of vortex shedding will be discussed further in conjunction with mean velocity profile results in Section 4.7.3.

4.2 Wall-Pressure Profiles and Drag Measurements

Surface pressure variations are produced when a turbulent boundary layer gives rise to vortices between wave crests. The resulting wall-pressure profiles for waves A and C are shown in Fig. 15. (No pressure measurements were taken for wave B). Pressure coefficients, defined as

$$C_p = (p_w - p_\infty)/(\rho U_\infty^2/2) \quad , \tag{4.1}$$

are essentially the same over the wave surface for $U_\infty = 10$, 20, and 40 fps, indicating a fully developed flow at these velocities. Pressures were measured on the 27th wave.

Flow separates shortly after each wave crest and p_w decreases; flow then re-attaches before the next crest, and p_w increases. The pressure peak in p_w on wave C moves upstream relative to its position on wave A. This result suggests that the vortex for wave C is smaller than that for wave A. Thus, the results of wall pressure profiles and smoke visualization are consistent on the existence of a vortex and its relative size between the two wave sizes.

The "effective shear stress", τ_e , a small distance above the wave crests, is obtained by integrating the measured wall pressures over one wavelength. The assumptions for this method of τ_e determination are discussed in Section 2.2. The resulting values of C_f are given in Table 2. Included also are the values obtained by mounting the 26th, 27th, and 28th waves on a strain-gage balance. These two sets of C_f values agree within 25%. Form drag and total drag measured by the strain gage balance should agree very closely for separated flow between wave crests.

The spread in C_f values for several repeat measurements is approximately $\pm$ 5% from the mean value. Thus, the form drag results show that C_f measurements are repeatable. This last observation is further confirmed by comparing the C_f values obtained by Verma (65) to the present measurements. The values differ by less than 10%. The experiments reported in this thesis involved a reinstallation of the apparatus used by Verma and so are a true repeat check of the measurements. These values of C_f are relatively large and ranged from 0.01 for wave C to 0.02 for wave A. The only other results for fully-developed rough wall turbulent boundary layers available for comparison were approximately one-half the values reported here, but the comparison values were for square-bar roughness elements. Perry et al. (53) reported a value of 0.005; Antonia and Luxton (3) and Liu et al. (42) reported C_f values of 0.008.

4.3 Wall Heat Flux

Heat loss from a point-source was measured using the surface-mounted heated film. The film was moved along the surface of the waves to record the variation of heat loss shown in Fig. 16. The Nusselt number is

$$Nu = \frac{(I^2R/A)\ell}{k\ \Delta T}\ , \tag{4.2}$$

where A is the film area (1 mm x 0.2 mm) and length ℓ was arbitrarily chosen as the film width (1 mm). Since the film is operated at a low overheat (see Section 3.4), approximately 80% of the heat loss is caused by free convection from the film.

The vortex between the waves removes heat from the film, causing almost uniform Nusselt numbers over the wave surface. Comparison of these numbers with the Nusselt number variations given by Kolar (40), Nunner (51), and Webb et al. (66) is difficult. Their correlations of Nusselt number with roughness Reynolds numbers are for area sources of heat, while the measurements in this experiment are for point sources of heat. Other point-source heat-loss measurements for rough wall flows have not been reported, and may not be of physical significance. The wavy surface is a model of a micro-ridged field and there would be no natural equivalent to a point source of heat. Point-source measurements of heat loss are necessary for calculation of the surface shear stress.

4.4 Wall Shear Stress

The heated film was used in this study primarily as a method of measuring wall shear stress, and secondarily as a measure of heat flux. The calibration relating wall heat flux and shear stress was discussed in Section 3.5. Local "friction coefficients" are obtained from the calibration and the heat loss profiles. The skin friction on wave A, derived from the Nusselt number variations shown in Fig. 16, is shown in Fig. 17. The vortex between the crests removes as much heat as the flow skimming over the wave crests. Consequently, the "shear stresses" reported in the trough area are as large as the stresses at the wave crest. Shear stresses in the trough area are probably very small since flows in the troughs are weak (38), and the hot film does not give reliable measurements in this area. For the flow near the crest where the velocity skims over the surface, the hot film measures C_f values of approximately 0.01. The uncertainty in these measurements is of the order of $\pm$ 15% when the calibration procedure is taken into account. Caution must be expressed here as to the application of the calibration obtained on a circular cylinder to the highly turbulent wavy surface flow. Bellhouse and Schultz (7) suggested that flush-mounted films may give low values of shear stress in turbulent flows when the static calibration is used to relate heat loss and shear stress. However, the degree to which films are affected by velocity fluctuations has not yet been determined. Thus, no corrections were used with the calibrations to account for any fluctuations.

The C_f values from the heat flux measurements for wave C are shown in Fig. 18. Kendall's values (37) are also shown in Fig. 18 for comparison. Kendall presented skin friction variations over a shallow wave similar to wave C. The important part of the comparison between these skin friction values is the similarity of shape, not necessarily of level. Separation downstream of Kendall's wave crests did not occur, while separation was intermittent on wave C. Therefore and exact correlation would not be expected.

The shear stress profile for wave C, shown in Fig. 18, illustrates well the rapid increase in surface shear created by air flow over the crests. Immediately after the crests, the shear stress decreases, indicating that the flow separates from the wave surface. The same qualitative observation was made from the smoke visualization pictures. The flow visualization, wall pressure distributions, and qualitative shear stress profiles are all consistent with the vortex flow pattern suggested in Fig. 14. These results do not identify a particular frequency of vortex shedding from the waves, but show that the vortex involves turbulent mixing with the outer flow.

4.5 Distinction Between Form Drag and Heated Film Values of C_f

Form drag measurements over one wavelength, discussed in Section 2.2, give the average shear stress acting on a horizontal surface a small distance above the wave crests. This shear stress is given by Eq. (2.23). The heated film measures the stress acting near the wave crest. Thus, C_f obtained from heated film measurements is only a part of the C_f value determined from form drag measurements. The following values illustrate the differences:

	Form Drag C_f Values	Heated Film C_f Values
Wave A	0.02	0.01
Wave C	0.01	0.005

If the effective shear stress obtained from the form drag measurements is considered, the wavy surface can be replaced by a very rough flat surface located at some position between the top and bottom of the wave. On the other hand, skin friction values obtained from the heated film apply only at the crest and do not represent the shear stress felt by the turbulent boundary layer as it passes over the waves.

Part II: Mean and Turbulent Velocity Profiles

4.6 Smooth Wall Velocity Profiles

A thick, turbulent boundary layer forms over the smooth false floor upstream of the waves when brushes are placed at the start of the floor. The smooth floor is 60 wavelengths long. The mean velocity profile measured by the two-wire method is shown in Fig. 19 and is closely approximated by

$$\bar{u}/u_* = 5.76 \log (yu_*/\nu) + 6.0 \quad , \tag{4.3}$$

where $u_*/U_\infty = 0.039$. Turbulent intensities $\sqrt{\overline{u'^2}}/U_\infty$ and $\sqrt{\overline{v'^2}}/U_\infty$ determined by the two-wire method are shown in Fig. 20 and are compared to Klebanoff's classic measurements (39). In general, the $\sqrt{\overline{u'^2}}/U_\infty$ results agree with the classic measurements for $y/\delta < 0.5$. For $y/\delta > 0.5$, the smooth floor profile has higher intensities. The C.S.U. tunnel with the wavy surface installed has a free-stream turbulent intensity of approximately 2%. The smooth floor profile of $\sqrt{\overline{v'^2}}/U_\infty$ is higher than Klebanoff's results. As will be discussed later, determination of v' by the two-wire method is less reliable than measurements of u' (see Section 4.82). However, the intensity profiles have the relative shape characteristic of smooth surface results. Probe calibration and data reduction procedures vary among researchers, and Antonia and Luxton (3) suggested comparing relative shapes of intensity profiles rather than absolute magnitudes.

Direct measurements of $\overline{u'v'}$ are given in Fig. 21. The two-wire measurements extrapolated to a wall skin friction of $C_f = 0.0032$, which compares favorably with 0.0031 obtained from the slope of the logarithmic velocity profile. Klebanoff's shear stress profile is also shown in Fig. 21 for comparison to the present measurements. The two-wire method of measuring stress appears to give reasonable values.

4.7 Wavy Surface Mean and Turbulent Velocity Profiles

Flow in the fully developed region far downstream from the first wave will be discussed in this section. Measurements of mean and turbulent velocities and their pertinent profile parameters are presented.

4.7.1 Mean Velocity Profiles and Related Results - Mean horizontal velocity profiles are shown in Figs. 22, 23, and 24 as a function of distance above the crest at various longitudinal wave positions. For a given wave size, the velocity profiles ($\bar{u}/U_\infty$ vs. y_T/δ) at the 15th, 20th, 24th, and 25th wave crests are essentially the same. For each velocity profile, the boundary layer parameters of total thickness δ, displacement thickness δ^*, momentum thickness θ, and shape factor H can be determined, where

$$\bar{u}\,(x,\delta) \simeq 0.99\, U_\infty \quad , \tag{4.4}$$

$$\delta^* = \int_0^\infty (1 - (\bar{u}/U_\infty))\, dy \quad , \tag{4.5}$$

$$\theta = \int_0^\infty (\bar{u}/U_\infty)[1 - (\bar{u}/U_\infty)]\, dy \quad , \tag{4.6}$$

and

$$H = \delta^*/\theta \quad . \tag{4.7}$$

The variation of these parameters is shown as a function of fetch in Figs. 25, 26, and 27. Between the first wave and approximately the tenth wave, the boundary layer grows rapidly, as shown by the changes in δ^* and θ . The additional momentum extracted by the first few waves causes the abrupt change in θ . Downstream of the fifteenth wave, the momentum thickness θ varies linearly with distance x. The momentum integral equation

$$C_f/2 = \frac{d\theta}{dx} \tag{4.8}$$

then gives constant C_f values (57).

Now that mean velocity profiles are available, various parameters can be compared to the similarity requirements discussed in Section 2.3. The comparison will show whether or not there is an equilibrium boundary layer above the wavy surface. First, the shape factor H is shown in Fig. 28 as a function of the skin friction coefficient C_f. Clauser's shape parameter G equals approximately 2.7 for the wavy surface flow. The local similarity concept requires that

$$H = (1 - (C_f/2)G)^{-1} \quad . \tag{4.9}$$

The measured H , C_f , and G follow Eq. (4.9) reasonably well. Also shown in Fig. 28 are the water wave results of Karaki and Hsu (36) and the square bar roughness results of Liu et al. (42). Form drag values of skin friction were used to determine G in this study. Since C_f is comparitively large, parameter G is smaller than previously reported values of 5 to 7 from other rough wall flows.

A correlation that relates many turbulent boundary layer flows was suggested by Liu et al. as

$$G = 1.47 \frac{\Delta}{\delta} + 0.74 \quad . \tag{4.10}$$

The measured values of G and $\frac{\Delta}{\delta}$ also fit this correlation even though the numerical values of G differ from those of other researchers. The data are shown in Fig. 29.

The parameter G is obtained from the velocity defect profile. Clauser (18) showed that turbulent velocity profiles with constant G are equilibrium profiles. Equilibrium is used to classify profiles which have a balance between a pressure force $\delta^+ \frac{dp}{dx}$ and the surface shear stress τ . For wave positions 15 through 25, $G = 2.7$. Thus, for these wave positions, the turbulent layer meets Clauser's equilibrium requirements.

The three requirements established by Rotta (Section 2.3) are also met. In each case, Rotta's conditions of $dp/dx = \text{constant}$, $\delta^* \propto (x - x_o)$, and $C_f = \text{constant}$ are met. (See Figs. 25, 26, 27, 30 and Eq. (4.8)). The turbulent boundary layer has now been shown to be an equilibrium boundary layer. One of the possible equilibrium turbulent boundary layers given by Rotta has

$$\frac{dp}{dx} \propto \exp\left[\mu'(x - x_o)\right] \quad , \tag{4.11}$$

with $\mu' > 0$, and constant wave height (or constant amplitude). Although the pressure appears to be a linear function of x for this flow, the wavy surface turbulent boundary layer still meets the requirements of an equilibrium layer. Such a turbulent boundary layer has not been reported previously.

4.7.2 Power Law Velocity Profiles - The mean velocities above the wavy surface might be related to a power of the vertical coordinate y as

$$\bar{u}/U_\infty = (y/\delta)^{1/n} \quad , \tag{4.12}$$

where n can be as small as 3 according to Liu et al. Karaki and Hsu (36) also showed that rough surface boundary layer velocity profiles for $y/\delta > 0.3$ could be represented by power law profiles. However, the mean velocity profiles shown in Figs. 31 and 32 for the waves A and C cannot be represented by power law profiles.

Antonia and Luxton (2,3,4) showed that for the first few roughness elements, mean velocities are proportional to the square root of y:

$$\bar{u} \propto y^{\frac{1}{2}} \quad . \tag{4.13}$$

However, the transitional flow over the first few waves is not the primary concern here, and the power law velocity profiles are discussed only in their relation to the fully developed flow region.

4.7.3 Logarithmic Velocity Profiles - The mean velocity above the wavy surface can be represented by the logarithmic velocity profile

$$\bar{u}/U_\infty = \sqrt{C_f/2}\left[\frac{1}{\kappa} \ln \frac{(y_\tau + \varepsilon h)u_*}{\nu} + A - \frac{\Delta u}{u_*}\right] \quad , \tag{4.14}$$

which is assumed to hold for $y_\tau + \varepsilon h < 0.2$, where εh is a yet undetermined origin shift downward from the wave crests. As discussed in Section 2.2, the origin shift εh and skin friction coefficient C_f are inter-related. Using the form drag measurements of C_f, the origin shift εh can be determined by adding small values to y and comparing the slope of the velocity points for $y_T + \varepsilon h/\delta < 0.2$ to the required slope of $(1/\kappa)\sqrt{C_f/2}$. For the mean velocity profiles at the 25th crest, the resulting origin shifts are 0.5 h for wave A, 0.75 h for wave B, and 1.0 h for wave C. These origin shifts could vary ± 0.05 h with negligible changes in the resulting slopes. The values of ε mean that the origin of y is shifted below the crest a fractional amount of the wave height. Equivalently, a very rough surface could be placed 0.25 h above the trough of wave B without changing the mean logarithmic velocity profile. The logarithmic velocity profiles are shown in Figs. 33, 34, and 35.

In general, as roughness elements become more closely packed, the origin moves toward the top of the elements. This particular case was discussed in Section 2.2. For very widely spaced roughness elements the origin moves to the base of the elements. The origin shifts for the three wave sizes appear to be physically reasonable. A decrease in wave amplitude has the equivalent effect as an increase in roughness-element spacing, since the origin moves downward.

The origin shift was determined from the form drag measurements on the 25th wave. Since C_f was shown to be constant for the 15th through 25th waves, the origin for these positions is constant. Therefore, the appropriate value of ε can then be used in the logarithmic velocity profile for the 15th through 25th wave crests for each wave size. Upstream of the 15th wave, the origin shift was assumed to be the same as the origin shift downstream of this position. Using this assumption gives the qualitative distributions of C_f shown in Fig. 36 although the logarithmic velocity profile probably does not hold in the transitional region since the boundary layer is undergoing rapid growth. The rapid decreases in skin friction after the first few roughness elements were reported by others (4,8,24,53, 68). Flow upstream of the 15th crest is not of primary concern in this thesis and is presented here only to obtain an overall picture.

The roughness function can be determined from the logarithmic velocity profile in the fully developed region. The resulting roughness function is shown in Fig. 37 as a function of the roughness number hu_*/ν . Also plotted are the roughness functions from several other studies. For the wavy surface

$$\Delta u/u_* = 5.76 \log (hu_*/\nu) + C_2 \quad , \tag{4.15}$$

where C_2 is approximately -1.1. Values of C_2 for "k" type rough surfaces have been reported between -0.2 and -5.5 (17,31,52). To illustrate that the wavy surface is indeed a "k" type rough surface, the roughness function can be plotted as a function of the origin shift $\varepsilon hu_*/\nu$ as shown in Fig. 38. The slope of the roughness function is $1/\kappa$. However, the slope of the data in Fig. 38 is greater than $1/\kappa$, indicating that the surface can not be characterized by the origin shift (53).

The velocity defect profiles are shown in Fig. 39 for the 25th crest of each wave size. Clauser's form (18) for the velocity defect profile is

$$(U_\infty - \bar{u})/u_* = -[5.76 \log (yu_*/\delta^* U) + C_3] \tag{4.16}$$

where C_3 was shown to be a function of C_f (57). For the wavy surface,

C_3 is approximately 1.5. Roughness effects on C_3 appear to be ill-defined. Furuya and Fujita (30) determined $C_3 = 0.3$ for flow over sand grain and wire screen roughnesses -- a decrease from the smooth wall value of 0.6. Tillman (see (57)) and Perry et al. (53) showed that C_3 increased with C_f. Thus, the present result is in agreement with Perry et al. and Tillman's but opposite that of Furuya and Fujita.

Large values of C_f shift the velocity defect profile downward and to the right (Fig. 39), similar to the shift shown in Fig. 1. Hama (31) suggested that the logarithmic velocity profile extends outward to $yu_*/\delta^* U_\infty = 0.045$ (or $y/\delta \simeq 0.15$). The velocity profile shown in Fig. 39 indicates that the logarithmic portion may extend to $yu_*/\delta^* U_\infty = 0.2$ where $y = y_T + \varepsilon h$. The outer edge of the logarithmic velocity profile region extends to $y_T/\delta \simeq 0.2$ when the C_f and δ^* values for each wave are used. Perry et al. also indicated that the outer edge of the logarithmic region may extend to $yu_*/\delta^* U_\infty = 0.07$, which is also larger than the value suggested by Hama. The implication is that increasing surface friction increases $yu_*/\delta^* U_\infty$, but has little effect on the extent of the logarithmic portion, which is still in the lower 20% of the boundary layer.

4.8 Turbulence Measurements

4.8.1 Two-Wire Method - Turbulence measurements were made by a two-wire method. This method, which is discussed in Section 3.6 and Appendix A, is a relatively "new" method of measuring turbulent flows. Karaki and Hsu (36) presented data collected by the two-wire method, and the apparent advantages resulted in the choice of the two-wire method for data collection for this thesis.

The advantages of this two-wire method are: 1. the velocity vector can be measured as a function of time, and 2. measurements of turbulence intensities do not rely on linear response assumptions for the hot-wires. The main disadvantage is that physical quantities can not be obtained immediately. First, anemometer signals must be recorded on analog tapes; the analog tapes must be digitized; and finally, the data must be processed back to physical quantities by a digital computer. Unless an on-line computing facility is available, an unavoidable delay occurs between the time when data is taken and the time when data is reduced. Therefore it is difficult to re-run "questionable" data. In addition, if a great deal of data is desired, digitizing and computing cost may outweigh the advantages.

4.8.2 Turbulence Intensities and Vertical Velocities - Turbulence intensities $\sqrt{\overline{u'^2}}/U_\infty$ and $\sqrt{\overline{v'^2}}/U_\infty$ are shown as a function of y/δ in Figs. 40, 41, and 42. The length of the digitized record is generally 6.5 sec for each data point. Longer data records of 19.5 sec were used to obtain intensities for selected positions above the waves (see Fig. 40). These longer records appear to "smooth" the data, but insufficient records were taken to reach any firm conclusions. Digitizing and computing costs limited most records to 6.5 sec. Eight to nine minutes of central processing time on a C.D.C. 6400 digital computer were needed for data reduction of 30 profile points, each with 6.5 sec records.

For wave C, the measured intensities are compared to the far-downstream data of Liu et al. (42), Corrsin and Kistler (21), and Antonia and Luxton (3,4). In general, the measured intensities agree reasonably well with these rough surface studies where C_f varied between 0.005 and 0.010. However, intensity measurements above rough surfaces are functions of probe configuration and calibration procedures, and profiles should be compared on relative shape, as discussed in Section 4.6.

The intensity profiles shown in Figs. 40, 41, and 42 are for the 25th crest of each wave size. The profiles for the 20th and 24th crests have essentially the same magnitude and shape. The gradient in the x-direction was difficult to determine because of data scatter, but appeared to be negligible. The significance of a negligible streamwise gradient is that it indicates a self-preserving flow pattern over the last few waves. If the mean and turbulent velocity profiles are essentially constant with downstream distance, the flow is in a self-preserving state (32,57).

A fluctuation v' is the departure of the vertical velocity from the mean vertical velocity, $\overline{v}$, at a particular instant in time. A mean vertical velocity was determined at each elevation above the wavy surface for each 6.5 sec data sample. In general, the vertical velocities are less than 1 fps for all heights above the waves. Typical vertical velocity profiles are shown in Fig. 43. Vertical velocity can also be obtained from the mean horizontal velocity profiles (Figs. 22, 23, and 24) and the two-dimensional continuity equation

$$\overline{v} = -\frac{d}{dx}\int \overline{u}\, dy \quad . \qquad (4.17)$$

Values of vertical velocity, $\overline{v}$, from the integrated continuity equation were less than 0.5 fps for all heights above the crest. These values of velocity are 50% lower than the values from the hot-wire method. However, measurements of $\overline{v}$ by either the two-wire method or the continuity equation can easily differ by $\pm$ 50%. The integrated continuity equation requires differentiating integrals of nearly the same magnitude -- an error-prone procedure. The two-wire method for measuring $\overline{v}$ is extremely sensitive to the calibration parameters and wire angles. The magnitude of the vertical velocity component is very small compared to the local mean horizontal velocity, so the angle between the mean velocity vector $\overline{u}\,\hat{i} + \overline{v}\,\hat{j}$ and the horizontal velocity $\overline{u}$ is small. Errors in the determination of the wire angles make the determination of this small angle (or equivalently, $\overline{v}$) uncertain. Thus, the vertical velocity profile should be considered on shape only.

At the wave surface, the vertical velocity is zero. A tentative explanation for the vertical velocity profiles in Fig. 43 can be given. Referring to Fig. 14, the streamlines may curve upward as the flow moves from area "a" toward the crest. Compared to $\overline{u}$, the vertical velocity component $\overline{v}$ is small and decays rapidly with distance above the crest. A small vertical velocity component near the wave crest enhances the separation of flow from the wave, and area "s" is near the crest. Separation very near the crest was observed in the flow visualization and is illustrated in Fig. 12.

There is considerable data scatter in the vertical velocity profiles and the turbulence intensity profiles, but an explanation can be given. First, turbulent flow above the wavy surface is a random process, and the length of data needed to obtain stable averages and moments by the two-wire method may be greater than the 6.5 sec used for the profiles. Although the longer data records of 19.5 sec appear to smooth turbulence intensity profiles, they still do not produce stable mean vertical velocity profiles above the wave crests. Again, errors in the calibration constants of the hot-wires, the angles of the wires, and the calibration of the amplifiers and the tape recorder all contribute to data scatter. The uncertainty in the intensity measurements is subsequently of the order of $\pm$ 20%, but even with this uncertainty, the profile shapes in Figs. 40, 41, and 42 appear to be reasonable.

4.8.3 Shear Stress Measurements - Shear stress magnitudes above the wavy surface were measured by two methods. First, the "effective wall shear stress" was obtained from measurements of wave form drag. Second, direct measurements of the turbulent shear stress, $-\rho\overline{u'v'}$, were made above the wave crests by the two-wire method. The assumptions necessary to relate the measured form drag to the "effective wall shear stress" were discussed in Section 2.2. In addition, the wave-induced Reynolds shear stress, $-\rho\tilde{u}\tilde{v}$, is assumed to decay rapidly above the wavy surface. Then, the "effective shear stress" from the momentum balance over the control volume ABCD (Fig. 3) is the average turbulent shear stress over one wavelength. Since the effective shear stress τ_e is a total shear stress measured on surface BC, τ_e is used in the logarithmic velocity profile to determine the shift in origin.

Turbulent shear stresses above the wave crests are shown in Figs. 44, 45, and 46. The profiles shown are the arithmetic averages of the profiles for the 24th and 25th crests of each wave size. The average profile is smoother than either individual profile. Shear stresses were determined by the two-wire method using the relation

$$\overline{u'v'} = \overline{uv} - \overline{u}\,\overline{v} \quad , \qquad (4.18)$$

where u and v are instantaneous values of the horizontal and vertical velocities and the overbar represents time averaging. In general, $\overline{v}$ is less than 5% of $\overline{u}$. Also, the small magnitude of $\overline{v}$ ($\overline{u} >> \overline{v}$) made it difficult to measure. Incorrect values of $\overline{v}$ produce uncertainty in the values of $\overline{u'v'}$ near the wave surface. Thus, the uncertainty of $\overline{u'v'}$ at 19:1 odds is estimated at $\pm$ 30%. Direct measurements of turbulent shear stresses above other rough surfaces were presented by Logan and Jones (43), and Antonia and Luxton (3,4). These measurements used the linear approximation for the hot-wire response as opposed to the two-wire digital method of this study.

As shown in Figs. 44, 45, and 46, values of $\overline{u'v'}$ near the crest extrapolate to a C_f less than the "effective shear stress" values. The measurements of Antonia and Luxton also extrapolate to a wall C_f below the value obtained from their form drag measurements. Antonia and Luxton's measurements are included in Fig. 46. For $y/\delta < 0.2$, their measurements decrease rapidly, while the turbulent shear stresses for wave C increase.

The disagreement between the friction coefficients from the hot-wire and form drag methods can be attributed to the meaning of the "effective shear stress" τ_e . This stress is

$$\tau_e = \langle -\rho\ \tilde{u}\tilde{v} \rangle + \langle -\rho\ \overline{u'v'} \rangle \quad , \tag{4.19}$$

where the brackets < > represent an average over one wavelength. Turbulent shear stresses $-\rho\ \overline{u'v'}$ above the crests are a part of $\langle -\rho\ \overline{u'v'} \rangle$ and do not include the wave-induced stresses $-\rho\tilde{u}\tilde{v}$. Thus, $-\rho\ \overline{u'v'}$ measures only part of the total shear stress at any height above the wavy surface. The wave-induced shear stress could provide the missing momentum transfer to the surface, but this is only conjecture without measurements of $-\rho\ \tilde{u}\tilde{v}$. Thus, the apparent lack of agreement is between two shear stresses which should not be expected to agree anyway. The hot film at the wave crests measures a value of shear stress τ which is approximately the same magnitude as the turbulent shear stress $-\rho\ \overline{u'v'}$ for waves A and C, but neither method gives the same shear stress as the form drag method.

Another method for determining the shear stress profiles is the momentum integral equation, which was used by Liu et al. (42), Doenecke (24), and Betterman (8). The momentum integral equation can be written as

$$\frac{\tau}{\rho} = \frac{d}{dx}\int_y^\infty u(U_\infty - u)\ dy + \frac{dU_\infty}{dx}\int_y^\infty (U_\infty - u)\ dy$$
$$-(U_\infty - u)v - \frac{d}{dx}\int_y^\infty (\ \overline{u'^2} - \overline{v'^2}\ )\ dy \quad , \tag{4.20}$$

where the "inner" surface of the control volume is at a distance y above the rough surface. Velocities u and v represent the mean and wave-induced velocities, where

$$u = \overline{u} + \tilde{u} \quad , \tag{4.21}$$

and $$v = \bar{v} + \tilde{v} \quad . \tag{4.22}$$

Thus, the shear stress τ contains the wave-induced stresses. However, evaluating shear stresses by a momentum integral technique requires great care. For the wavy surface, the term $-(U_\infty - u)v$ in Eq. (4.20) was found to vary to such a degree that values of τ were very uncertain. The primary reason for this uncertainty was the unreliable measurements of vertical velocity v, since it was obtained from the two-dimensional continuity equation

$$\bar{v} = - \int \frac{\partial \bar{u}}{\partial x} dy \quad . \tag{4.23}$$

Substitution of the horizontal mean velocity profiles measured at the wave crests into Eq. (4.23) results in the average vertical velocities over the distance Δx in the derivative $\partial u/\partial x$. Generally, Δx is 1, 2, or 5 wavelengths; so v represents the average vertical velocity between two wave crests either 1, 2, or 5 wavelengths apart.

4.9 Eddy Viscosity

The eddy viscosity K_m, defined by

$$K_m = \frac{\tau/\rho}{\partial \bar{u}/\partial y} \quad , \tag{4.24}$$

is plotted as a function of the distance above the trough in Fig. 47. The smoothed shear stresses from Figs. 44 and 46 were used with the mean velocity profiles in Figs. 22 and 24 for measuring K_m. For wave A or C,

$$K_m \simeq \kappa u_* \, (y_\tau + \varepsilon h) \qquad (4.25)$$

if ε equals 0.5 or 1.0 for wave A or C respectively, and $y/\delta < 0.1$. A linear variation of K_m with distance $y_\tau + \varepsilon h$ less than 10% of the total boundary layer thickness provides indirect proof that the law of the wall can be used. Linear variations of K_m were also reported by Liu et al. and Antonia and Luxton. For their measurements, $K_m \simeq \kappa u_* y$ only for $y_\tau < 0.1\,\delta$. The mean velocity profiles shown in Figs. 33, 34, and 35 indicate that the logarithmic portion extends to $y_\tau/\delta \simeq 0.2$. Thus, the logarithmic velocity profile represents only the lower 10% of the total boundary layer if a linear variation of K_m is used to verify the existence of the wall law.

4.10 Windbreak Effects

The wavy surface flow of this study is a model of atmospheric wind over an open, corrugated field. The model wavy surface acts as a surface windbreak by creating vortices between the waves and reducing the wing velocity above the waves. The vortex was shown to reduce the moisture loss in the trough (65). These two features of the wavy surface flow strongly suggest that field micro-ridges created by a roller (35) would provide a beneficial surface for promoting crop growth in the troughs.

The reduction in overall wind speed is at the expense of increased surface friction. The usual way of documenting wind reduction caused by a windbreak is by a wind-reduction factor R_f defined by (25,41)

$$R_f = 100[1 - (\bar{u}/\bar{u}_o)] \quad , \qquad (4.26)$$

where $\bar{u}_o$ is wind speed above an open, smooth surface and $\bar{u}$ is wind speed over a surface windbreak. The factor R_f is shown in Figs. 48, 49, and 50 as a function of height above the wave crests for each wave size. Velocity $\bar{u}_o$ is the smooth wall velocity profile. These plots show that the greatest percentage reduction in wind speed at a given height is achieved by the largest wave (or field corrugation). However, the factor R_f does not reflect the increased shear stress needed to reduce the wind speed, and the modified factor

$$R_f' = u_*/u_{*o}[1 - (\bar{u}/\bar{u}_o)]100 \qquad (4.27)$$

is suggested as a more appropriate measure of this reduction for surface windbreaks. The additional factor u_*/u_{*o} is a measure of the increase in surface shear velocity u_* relative to the smooth surface value u_{*o} . The modified factor R_f' is shown in Fig. 51 for the far-downstream waves of each size.

The reason for including u_* as a parameter in R_f' is the following. The transport of sand by wind is proportional to u_*^3 and inversely proportional to the 3/2-power of mean soil-grain size D (34). If q represents the rate of sand transport in lb/hr, then

$$q \propto u_*^3/D^{\frac{3}{2}} \quad . \qquad (4.28)$$

Thus, for a given mean field soil-grain size, small reductions in surface shear result in substantial reductions in loose-sand transport by the wind. As far as blowing soil is concerned, the factor u_* can not be disregarded.

Surface soil will start to move where the friction is largest. The surface measurements of friction shown in Figs. 17 and 18 indicate that the friction is the greatest near the wave crests (as would be expected). The viscous friction

$$\tau = \mu \frac{\partial \bar{u}}{\partial y'} \quad , \tag{4.29}$$

where y' is distance perpendicular to the wave surface and $\bar{u}$ is velocity along the surface, probably starts the soil moving initially. The friction velocity u_* is a measure of this stress, and reductions in u_* are accompanied by reductions in the viscous stress τ . As the wave heights are decreased, both the effective shear stress and the surface shear stress are decreased (as shown in Section 4.5).

Extrapolating the results of this study to field corrugations shows that the waves will erode at the crests first. However, as the waves become shallower, less windbreak protection is afforded to seeds planted in the troughs; but there will also be a decreased erosion rate. Thus, there is a trade-off between the amount of protection created by a given wave size and the rate at which the wave changes shape. The results of this study indicate that the largest amplitude wave provides the most protection, but also tends to erode the quickest. Further experimentation with erodable surfaces in a large wind-tunnel are needed to support the results of the experiments with solid waves.

Chapter V

SUMMARY AND CONCLUSIONS

Turbulent boundary layer flow over three sizes of sinusoidal waves was investigated experimentally in this thesis. Primary emphasis was on the fully-developed flow over the last few waves. Mean and turbulent velocity profiles were measured with a hot-wire/digital-data technique. Surface shear stress near the wave crests was measured by a heated-film method, and wave form drag was measured to determine the shift-in-origin in the logarithmic velocity profile.

The results presented and discussed support the following conclusions:

1. The flow over the last few waves is an equilibrium turbulent boundary layer which conforms to Clauser's and Rotta's requirements for self-preservation.

2. The shift-in-origin parameter ε in the logarithmic velocity profile,

$$\bar{u}/u_* = (1/\kappa)\ \ln[(y_T + \varepsilon h)u_*/\nu] + A - \Delta u/u_* \quad , \tag{5.1}$$

is a function of the wave-height h. For shallow waves $(a/\lambda \simeq 0.06)$, the origin for distances perpendicular to the mean surface is at the wave trough. Steep waves $(a/\lambda \simeq 0.2)$ have the origin midway between the crest and trough.

3. The roughness function $\Delta u/u_*$ for wavy surfaces is related to the wave-height by

$$\Delta u/u_* = (1/\kappa)\ \ln(hu_*/\nu) - 1.1 \qquad (5.2)$$

and is not a function of the origin-shift εh .

4. Measurements of shear stress at the wave crest by the two-wire method and surface-mounted heated-film are in close agreement (differ by less than 15%), but neither measurement agrees with the effective shear stress deduced from the form drag measurements over one wavelength. Form drag measurements are influenced by the total flow field around each wave, as manifested by the surface pressures. Part of this flow field may contain wave-induced velocities, and the measurements presented in this thesis strongly suggest that the wave-induced shear stresses supply the additional momentum loss to the surface.

5. Eddy viscosity,

$$K_m = (\tau/\rho)/(\partial\bar{u}/\partial y) \qquad (5.3)$$

is a linear function of the distance y above the wave troughs. For wave C,

$$K_m \simeq 0.4u_*y \quad , \qquad (5.4)$$

where u_* is the effective friction velocity and y is less than $0.15\ \delta$. Since $K_m \simeq 0.4u_*y$, the mean velocity can be represented by the logarithmic velocity profile in the lower 10 to 15% of the total boundary layer. The Clauser form of the velocity defect profile

$$\frac{U_\infty - \bar{u}}{u_*} = -\left(\frac{1}{\kappa}\ \ln \frac{yu_*}{\delta^* U_\infty} + C_3\right) \qquad (5.5)$$

with $C_3 \simeq 1.5$ for the wavy surface also supports the logarithmic variation in the lower 20% of the boundary layer. The constant C_3 is larger for rough surface flows than for smooth surface flows.

6. The two-wire method of measuring mean and turbulent velocities, though providing encouraging measurements in this study, must be examined further to clarify more fully the importance of calibration techniques and wire orientation. The results presented here show that this particular method may be quite useful for an on-line computing facility.

7. The largest wave provides the most reduction in wind speed above the surface and is thus the best extended-surface windbreak by that criterion. Simple wind-speed reduction is not the only requisite of a surface windbreak. Surface shear stresses, which "scuff" surface soil particles along, must also be considered, and the modified wind reduction factor

$$R_f' = 100\, u_*/u_{*_o}[1 - \bar{u}/\bar{u}_o] \tag{5.6}$$

should be used for surface windbreaks to account for both wind speed reduction $(1 - \bar{u}/\bar{u}_o)$ and increased surface shear stress (u_*/u_{*_o}) .

REFERENCES

REFERENCES

1. Achenbach, E. (1968), "Distribution of local pressure and skin-friction around a circular cylinder in cross-flow up to Re = 5×10^5, Journal of Fluid Mechanics, Vol. 34, p. 625.

2. Antonia, R.A. and R.E. Luxton (1969), "The energy balance in a turbulent boundary layer on a rough wall", Kolling Research Lab., Technical Note F-4, Dept. of Mech. Engrg., Univ. of Sydney, Australia.

3. Antonia, R.A. and R.E. Luxton (1969), "The response of a turbulent boundary layer to a step change in surface roughness", Kolling Research Lab. T.N. F-7, Dept. of Mech. Engrg., Univ. of Sydney, Australia.

4. Antonia, R.A. and R.E. Luxton (1971), "The response of a turbulent boundary layer to an upstanding step change in surface roughness", Transactions A.S.M.E., Journal of Basic Engineering, Vol. 94, p. 22.

5. Bates, C.G. (1945), "Shelterbelt influence, Part I, General description of studies made", Journal of Forestry, Vol. 43, p. 88, and "Part II, The value of shelterbelts in house-heating", p. 176.

6. Bellhouse, B.J. and D.L. Schultz (1966), "Determination of mean and dynamic skin friction, separation and transition in low-speed flow with a thin-film heated element", Journal of Fluid Mechanics, Vol. 24, p. 379.

7. Bellhouse, B.J. and D.L. Schultz (1968), "The measurement of fluctuating skin friction in air with heated thin-film gauges", Journal of Fluid Mechanics, Vol. 32, p. 675.

8. Betterman, D. (1966), "Contribution a l'etude de la convection forcee turbulente le long de plaques rugueuses", International Journal of Heat and Mass Transfer, Vol. 9, p. 153.

9. Blackman, R.B. and J.W. Tukey (1958), The Measurement of Power Spectra, Dover, New York.

10. Bonchkovskaya, T.V., (1955), "Wind flow over solid wave models", Akademia Nauk SSSR, Morskoi Gidrofizicheskii Institut, Vol. 6, p. 98.

11. Brown, G.L. (1967), "The application of heated surface films to aerodynamic measurements in boundary layers", Ph.D. Thesis, Madgalen College, Univ. of Oxford.

12. Brown, K.W. and W. Covey (1966), "Energy-budget evaluation of the micro-meteorological transfer processes within a cornfield", Agricultural Meteorology, Vol. 3, p. 73.

13. Champagne, F.H., C.A. Sleicher and O.H. Wehrmann (1967), "Turbulence measurements with inclined hot-wires, Part 1, Heat transfer experiments with inclined hot-wires", Journal of Fluid Mechanics, Vol. 28, p. 153.

14. Champagne, F.H. and C.A. Sleicher (1967), "Turbulence measurements with inclined hot-wires, Part 2, Hot-wire response equations", Journal of Fluid Mechanics, Vol. 28, p. 177.

15. Chepil, W.S. (1965), "Transport of soil and snow by wind", Agricultural Meteorology, Meteorological Monograph, Vol. 6, #28.

16. Cheyney, E.G. (1931), "Establishment, growth, and influence of shelterbelts in the prairie region of Minnesota", Univ. of Minn. Agricultural Experimental Station Bulletin #285.

17. Clauser, F.H. (1954), "Turbulent boundary layers in adverse pressure gradients", Journal of Aeronautical Sciences, Vol. 21, p. 91.

18. Clauser, F.H. (1956), "The turbulent boundary layer", Advances in Applied Mechanics, Vol. 4, p. 1 (H. Dryden and T. Von Karman, eds.), Academic Press, New York.

19. Coles, D. (1956), "The law of the wake in the turbulent boundary layer", Journal of Fluid Mechanics, Vol. 1, p. 191.

20. Coles, D. (1955), "The law of the wall in turbulent shear flow" 50 Jahre Grenzschichtforschung, (H. Gorther and W. Tollmien, eds.), p. 153.

21. Corrsin S. and A.L. Kistler (1954), "The free stream boundaries of turbulent flow", N.A.C.A. Technical Note 3133.

22. Denuyl, D. (1936), "The zone of effective windbreak influence", Journal of Forestry, Vol. 34, p. 689.

23. van Driest, E.R. (1956), "On turbulent flow near a wall", Journal of Aeronautical Sciences, Vol. 23, p. 1009.

24. Doenecke, J. (1964), "Contribution a l'etude de la convection forcee turbulent le long de plaques rugueuses", International Journal of Heat and Mass Transfer, Vol. 7, p. 133.

25. van Eimern, J. (1964), Windbreaks and Shelterbelts, Technical Note #59, World Meteorological Organization, Geneva.

26. Enochson, L.D. and R.K. Otnes (1968), Programming and Analysis for Digital Time Series Data, Shock and Vibration Monograph #3, Naval Research Laboratory.

27. Fage, A. and V.M. Falkner (1931), "Further experiments on the flow around a circular cylinder", A.R.C. R & M 1369.

28. Frenkiel, F.N. and P.S. Klebanoff (1967), "Correlation measurements in a turbulent flow using high-speed computing methods", Physics of Fluids, Vol. 10, p. 1737.

29. Freymuth, P. (1969), "Nonlinear control theory for constant-temperature hot-wire anemometers", Review of Scientific Instruments, Vol. 40, p. 258.

30. Furuya, Y. and H. Fujita (1967), "Effect of surface roughness on the velocity defect law", Physics of Fluids, Vol. 10, p. 155.

31. Hama, F.R. (1954), "Boundary layer characteristics for smooth and rough surfaces", Transactions of the Society of Naval Architects and Marine Engineers, Vol. 62, p. 333.

32. Hinze, J. (1959), Turbulence, McGraw-Hill, New York.

33. Hsi, G. and J.H. Nath (1968), "Wind drag within a simulated forest canopy field", Colorado State Univ. Report CER68-69 GH-JHN6.

34. Hsu, S.A. (1971), "Wind stress criteria in eolian sand transport", Journal of Geophysical Research, Vol. 76, p. 8684.

35. Hyder, D.N. and R.E. Bement (1969),"A micro-ridge roller for seedbed modification", Journal of Range Management, Vol. 22, p. 54.

36. Karaki, S. and E.Y. Hsu (1968), "An experimental investigation of the structure of a turbulent wind over water waves", Civil Engrg. Dept., Stanford Univ., Technical Report 88.

37. Kendall, J.M. (1970), "The turbulent layer over a wall with progressive surface waves", Journal of Fluid Mechanics, Vol. 41, p. 259.

38. Kistler, A. L. and F.C. Tan (1967), "Some properties of turbulent separated flows", Physics of Fluids, Vol. 10, p. 165.

39. Klebanoff, P.S. (1955), "Characteristics of turbulence in a boundary layer with zero pressure gradient", N.A.C.A. Report 247.

40. Kolar, V. (1965), "Heat transfer in turbulent flow of fluids through smooth and rough pipes", International Journal of Heat and Mass Transfer, Vol. 8, p. 639.

41. Kung, R.J. (1970), "Boundary layer development over equally spaced fences", Ph.D. Dissertation, Colorado State Univ., Fort Collins.

42. Liu, C.K., S.J. Kline and J.P. Johnston (1966), "An experimental study of turbulent boundary layers on rough walls", Mech. Engrg. Dept., Stanford Univ. Report MD-15.

43. Logan, E. and J.B. Jones (1963), "Flow in a pipe following an abrupt increase in surface roughness", Transactions A.S.M.E., Journal of Basic Engineering, Vol. 85, p. 35.

44. Lumley, J.L. and H.A. Panofsky (1964), The Structure of Atmospheric Turbulence, Interscience, New York.

45. Malina, F.J. (1941), "Recent developments in the dynamics of wind-erosion", American Geophysical Union Transactions, Part II, p. 262.

46. Malkus, W.V.R. (1961), "Similarity arguments for fully developed turbulence", Nuovo Climeto, Vol. 22, p. 376.

47. Marlatt, W.E. and D.N. Hyder (1970), "Soil ridging for reduction of wind erosion from grass seedbeds", Journal of Range Management, Vol. 23, p. 170.

48. Morris, H.M. (1955), "Flow in rough conduits", Transactions A.S.C.E. Vol. 120, p. 373.

49. Motzfeld, H. (1937), "Die turbulente Stromung an welligen Wanden", Z.A.M.M., Vol. 17, p. 193.

50. Nikuradse, J. (1933), "Stromungsgesetze in rauhen Rohen", V.D.I. Forshungsheft, #361.

51. Nunner, W. (1956), "Warmeubergang und Druckabfall in rauhen Rohren", V.D.I. Forschungsheft 455, Series B, Vol. 22, p. 5.

52. Perry, A.E. and P.H. Joubert (1963), "Rough wall boundary layers in adverse pressure gradients", Journal of Fluid Mechanics, Vol. 17, p. 193.

53. Perry, A.E., W.H. Schofield, and P.N. Joubert (1969), "Rough wall turbulent boundary layers", Journal of Fluid Mechanics, Vol. 37, p. 383.

54. Phillips, O.M. (1966), The Dynamics of the Upper Ocean, Cambridge University Press, London.

55. Plate, E.J. (1971), Aerodynamic Characteristics of Atmospheric Boundary Layers, U.S. A.E.C. TID-25465.

56. Reichardt, H. (1951), "Vollstandige Darstellung der turbulent Geshwindikeitsverteilung in glatten Leitungen", Z.A.M.M., Vol. 31, p. 208.

57. Rotta, J.C. (1962), "Turbulent boundary layers in incompressible flow", Progress in Aeronautical Sciences, Vol. 2, (A. Ferri, D. Kuchemann, and L.H.G. Sterne, eds.), Pergamon, New York.

58. Schlichting, H. (1960), Boundary Layer Theory, McGraw-Hill, New York.

59. Schraub, F.A. and S.J. Kline (1965), "A study of the structure of the turbulent boundary layer with and without longitudinal pressure gradients", Mech. Engrg. Dept., Stanford Univ. Report MD-12.

60. Son, J.S. and T.J. Hanratty (1969), "Velocity gradients at the wall for flow around a cylinder at Reynolds numbers from 5×10^3 to 10^5", Journal of Fluid Mechanics, Vol. 35, p. 353.

61. Stanton, T., D. Marshall, and R.Houghton (1932), "The growth of waves on water due to the action of the wind", Proceedings of the Royal Society of London, Series A, Vol. 137, p. 283.

62. Stearns, C.R. (1970), "Determining surface roughness and displacement height", Boundary Layer Meteorology, Vol. 1, p. 102.

63. Stegen, G.R. and C.W. van Atta (1970), "A technique for phase speed measurements in turbulent flow", Journal of Fluid Mechanics, Vol. 42, p. 689.

64. Townsend, A.A. (1956), The Structure of Turbulent Shear Flow, Cambridge Univ. Press, Cambridge.

65. Verma, S. (1971), "Mass transfer from rough surfaces", Ph.D. Thesis, Colorado State Univ.

66. Webb, R.L., E.R.G. Eckert, and R.J. Goldstein (1971), "Heat transfer and friction in tubes with repeated-rib roughness", International Journal of Heat and Mass Transfer, Vol. 14, p. 601.

67. Woodruff, N.P. and A.W. Zingg (1952), "Wind-tunnel studies of fundamental problems related to windbreaks", U.S. Dept. of Agriculture, Soil Conservation Service SCS-TP-112.

68. Yeh, F.F, and E.C. Nickerson (1970), "Air flow over roughness discontinuity", Colorado State Univ. Report CER70-71FFY-ECN6.

APPENDIX

APPENDIX A

DETERMINING VELOCITY FROM A TWO-WIRE ARRANGEMENT USING DIGITAL DATA

The basic assumption for this method is that the instantaneous response of the wires is given by

$$\frac{I^2R}{\Delta T} - A = B(\sin^2\beta + k^2\cos^2\beta)^{1/2n}\, U^{1/n} \quad , \tag{A.1}$$

where I^2 is the current through a wire of resistance R , ΔT is the resulting overheat, and β is the angle between the total velocity U and the wire (see Fig. 9). Coefficients A and B are determined by a calibration for each wire, and the exponent $1/n$ is approximately 0.5. A separate calibration determined k as approximately 0.33. Instantaneous values of $I^2R/\Delta T$ are obtained for each wire from the digitized data. Then, for a particular instant in time, knowing $I^2R/\Delta T$, A, and B for each wire gives

$$U_{eff}^{1/n} = U^{1/n}\,(\sin^2\beta + k^2\cos^2\beta)^{1/2n} \quad , \tag{A.2}$$

where U_{eff} is called the "effective cooling velocity". Then

$$U_{eff}^2 = U^2\,(\sin^2\beta + k^2\cos^2\beta) \tag{A.3}$$

for each wire. Let

$$y = (U_{eff}^2)_1/(U_{eff}^2)_2 \quad . \tag{A.4}$$

Then

$$y = [1 + (k^2 - 1)\cos^2\beta_1]/[1 + (k^2 - 1)\cos^2\beta_2] \tag{A.5}$$

The last equation can be re-written as

$$[\tfrac{1}{2}y(k^2 - 1) - \tfrac{1}{2}(k^2 - 1)\cos 2\Sigma]\cos 2\beta_2 + [\tfrac{1}{2}(k^2 - 1)\sin 2\Sigma)\sin 2\beta_2 = (1 - y)(1 + \tfrac{1}{2}(k^2 - 1)) \quad , \tag{A.6}$$

where the total included angle Σ is given by

$$\Sigma = \beta_1 - \beta_2 \quad . \tag{A.7}$$

Let $$D = \frac{1}{2}y(k^2 - 1) - \frac{1}{2}(k^2 - 1)\cos 2\Sigma \tag{A.8}$$

and $$C = \frac{1}{2}(k^2 - 1)\sin 2\Sigma \quad . \tag{A.9}$$

Then Eq. (A.6) can be written as

$$\cos(2\beta_2 - A) = [1 - y][1 + \tfrac{1}{2}(k^2 - 1)]/(D^2 + C^2) \quad , \tag{A.10}$$

with $$\sin A = \frac{1}{2}(k^2 - 1)\sin 2\Sigma/(B^2 + C^2) \quad . \tag{A.11}$$

Then, β_2 is known since y and Σ are known, and β_1 is given by (A.7). The total velocity U is given by Eq. (A.3) when U_{eff} and β are known for each wire. The angles β_1 and β_2 can not be less than 20°, or the relation (A.3) does not hold (13,14). The above method reduces to the conventional results for wires mutually perpendicular ($\Sigma = 90°$), which is

$$\cos^2\beta_i = \{[(U^2_{eff})_i/U^2] - 1\} / (k^2 - 1) \quad , \tag{A.12}$$

with $$U^2 = [(U^2_{eff})_i + (U^2_{eff})_j] / (k^2 + 1) \quad . \tag{A.13}$$

Once the total velocity vector U is known with the angles β_1 and β_2, the time average velocities $\overline{u}$ and $\overline{v}$, and the turbulent velocities $u' = u - \overline{u}$ and $v' = v - \overline{v}$, can be determined by

$$u = U \cos(\gamma_1 - \beta_1) = U \cos(\gamma_2 - \beta_2) \tag{A.14}$$

and $$v = U \sin(\gamma_1 - \beta_1) = U \sin(\gamma_2 - \beta_2) \quad . \tag{A.15}$$

The various correlations and moments, like $\overline{u'^2}$, $\overline{v'^2}$, and $\overline{u'v'}$, can be calculated. Frenkiel and Klebanoff (28) showed that the non-linear response of the hot-wire, as given by Eq. (A.1) results in negligible error in even-order correlations when using the method above. Only even-order correlations or moments were computed in this experiment.

The total included angle Σ between the wires was approximately 90° ($\pm$ 1.0°) for each two-wire set. In addition, the individual wires were 45° ($\pm$ 0.5°) from a reference line in the tunnel. This reference line was parallel to the false floor and the walls of the tunnel (see Fig. 9). Both wires were in vertical planes parallel to the tunnel walls and perpendicular to the false floor. The wires were spaced approximately 0.05 in laterally by the probe needle supports.

TABLES

TABLE 1

Average Shear Stress Values From Several Sources (1, 27,57,59) for Circular Cylinders Used for Calibrating Flush Mounted Film.

(Reynolds Number of Cylinder = 10^5, θ is angle from Front Stagnation)

θ	$\tau \times 10^3$
5	1.37
10	2.74
15	4.10
20	5.55
25	6.64
30	7.76
35	8.62

$[\tau] = lb_f/ft^2$

TABLE 2

Effective Skin Friction Coefficient C_f for Waves

	U_∞	Wall-pressure Integration	Strain-gage Balance
Wave A	10.1	0.021	-----
	19.8	0.020	0.018
	40.0	0.021	0.021
Wave B	40.1	0.0195*	-----
Wave C	20.1	0.010	0.017
	39.8	0.011	0.016

* Taken from Ref. 64.

TABLE 3

Summary of Wavy Surface Boundary Layer Parameters

Parameter	Smooth	Wave A Crest				Wave B Crest				Wave C Crest		
	-5	15	20	24	25	15	20	24	25	15	20	25
U_∞, fps	19.2	19.9	20.0	20.1	20.2	19.7	19.9	20.2	20.0	19.5	19.6	19.5
δ, in	8.9	9.0	9.0	9.0	9.0	9.0	9.1	9.1	9.1	9.0	9.0	9.0
δ^*, in	0.7	1.20	1.30	1.34	1.36	0.99	1.15	1.22	1.22	0.95	1.02	1.03
θ, in	0.56	0.85	0.92	0.93	0.94	0.75	0.86	0.88	0.89	0.72	0.73	0.74
H	1.17	1.41	1.43	1.44	1.45	1.32	1.34	1.38	1.37	1.32	1.40	1.39
C_f	.0032	.028	.024	.022	.021	.022	.019	.018	.018	.012	.011	.0105
Δ, ft	1.51	0.83	0.96	1.04	1.01	0.78	0.97	0.93	1.00	0.89	1.13	1.07
G	----	2.3	2.5	2.8	2.8	2.3	2.5	2.6	2.7	2.6	2.7	2.8
$\Delta u/u_*$	0	18.0	17.8	17.4	17.3	16.5	15.9	16.3	16.0	12.4	12.8	11.9
hu_*/ν	0	1620	1560	1500	1500	860	800	810	790	320	310	300
$\varepsilon hu_*/\nu$	0	810	780	750	750	650	600	605	590	320	310	300

TABLE 4 (A)

Wave A Mean Velocity Profiles

1st Crest Height Above Crest (in)	1st Crest $\bar{u}$ (ft/sec)	5th Crest Height Above Crest (in)	5th Crest $\bar{u}$ (ft/sec)	10th Crest Height Above Crest (in)	10th Crest $\bar{u}$ (ft/sec)
.148	12.95	.171	9.83	.106	9.00
.208	17.63	.245	9.99	.173	9.65
.286	18.12	.309	10.26	.244	9.74
.346	18.13	.384	10.80	.319	10.06
.424	18.25	.458	11.55	.397	10.60
.499	18.48	.522	11.42	.457	10.73
.584	18.46	.596	12.09	.535	11.06
.637	18.44	.674	12.64	.599	11.25
.725	18.59	.734	13.01	.673	11.64
.775	18.66	.812	13.32	.748	11.97
.878	18.65	.912	13.52	.811	12.36
.942	18.58	1.011	14.12	.886	12.52
1.052	18.78	1.128	14.62	.950	12.91
1.165	18.83	1.294	15.23	1.027	13.10
1.278	18.85	1.493	15.93	1.137	13.40
1.409	18.91	1.752	16.35	1.240	13.70
1.541	18.83	2.166	17.36	1.339	14.27
1.852	19.02	2.680	17.70	1.463	14.33
2.267	19.10	3.265	18.20	1.552	14.86
2.770	19.10	4.016	18.38	1.676	15.21
3.408	19.22	4.665	18.60	1.818	15.38
4.124	19.27	5.388	18.75	3.009	17.63
4.812	19.48	6.731	18.97	4.462	18.82
5.552	19.38	7.911	19.04	5.805	19.12
6.931	19.55	9.180	19.10	7.120	19.39
7.984	19.52	10.867	19.23	8.899	19.53
9.057	19.62	14.244	19.26	10.724	19.66
10.929	19.76			12.670	19.74
14.412	19.74				

TABLE 4 (A) - (Continued)

15th Crest		20th Crest		24th Crest	
Height Above Crest (in)	$\bar{u}$ (ft/sec)	Height Above Crest (in)	$\bar{u}$ (ft/sec)	Height Above Crest (in)	$\bar{u}$ (ft/sec)
.068	8.64	.043	8.85	.051	8.49
.157	9.72	.121	9.45	.189	10.24
.210	9.92	.192	9.75	.341	10.55
.295	10.22	.259	10.14	.480	11.04
.359	10.67	.333	10.53	.625	11.52
.433	10.81	.408	10.84	.781	11.95
.497	11.25	.468	10.94	.908	12.59
.568	11.70	.546	11.47	1.082	12.97
.650	11.89	.617	11.48	1.298	13.73
.720	12.01	.684	11.62	1.511	13.93
.791	12.39	.759	11.81	1.734	14.49
.873	12.55	.844	12.31	3.418	17.17
.951	12.93	.911	12.47	5.374	19.10
1.036	13.06	1.010	12.98	7.132	19.72
1.139	13.23	1.124	13.67	8.769	19.84
1.252	13.56	1.212	13.19	10.669	19.98
1.351	13.88	1.326	13.78	12.331	19.96
1.450	14.17	1.397	13.87		
1.603	14.64	1.503	14.15		
1.716	14.85	1.613	14.49		
2.443	16.44	1.701	14.48		
3.456	17.78	2.602	16.11		
4.924	19.10	3.558	17.71		
6.238	19.31	5.100	19.05		
8.159	19.51	7.007	19.39		
9.836	19.60	8.726	19.74		
11.618	19.74	10.551	19.81		
13.341	19.80	12.270	19.97		

TABLE 4 (A) - (Continued)

25th Crest	
Height Above Crest (in)	$\bar{u}$ (ft/sec)
.065	5.67
.139	10.02
.203	10.73
.277	10.55
.352	11.01
.416	11.41
.490	11.50
.568	11.72
.646	11.95
.703	12.36
.781	12.56
.855	12.80
.919	12.86
.979	13.32
1.089	13.18
1.195	13.56
1.309	13.96
1.419	14.24
1.521	14.44
1.645	14.68
1.738	14.69
2.074	15.35
3.464	17.82
5.094	19.14
7.153	19.96
8.733	20.04
10.583	20.11
12.164	20.21

TABLE 4 (B)

Wave B Mean Velocity Profiles

1st Crest		5th Crest		10th Crest	
Height Above Crest (in)	$\bar{u}$ (ft/sec)	Height Above Crest (in)	$\bar{u}$ (ft/sec)	Height Above Crest (in)	$\bar{u}$ (ft/sec)
.356	15.12	.244	11.75	.032	11.16
.427	15.34	.418	12.53	.121	11.52
.516	15.75	.545	13.40	.184	11.84
.643	16.02	.697	13.89	.248	12.15
.792	16.16	.861	14.94	.323	12.39
.969	16.53	1.098	15.74	.411	12.91
1.182	16.72	1.300	16.36	.461	13.07
1.409	16.90	1.498	16.86	.574	13.50
1.621	17.09	1.711	17.03	.677	13.91
1.830	17.36	2.080	17.61	.780	14.32
2.171	17.49	2.679	17.96	.886	14.41
2.670	17.69	4.096	18.56	.985	14.73
4.258	18.37	7.474	19.01	1.109	15.49
7.129	18.80	11.340	19.27	1.223	15.56
10.595	19.10	14.810	19.26	1.318	15.83
13.196	19.20			1.435	16.22
				1.563	16.47
				1.779	16.88
				1.939	17.01
				2.243	17.58
				2.984	18.09
				4.040	18.61
				5.514	18.97
				7.294	19.11
				9.041	19.39
				10.848	19.41
				12.539	19.46

TABLE 4 (B) - (Continued)

15th Crest Height Above Crest (in)	15th Crest $\bar{u}$ (ft/sec)	20th Crest Height Above Crest (in)	20th Crest $\bar{u}$ (ft/sec)	24th Crest Height Above Crest (in)	24th Crest $\bar{u}$ (ft/sec)
.014	9.90	.033	10.36	.183	10.44
.074	10.08	.082	10.16	.336	10.87
.145	10.60	.157	10.55	.439	11.11
.213	10.87	.231	10.80	.559	11.79
.287	11.14	.306	11.07	.672	12.08
.365	11.77	.383	11.35	.821	12.62
.425	12.01	.447	11.92	.924	12.91
.503	12.22	.511	11.73	1.013	13.29
.602	12.75	.585	12.34	1.339	14.09
.716	13.23	.660	12.44	1.576	14.37
.815	13.40	.731	13.00	2.342	16.27
.918	13.84	.834	13.23	3.373	17.76
1.028	14.01	.947	13.43	5.014	19.23
1.155	14.38	1.043	13.88	6.729	19.72
1.244	14.74	1.153	14.02	8.459	19.98
1.343	14.77	1.262	14.35	10.376	20.01
1.457	15.09	1.376	14.39	12.268	20.16
1.722	15.83	1.496	14.61	13.931	20.18
2.041	16.49	1.879	15.59		
2.374	16.88	2.230	16.42		
3.324	18.35	2.559	16.97		
4.409	18.82	2.917	17.11		
5.851	19.16	4.324	18.66		
7.566	19.37	5.770	19.25		
9.257	19.49	7.539	19.54		
11.022	19.58	9.343	19.65		
12.960	19.65	11.334	19.71		
		12.862	19.78		

TABLE 4 (B) - (Continued)

25th Crest

Height Above Crest (in)	$\overline{u}$ (ft/sec)
.105	10.29
.151	10.64
.193	10.70
.232	10.69
.279	10.87
.317	10.99
.353	11.04
.442	11.56
.512	11.75
.594	12.04
.661	12.20
.743	12.48
.807	12.77
.870	12.99
.945	13.32
1.044	13.50
1.122	13.53
1.232	14.11
1.345	14.16
1.480	14.39
1.639	14.95
1.788	15.01
1.997	15.56
2.199	15.74
4.003	18.14
5.804	19.36
7.515	19.64
9.326	19.72
11.633	19.76

TABLE 4 (C)

Wave C Mean Velocity Profiles

1st Crest		5th Crest		10th Crest	
Height Above Crest (in)	$\overline{u}$ (ft/sec)	Height Above Crest (in)	$\overline{u}$ (ft/sec)	Height Above Crest (in)	$\overline{u}$ (ft/sec)
.219	13.94	.141	11.49	.191	11.78
.297	14.84	.283	12.47	.330	12.29
.346	15.22	.431	13.37	.468	12.97
.445	15.77	.570	14.02	.620	13.45
.608	16.21	.708	14.68	.744	13.96
.736	16.66	.857	15.33	.918	14.26
.888	16.81	1.059	15.89	1.046	14.85
1.037	16.95	1.332	16.75	1.237	15.63
1.207	17.15	1.736	17.14	1.450	15.83
1.526	17.43	2.076	17.55	1.634	16.21
1.884	17.37	2.402	17.77	1.960	16.88
2.228	17.87	2.941	18.09	2.187	17.35
2.593	17.94	3.628	18.40	2.424	17.44
3.121	18.17	4.716	18.79	2.562	17.69
3.823	18.47	6.095	18.98	3.239	18.16
4.875	18.58	7.860	19.24	3.991	18.51
5.949	18.84	9.692	19.32	4.990	18.81
7.867	18.95	11.411	19.46	6.085	18.87
9.522	19.26	13.193	19.39	7.893	19.21
11.311	19.31			9.597	19.37
13.041	19.42			11.476	19.53
14.806	19.38			13.123	19.57

TABLE 4 (C) - (Continued)

15th Crest		20th Crest		25th Crest	
Height Above Crest (in)	$\overline{u}$ (ft/sec)	Height Above Crest (in)	$\overline{u}$ (ft/sec)	Height Above Crest (in)	$\overline{u}$ (ft/sec)
.199	11.18	.105	10.99	.156	11.54
.394	12.44	.343	12.01	.333	12.35
.578	13.34	.509	12.64	.521	12.82
.763	13.71	.686	13.62	.687	13.63
.954	14.39	1.073	14.64	.861	14.15
1.117	15.02	1.218	14.72	1.035	14.28
1.287	15.11	1.409	15.21	1.223	14.65
1.478	15.72	1.562	15.23	1.400	14.89
1.631	15.87	1.760	15.75	1.577	15.46
1.904	16.37	1.952	16.11	1.853	15.92
2.180	16.82	2.203	16.52	2.123	16.39
2.496	17.17	2.427	16.62	2.424	16.57
2.907	17.65	2.753	17.04	2.743	17.12
3.172	17.92	3.054	17.53	3.094	17.27
3.502	18.14	3.468	18.04	3.459	17.60
3.874	18.34	3.816	18.09	3.796	18.00
4.955	18.82	4.833	18.58	4.887	18.63
6.054	18.92	5.900	18.94	5.925	19.09
7.436	19.22	7.339	19.11	7.357	19.13
9.172	19.33	9.167	19.26	9.122	19.39
11.026	19.47	10.890	19.41	10.852	19.46
13.790	19.52	12.644	19.45	12.723	19.46

FIGURES

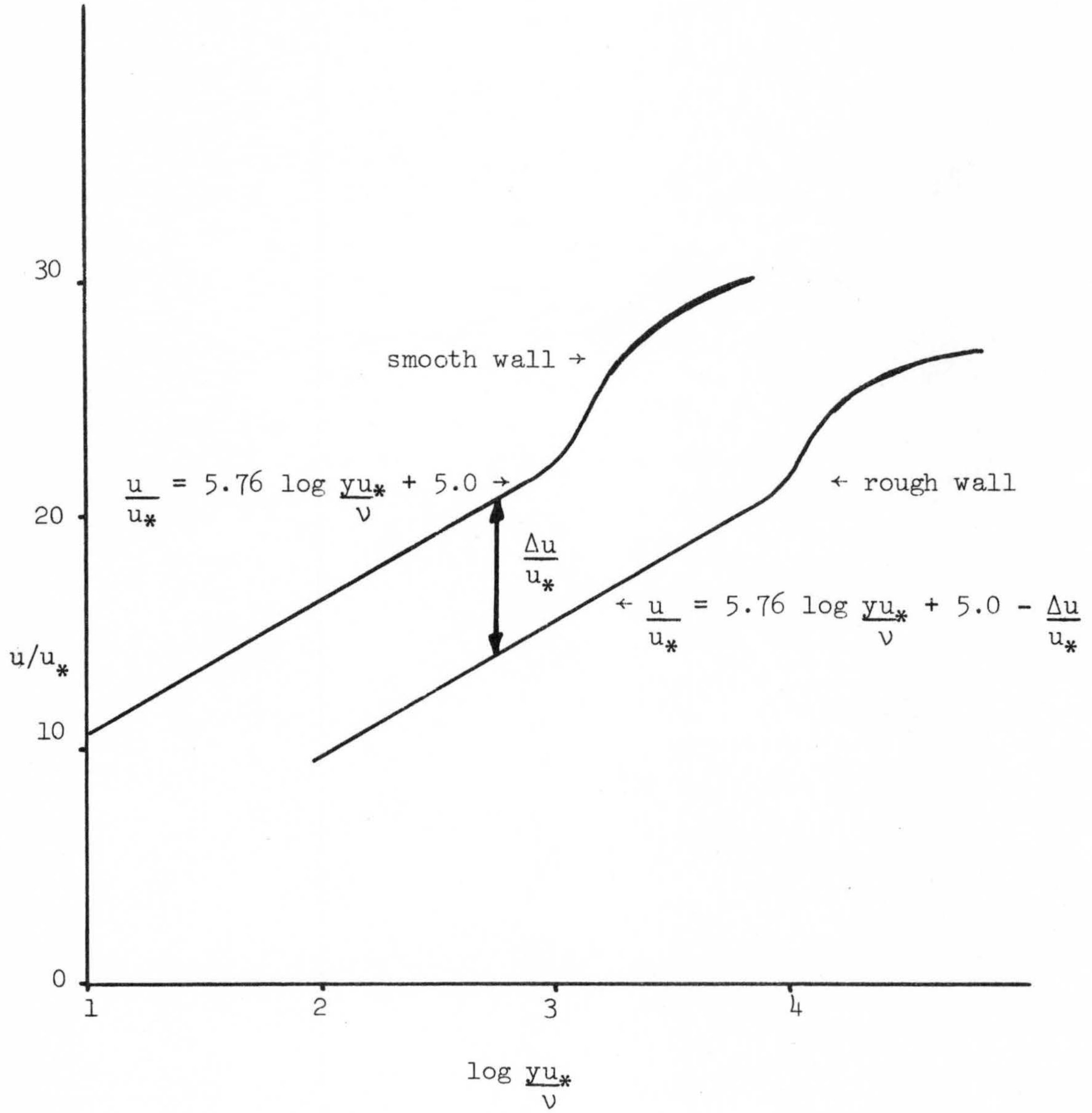

Fig. 1. Smooth and Rough Wall Velocity Profiles.

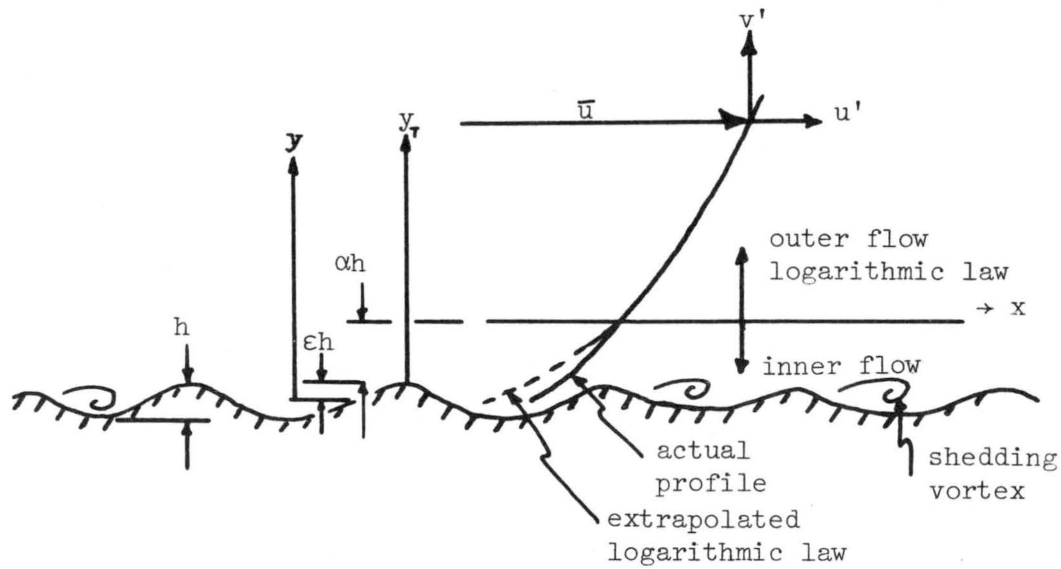

Fig. 2. Rough Wall Flow.

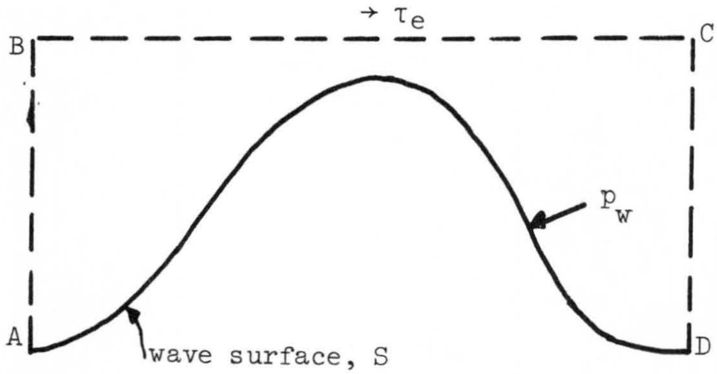

τ_e is "effective wall shear stress"

Fig. 3. Control Volume for "Effective Wall Shear Stress" Determination.

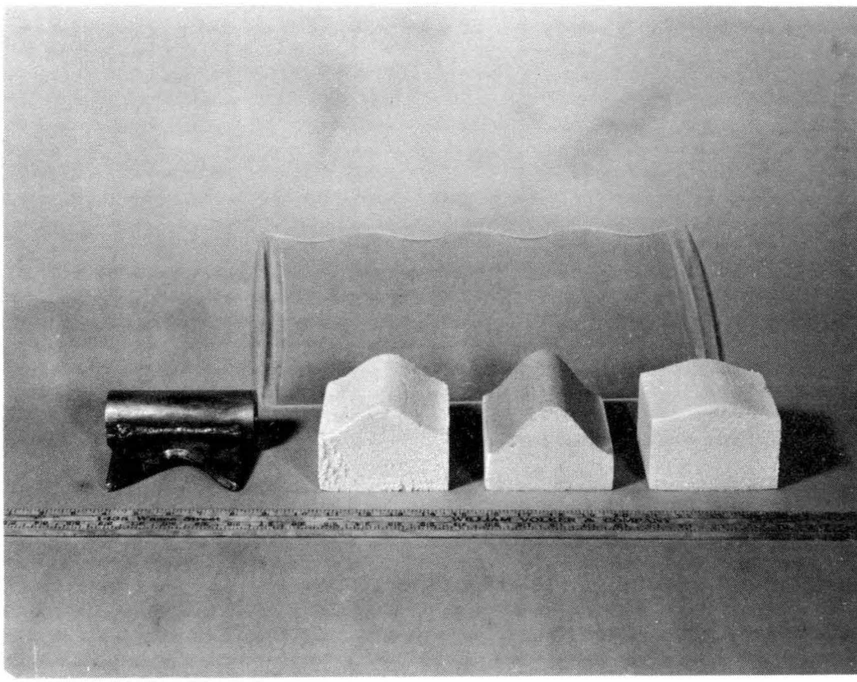

Fig. 4. Waves, Mill Cutter, Plexiglas Wave Form.

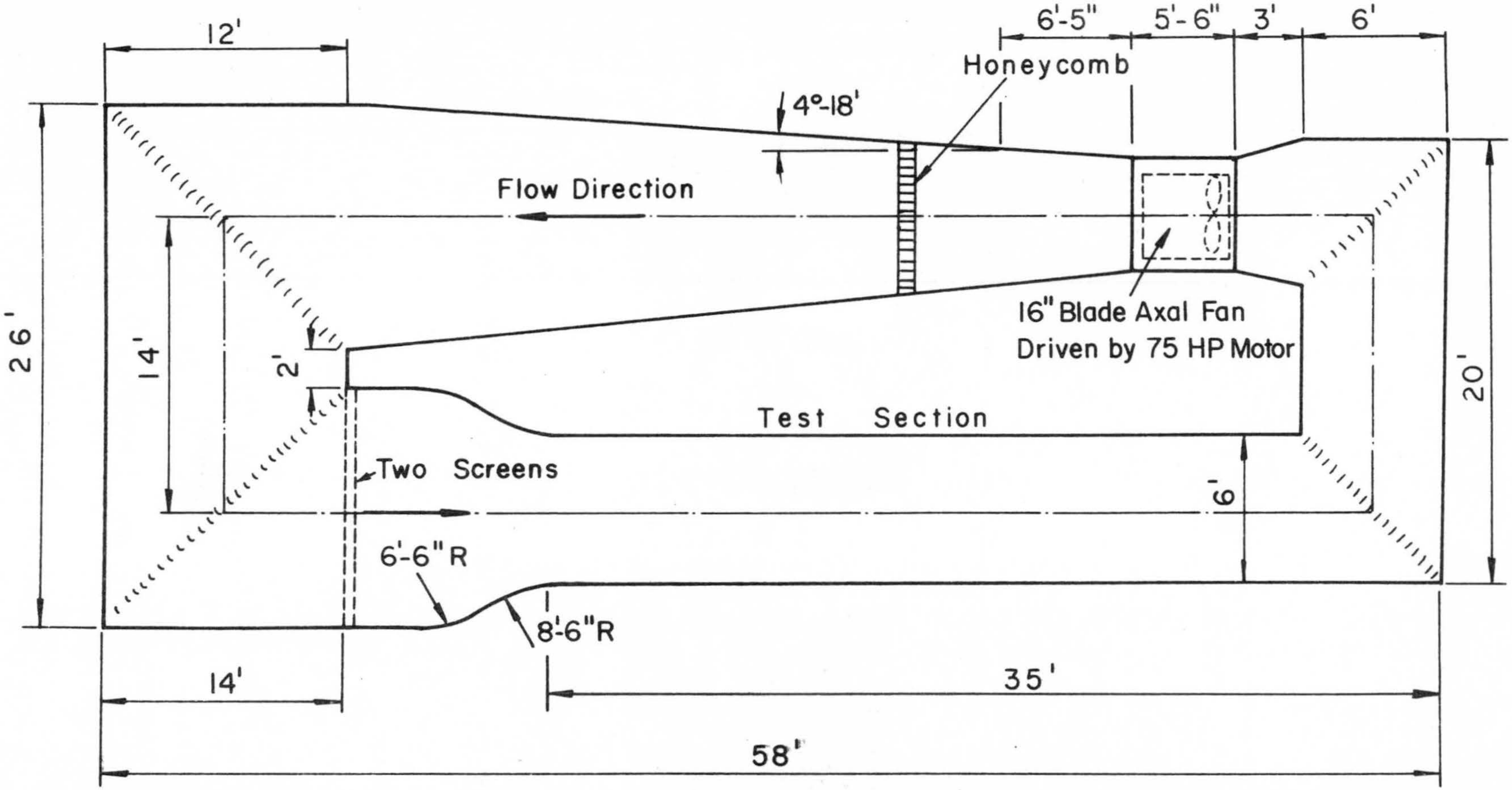

Fig. 5. Wind tunnel: Plan view.

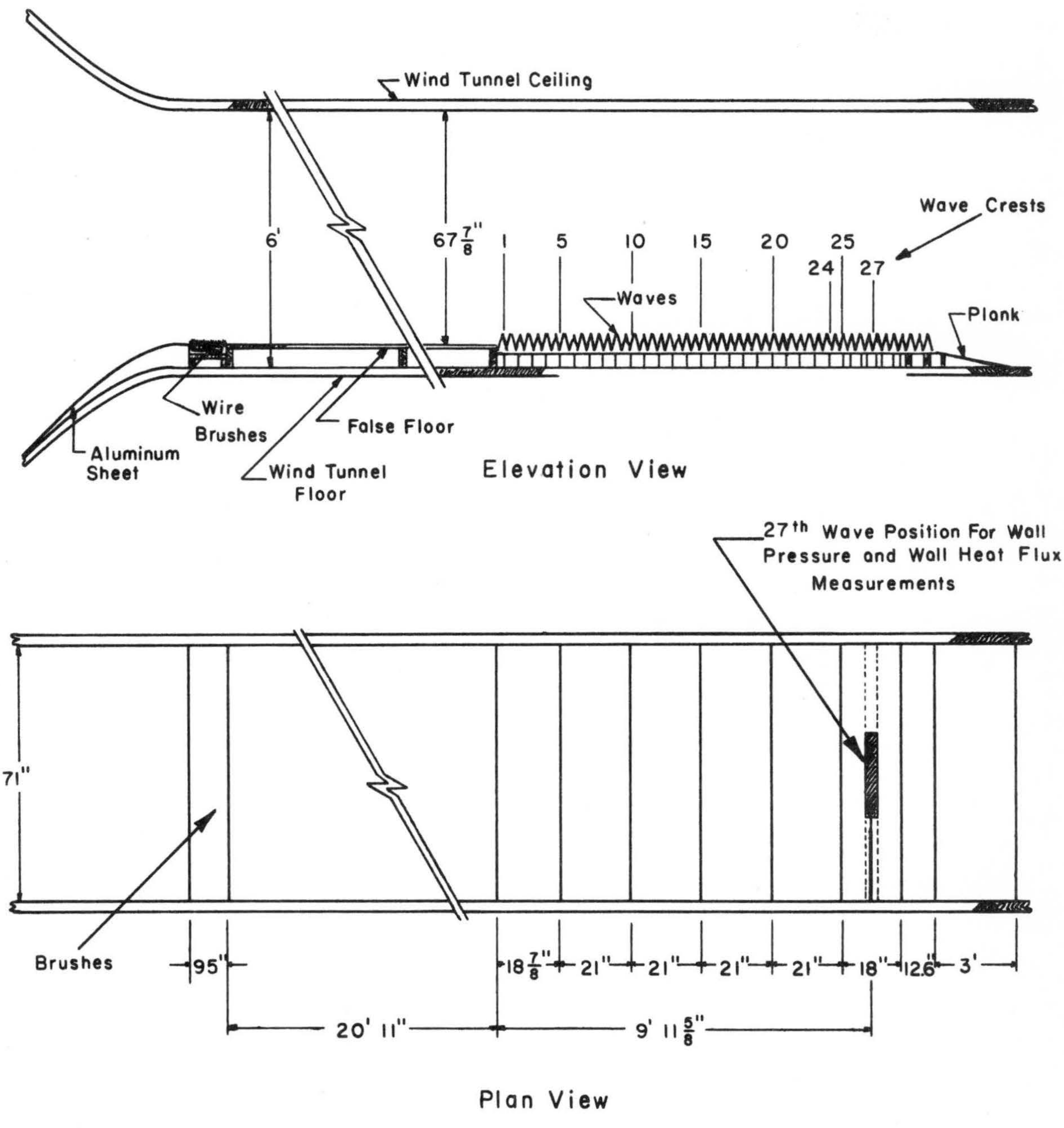

Fig. 6. Experimental set up in wind tunnel.

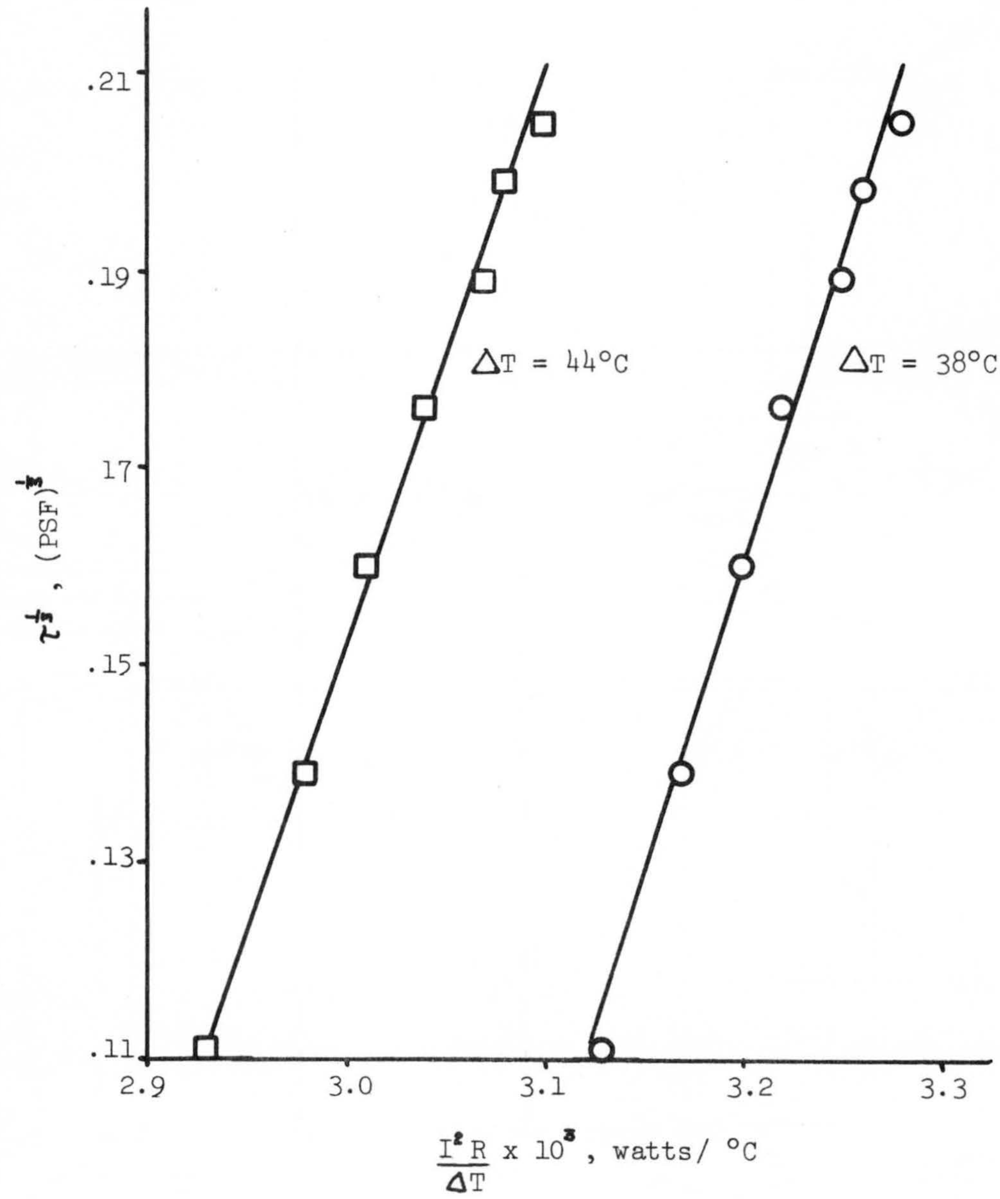

Fig. 7. Typical Hot-film Calibrations.

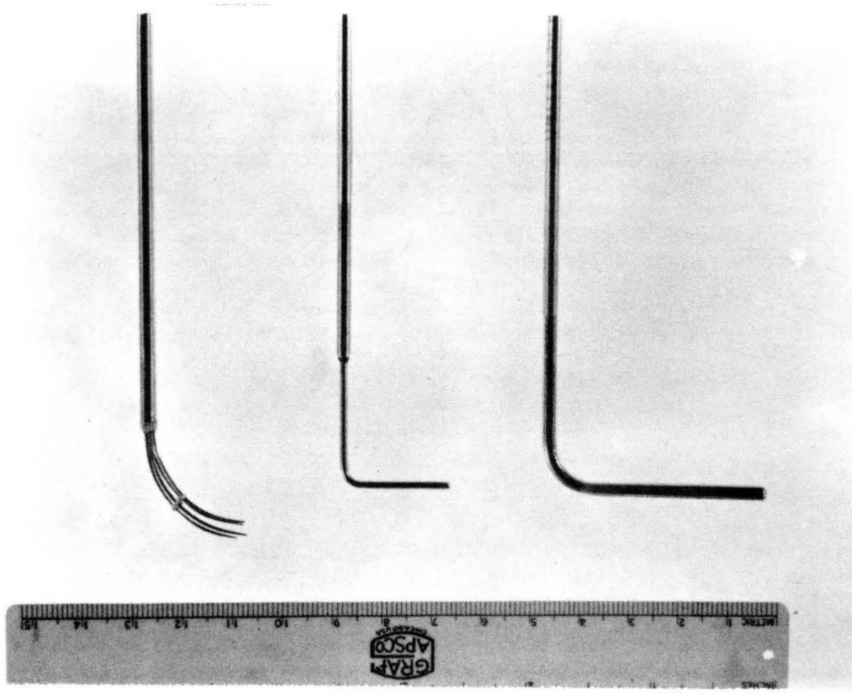

Fig. 8. Reference Pitot-Static Tube,
Profile Pitot-Static Probe and
Two-Wire Probe.

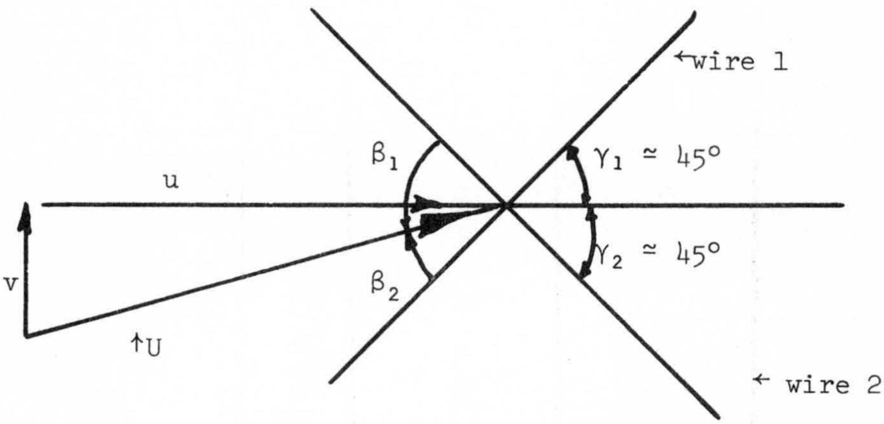

Fig. 9. Velocity Determination.

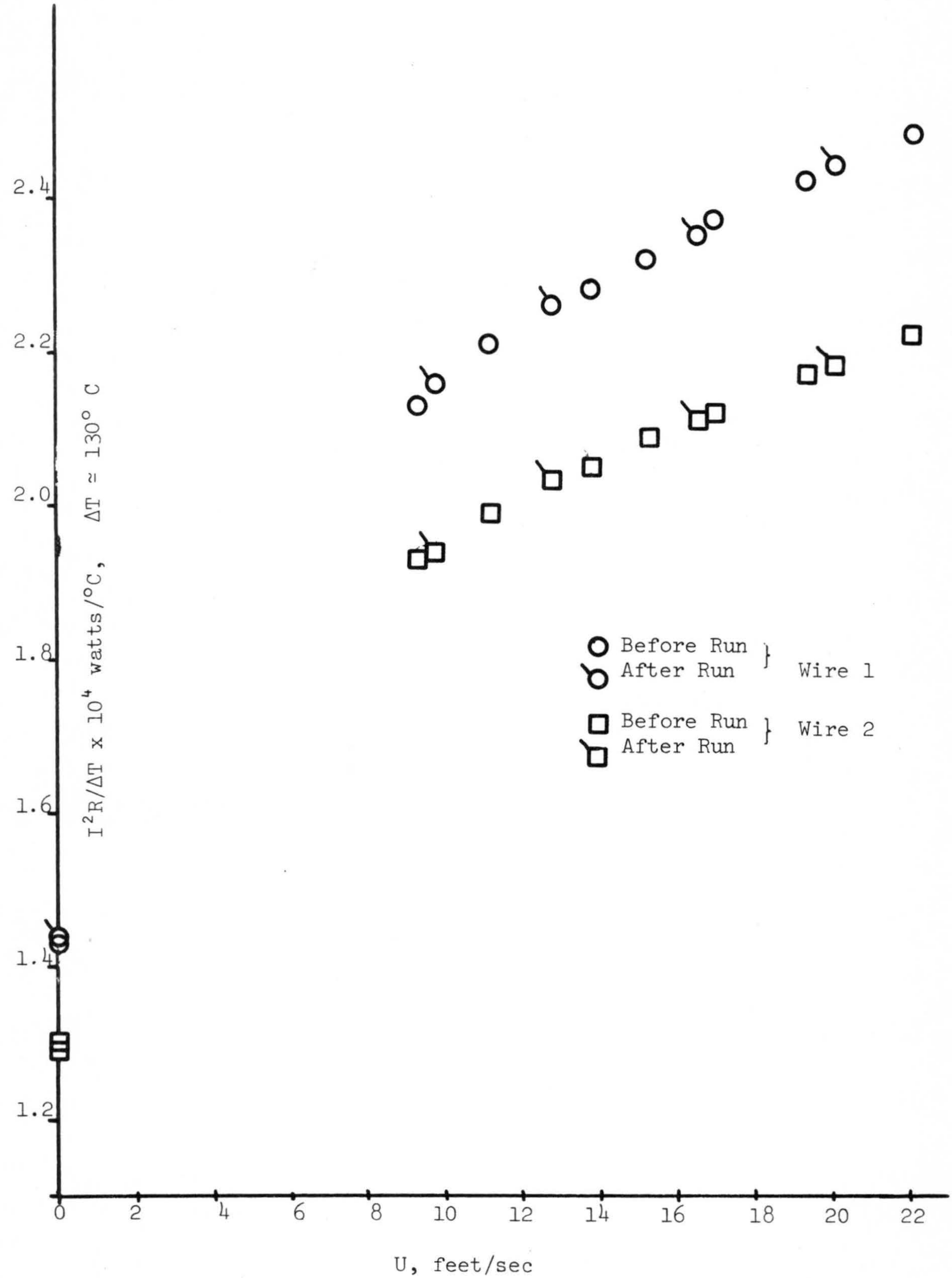

Fig. 10. Typical Hot-Wire Calibrations.

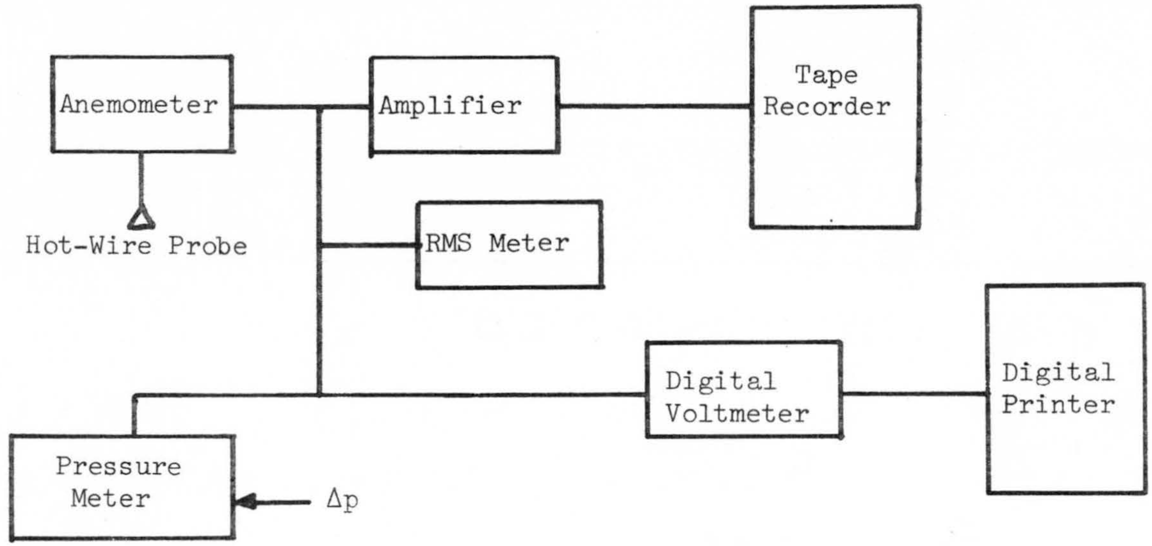

Fig. 11. Block Diagram of Data Acquisition System.

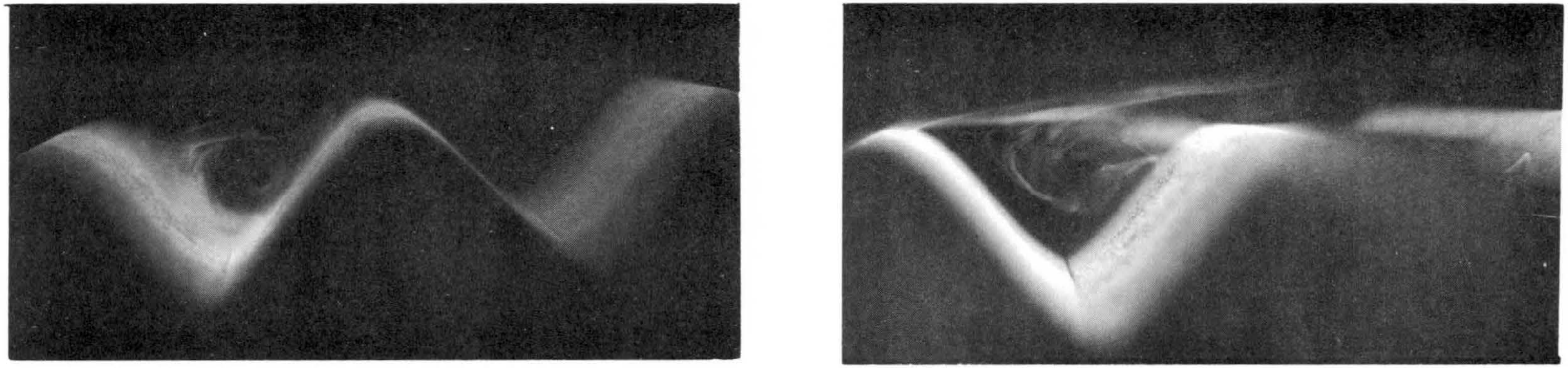

Fig. 12. Photographs of visualization study, Wave A.

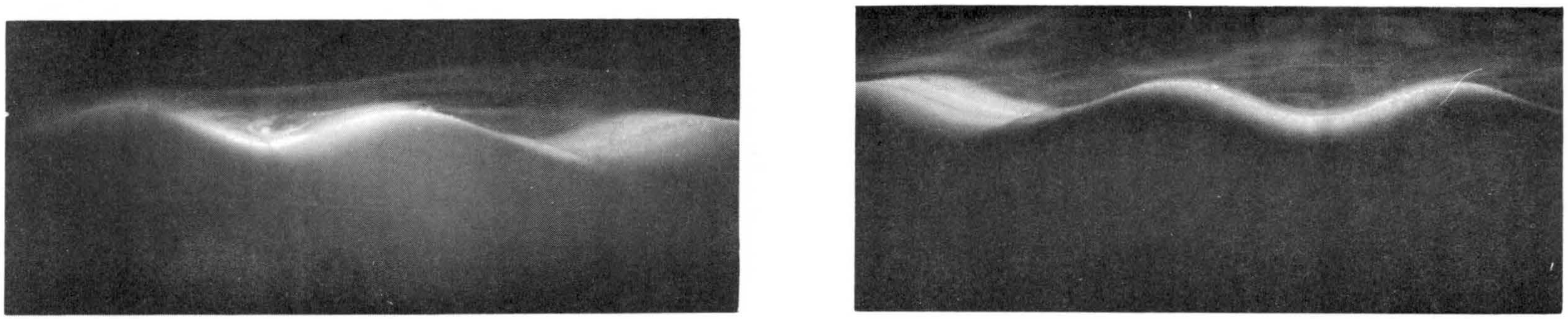

Fig. 13. Photographs of visualization study, Wave C.

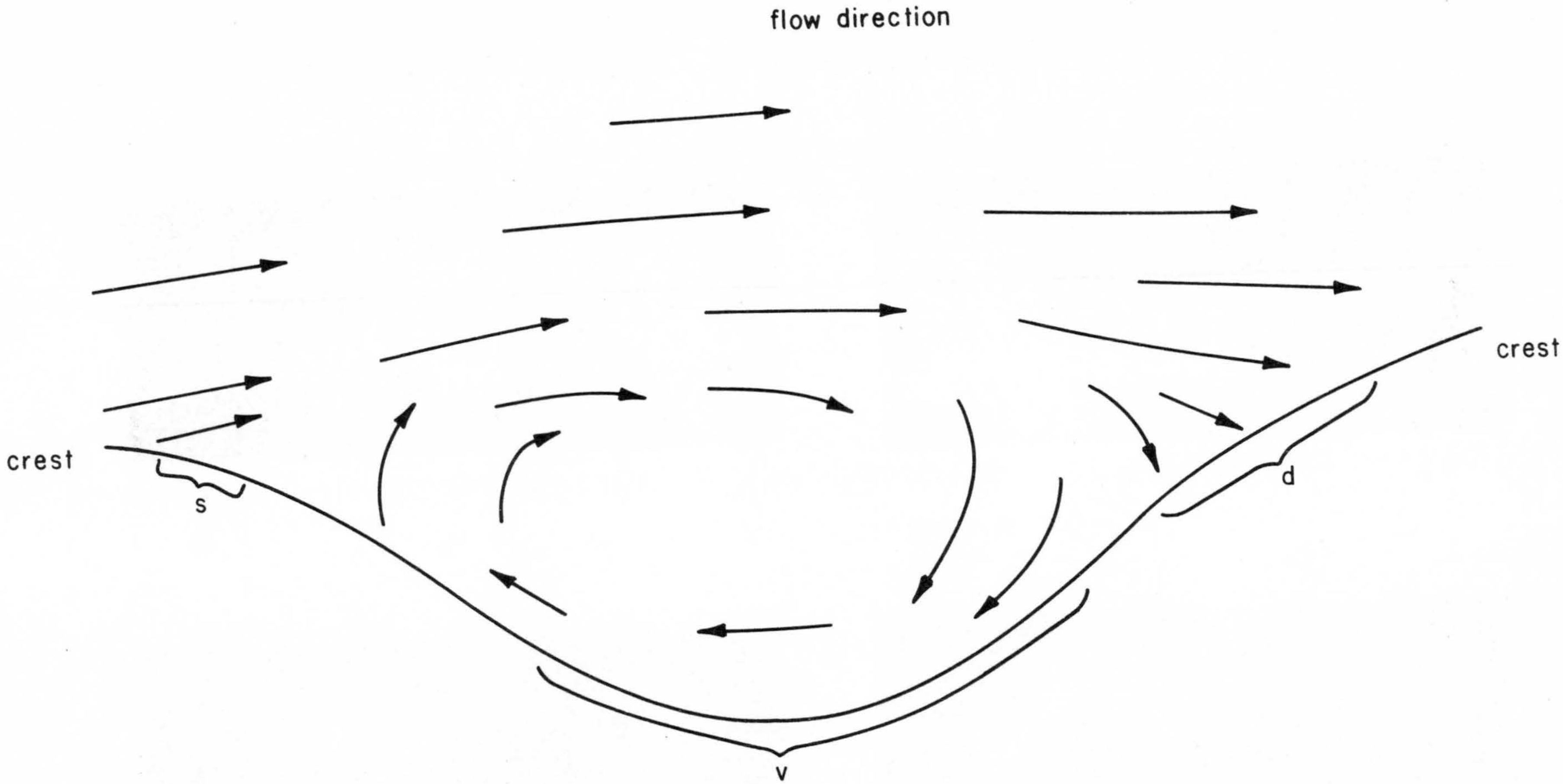

Fig. 14. General Flow Pattern.

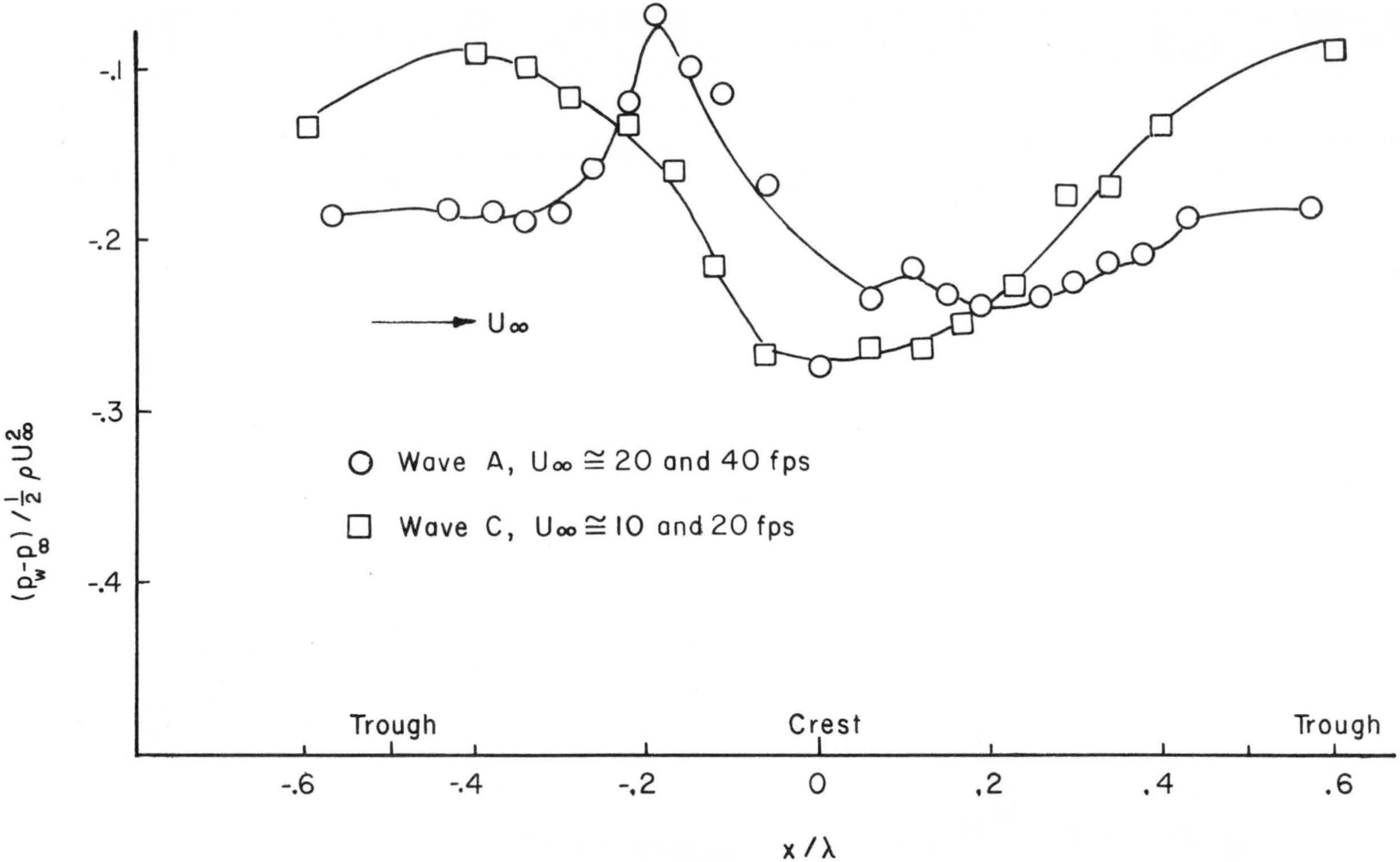

Fig. 15. Wall Pressure Coefficients.

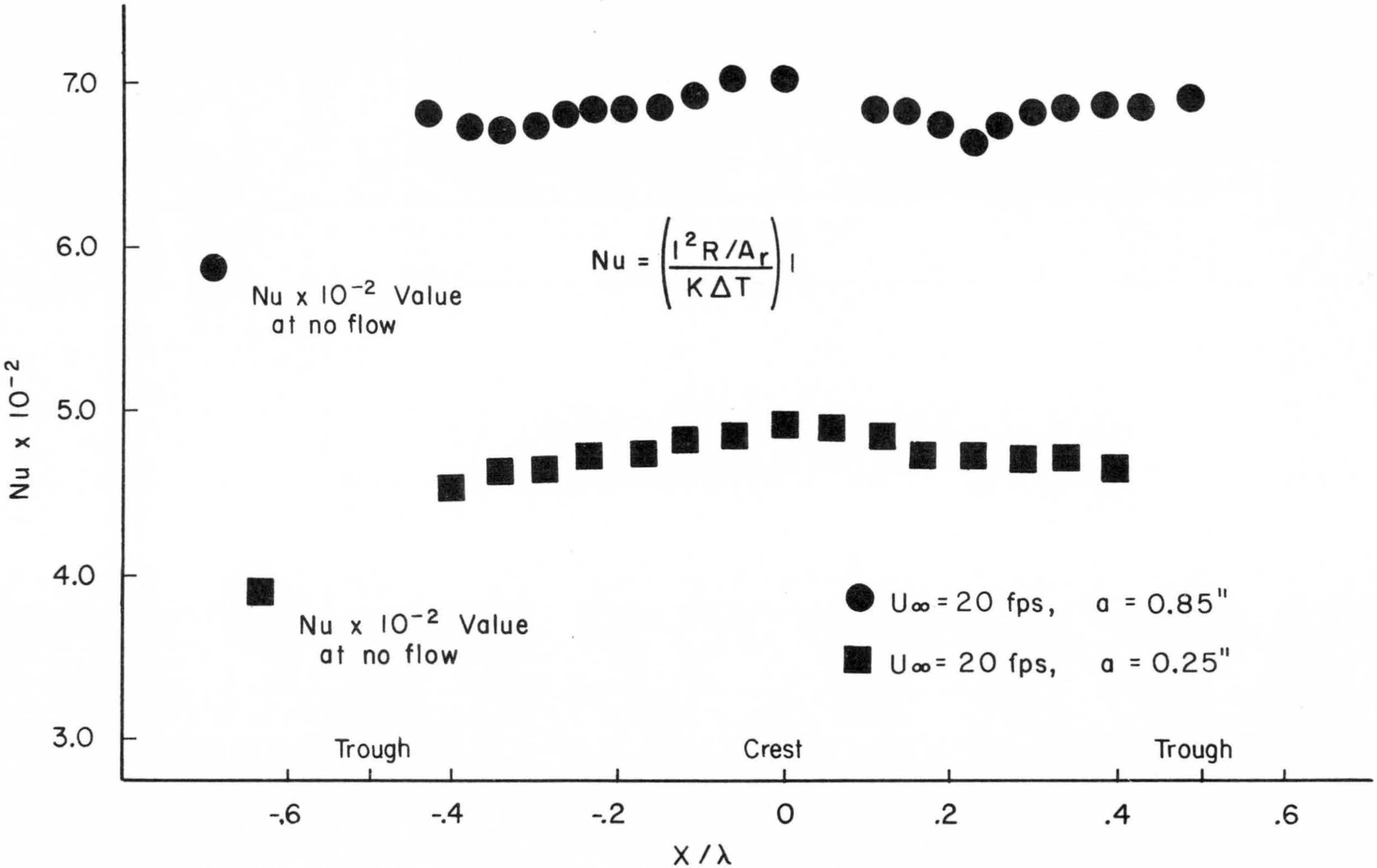

Fig. 16. Local variation of heat loss from a point source.

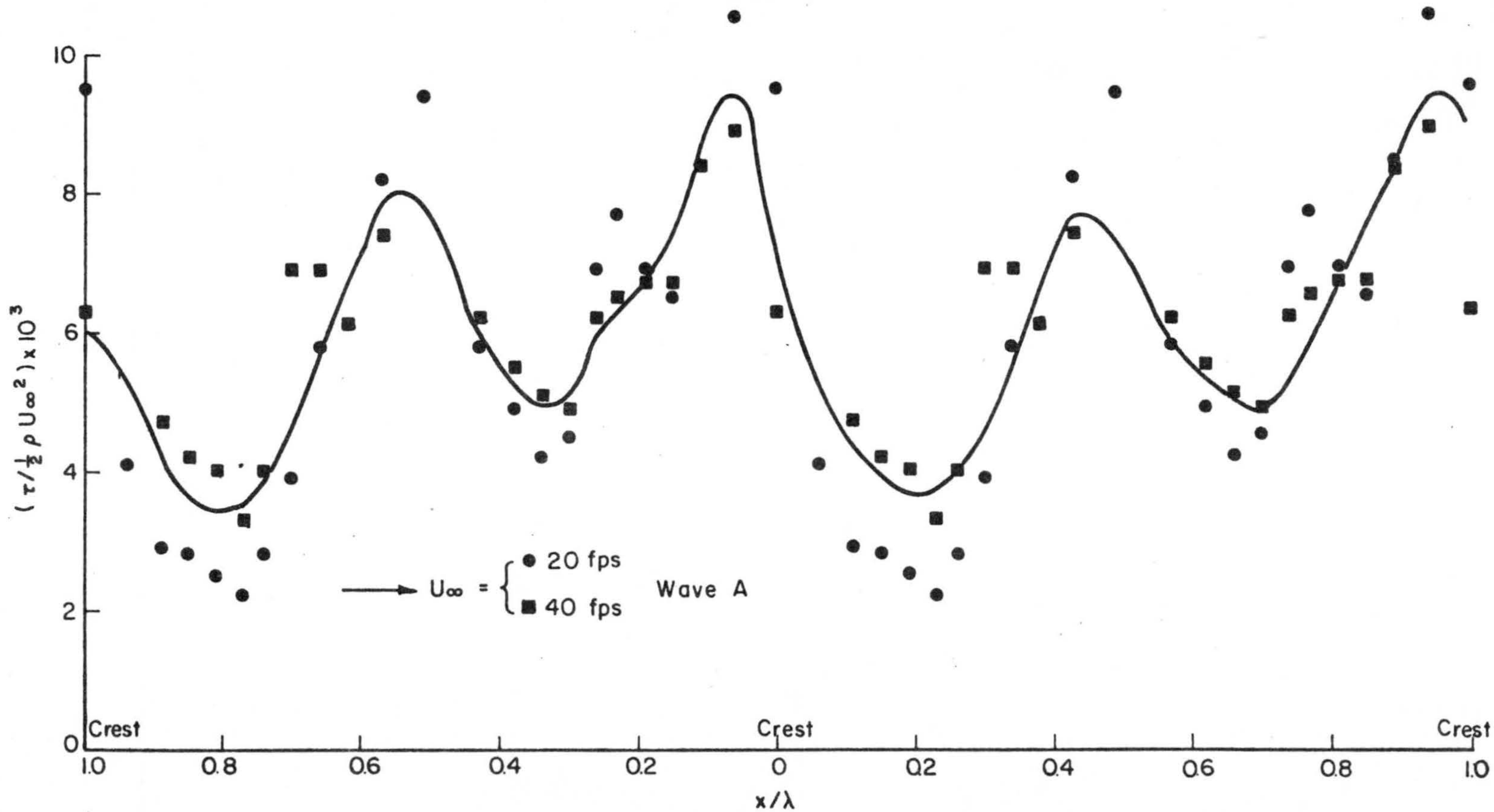

Fig. 17. Wall "shear-stress" profiles (waves), wave A.

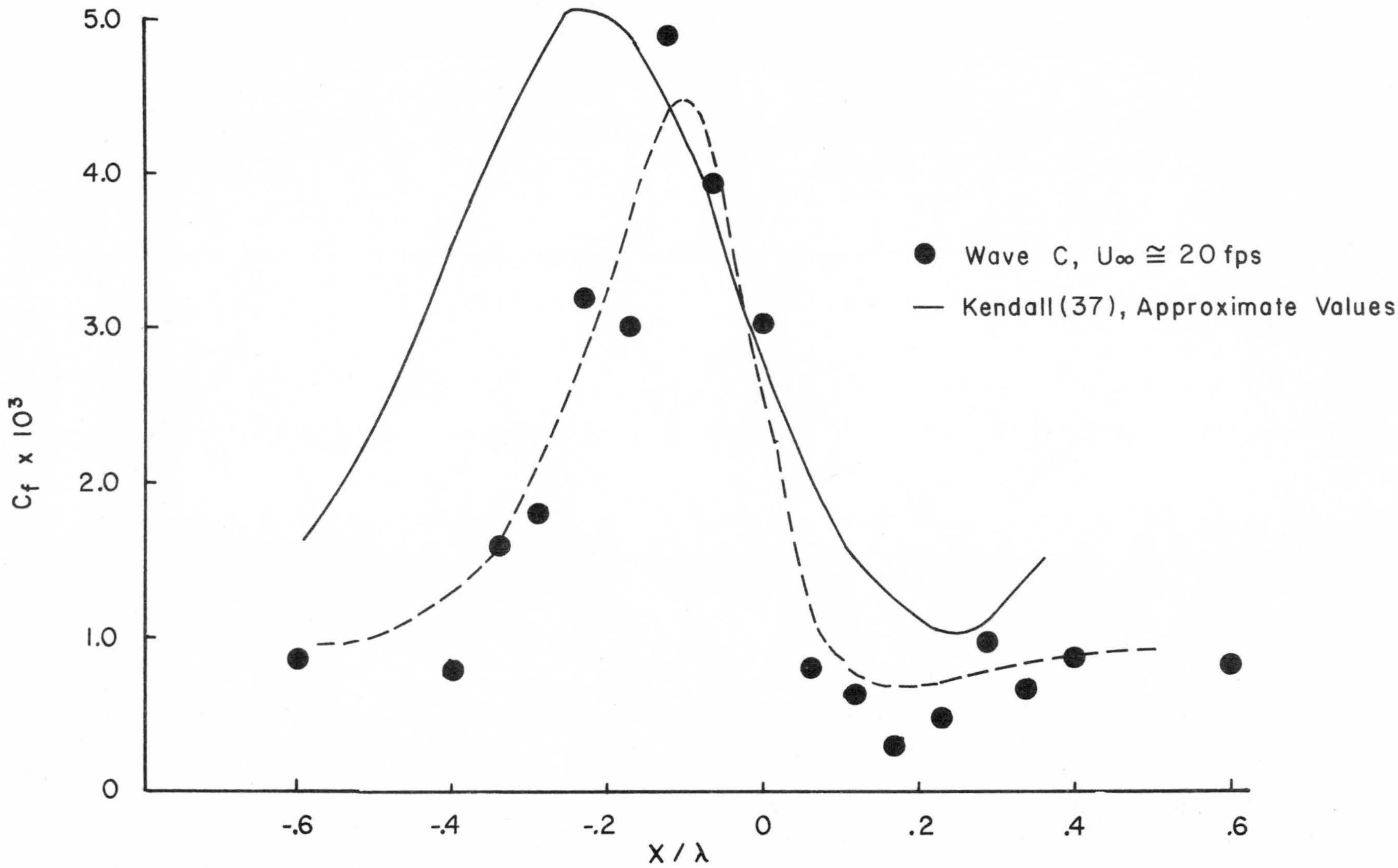

Fig. 18. Wall "shear stress" profile, Wave C.

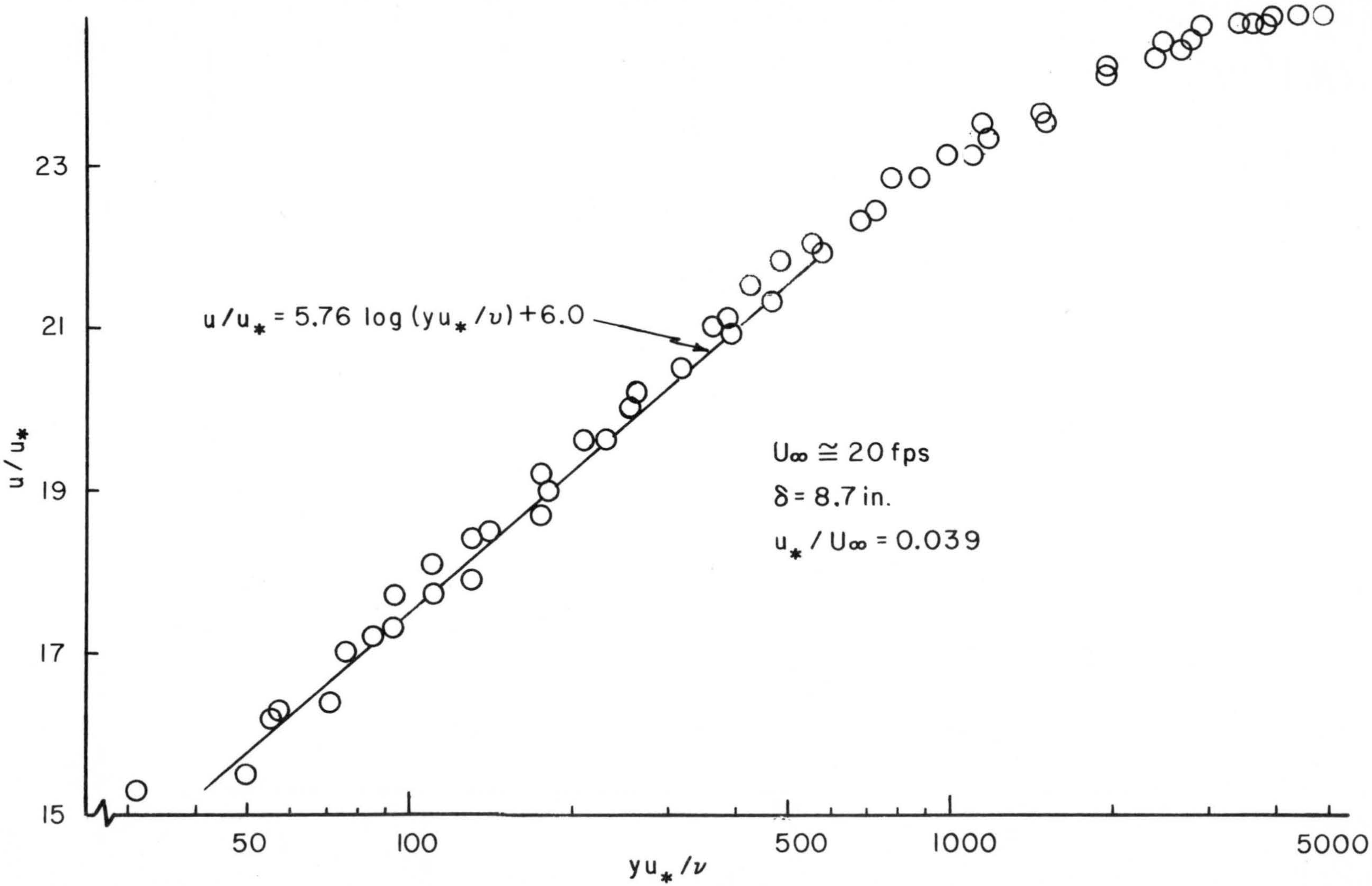

Fig. 19. Mean velocity profile, smooth surface.

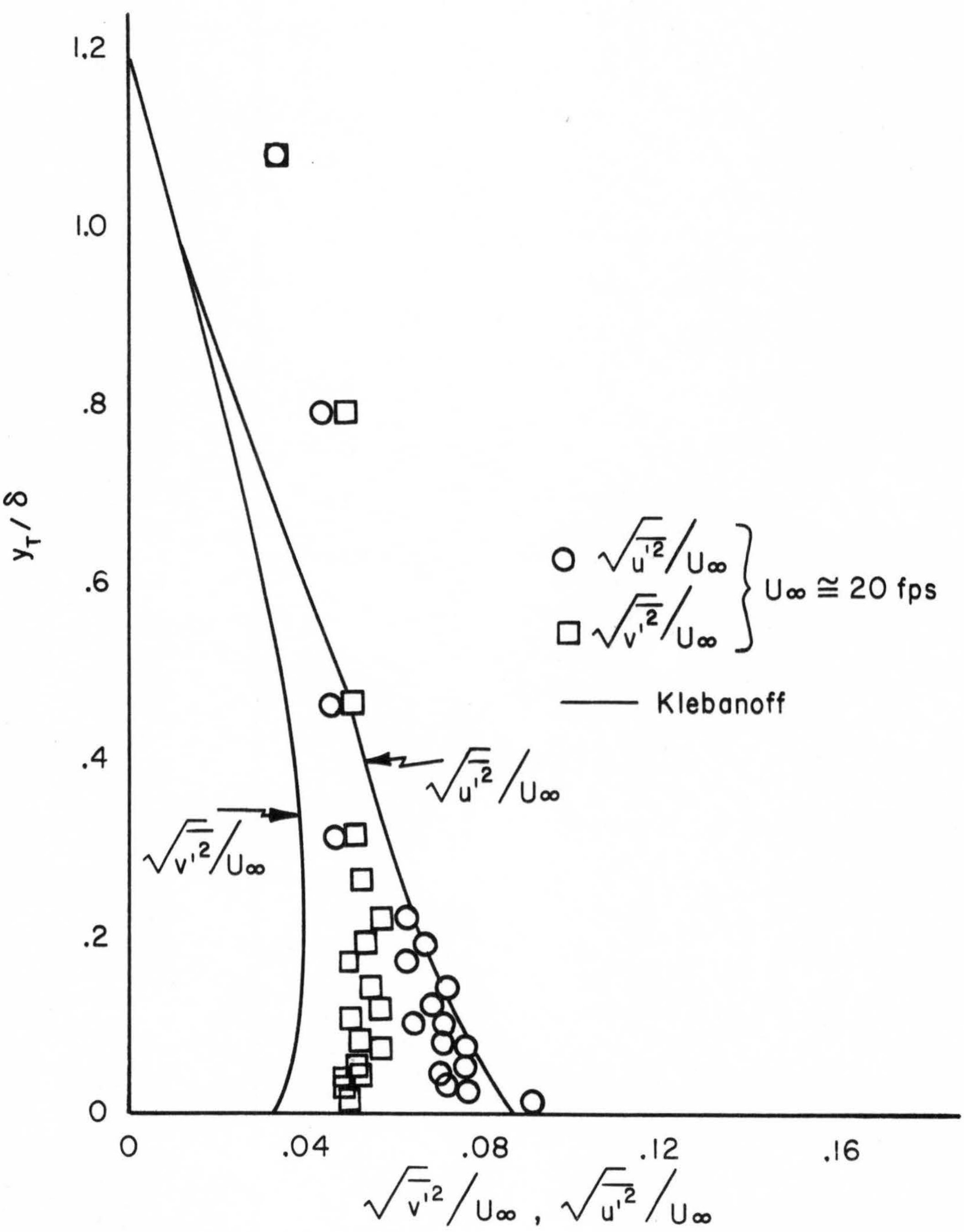

Fig. 20. Turbulence intensities, smooth surface.

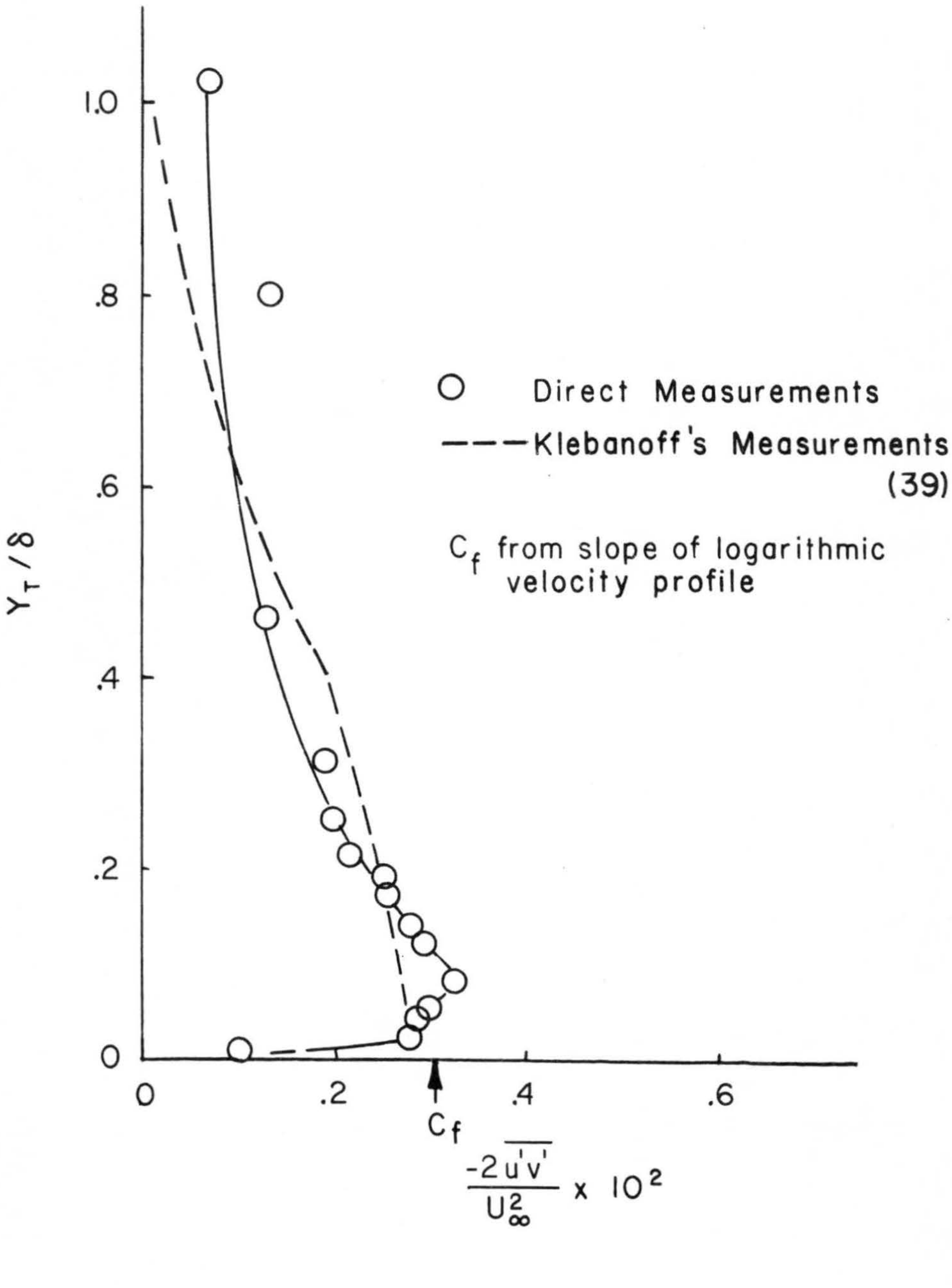

Fig. 21. Reynolds shear stress, smooth surface.

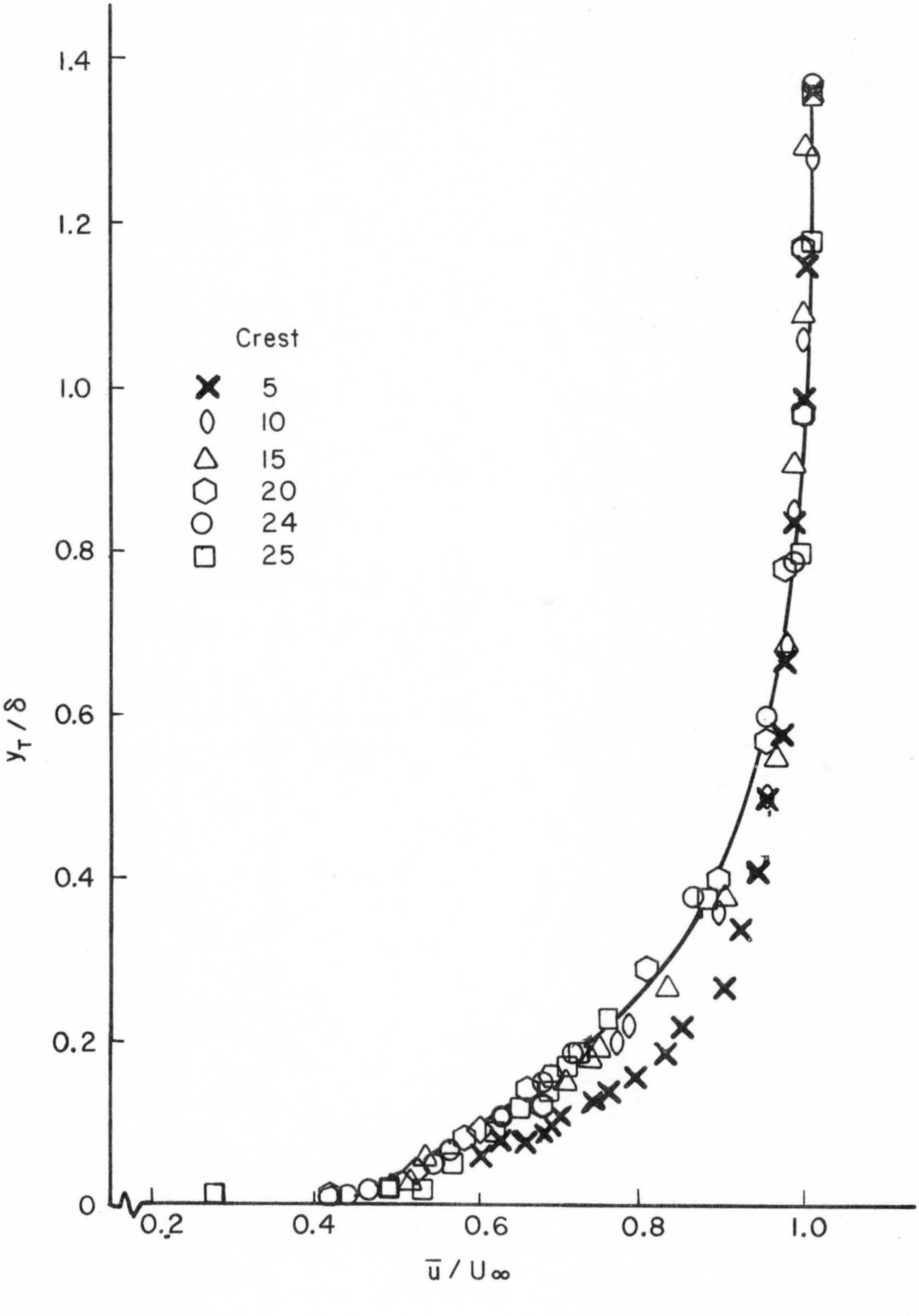

Fig. 22. Mean velocity profiles, wave A.

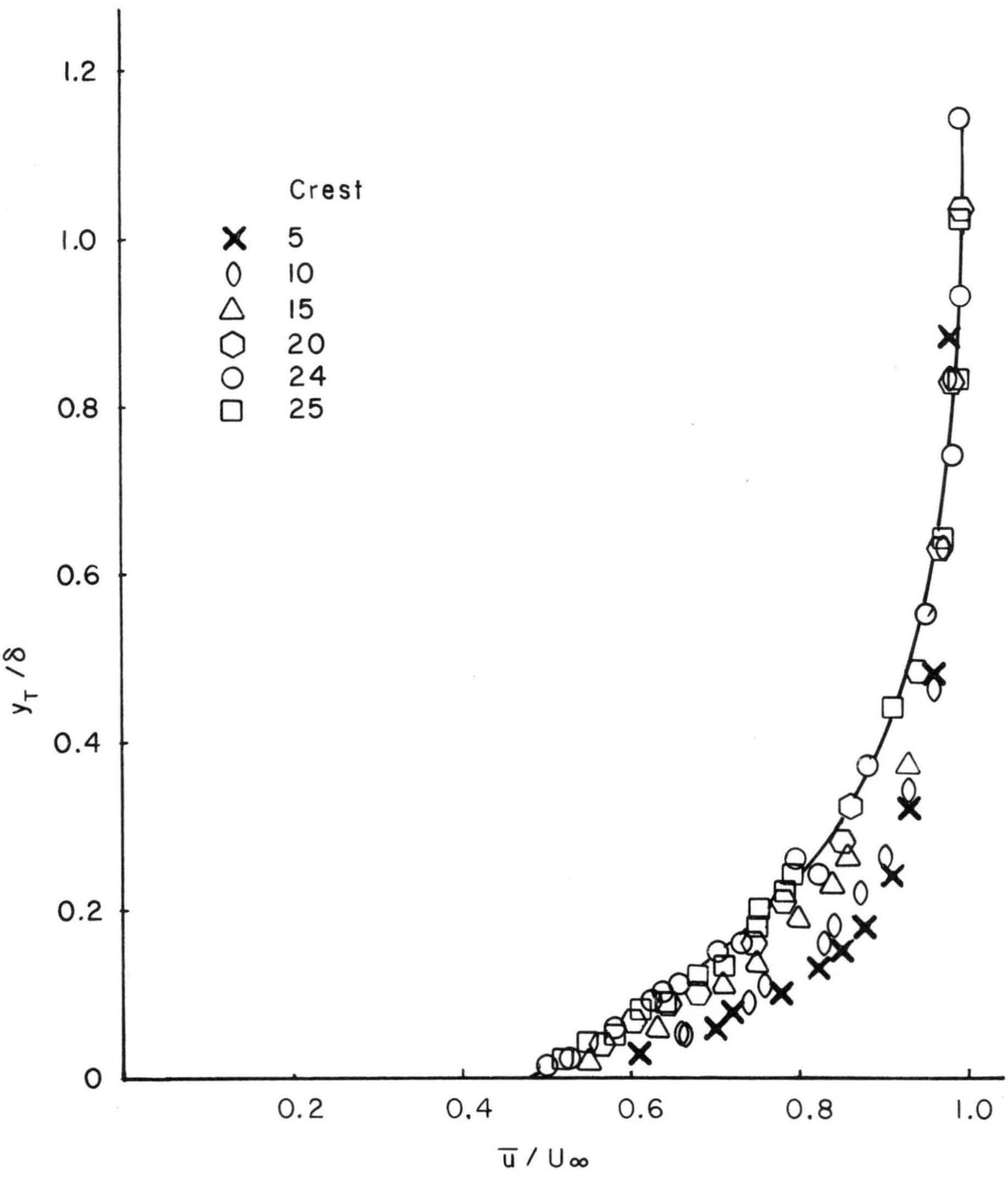

Fig. 23. Mean velocity profile, Wave B.

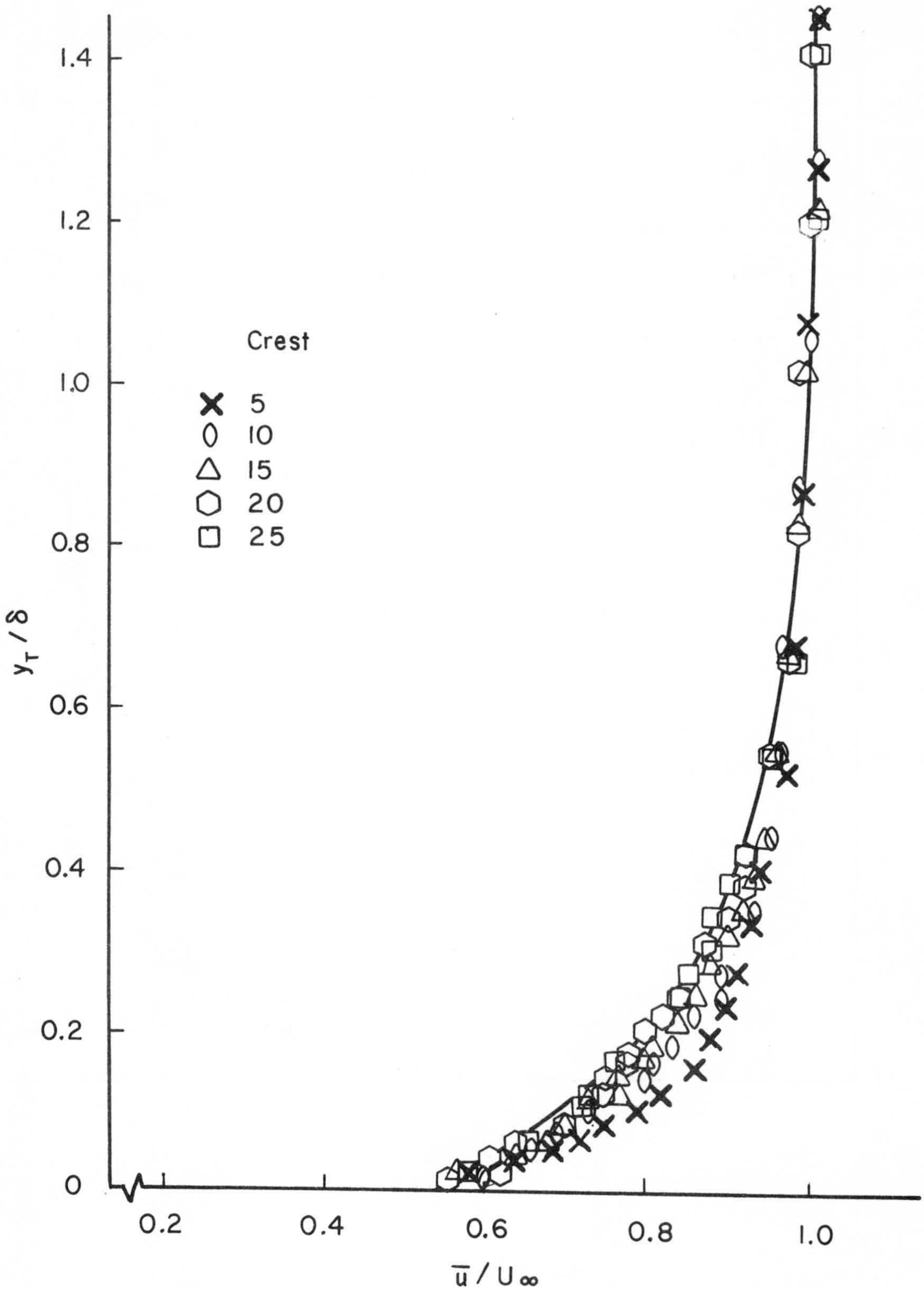

Fig. 24. Mean velocity profile, Wave C.

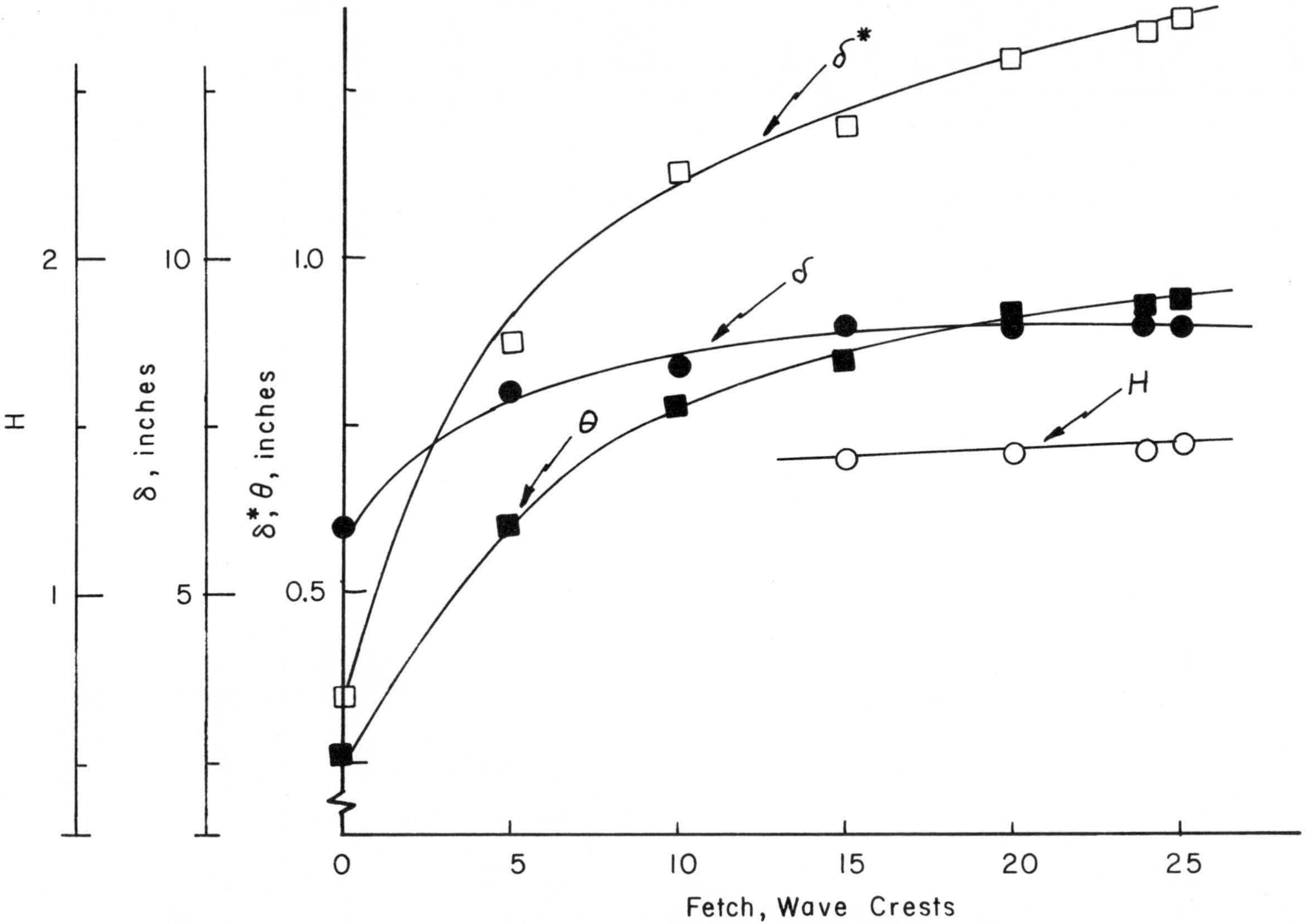

Fig. 25. Boundary layer parameter variation, Wave A.

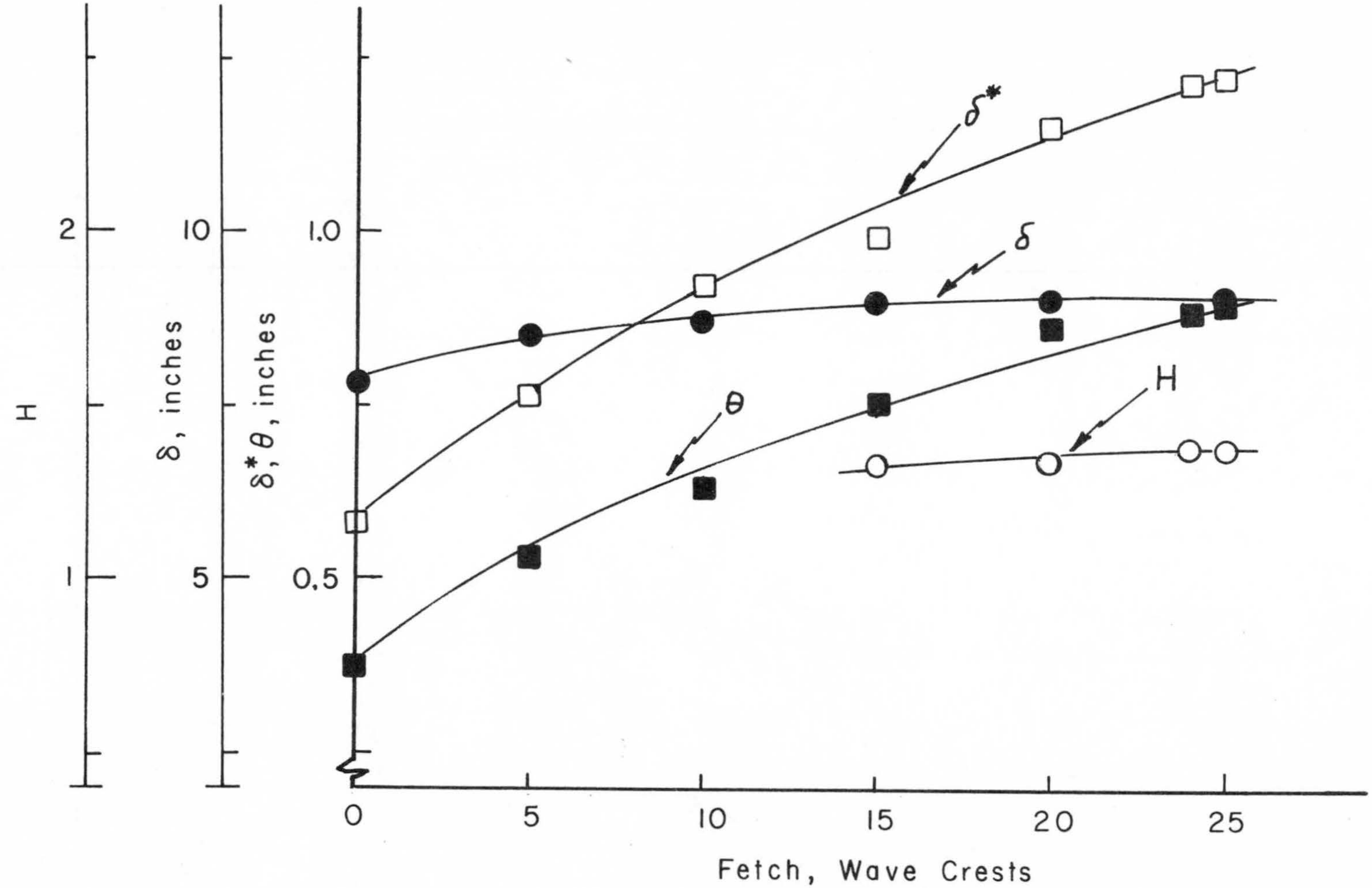

Fig. 26. Boundary layer parameter variation, Wave B.

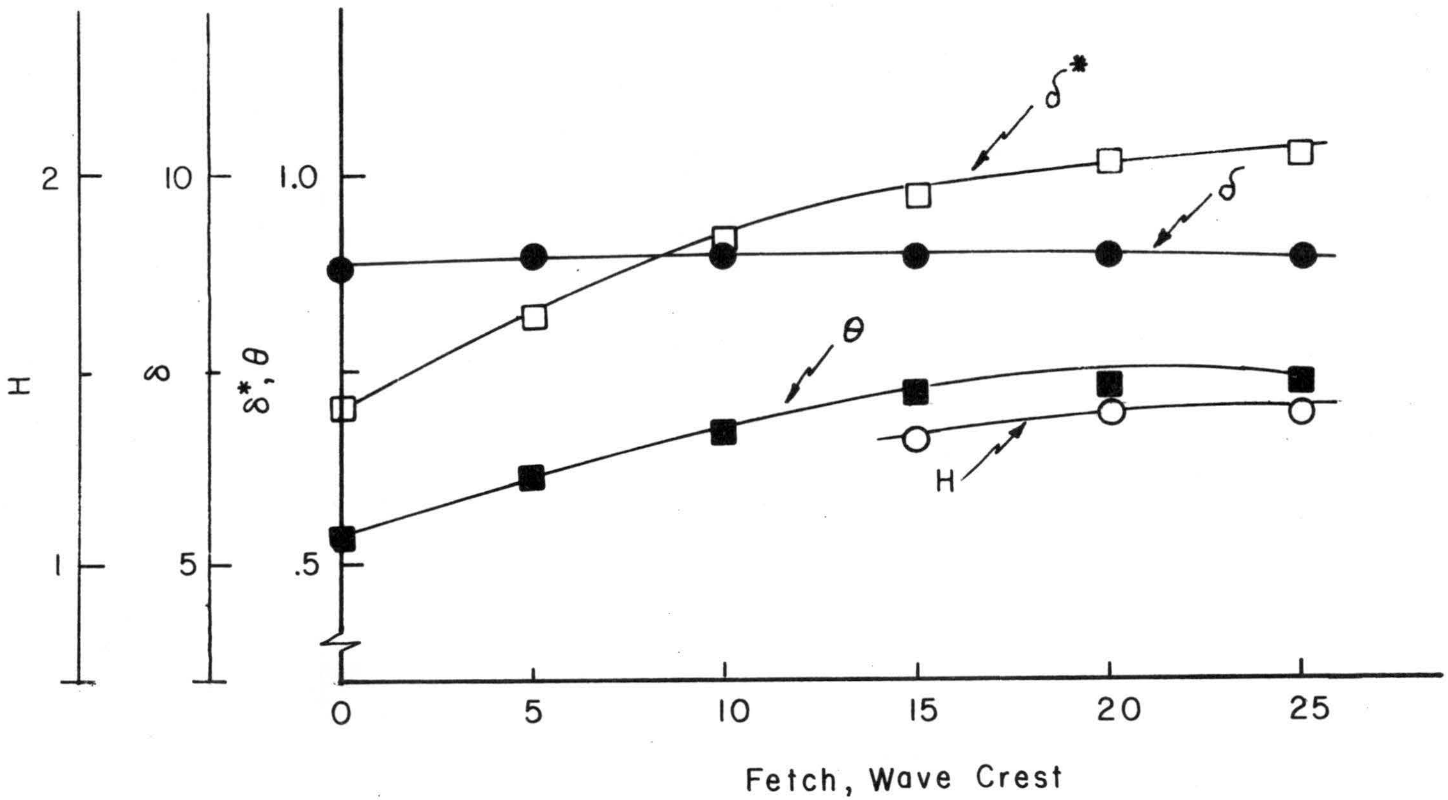

Fig. 27. Boundary layer parameter variation, Wave C.

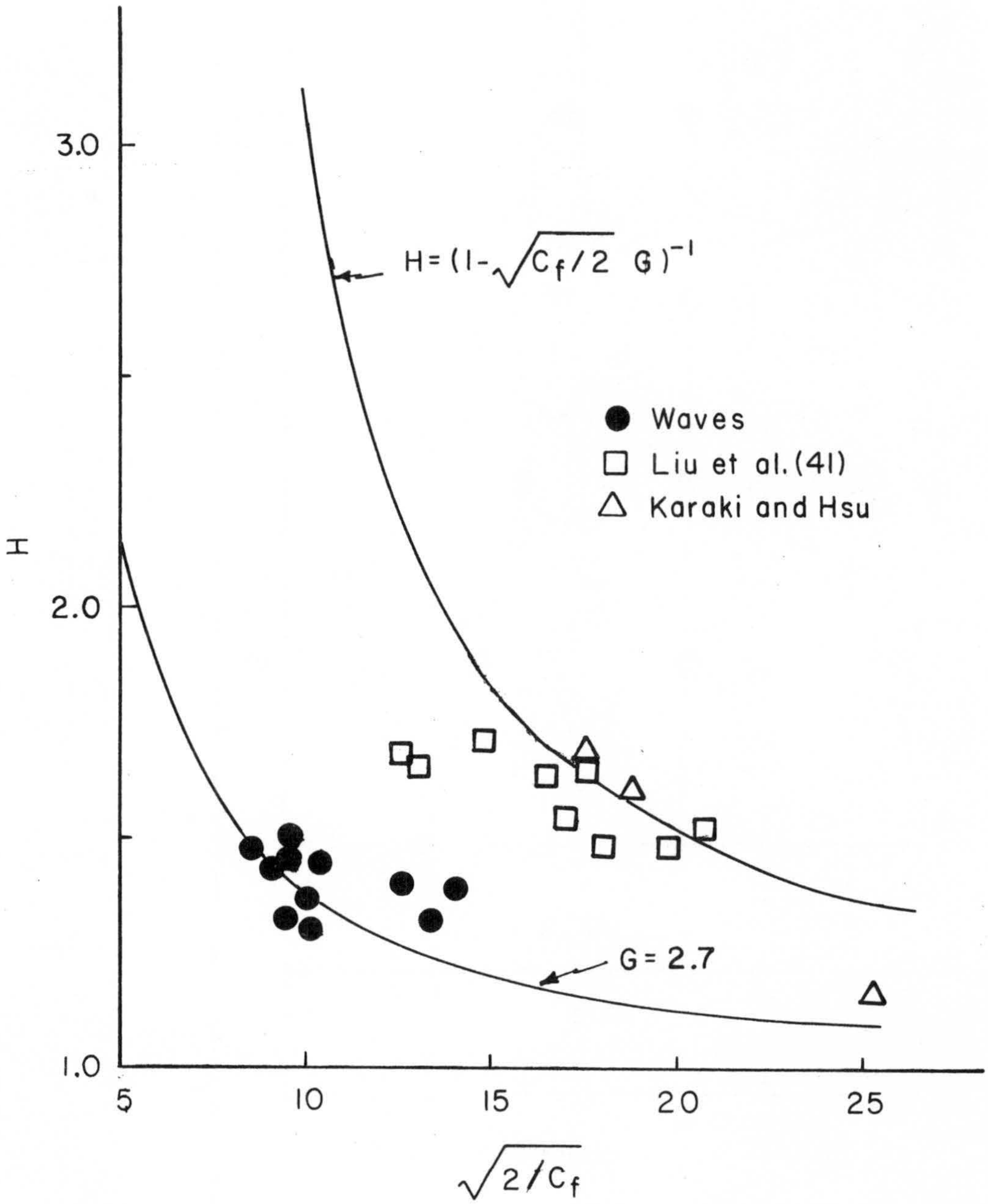

Fig. 28. Shape factor variation.

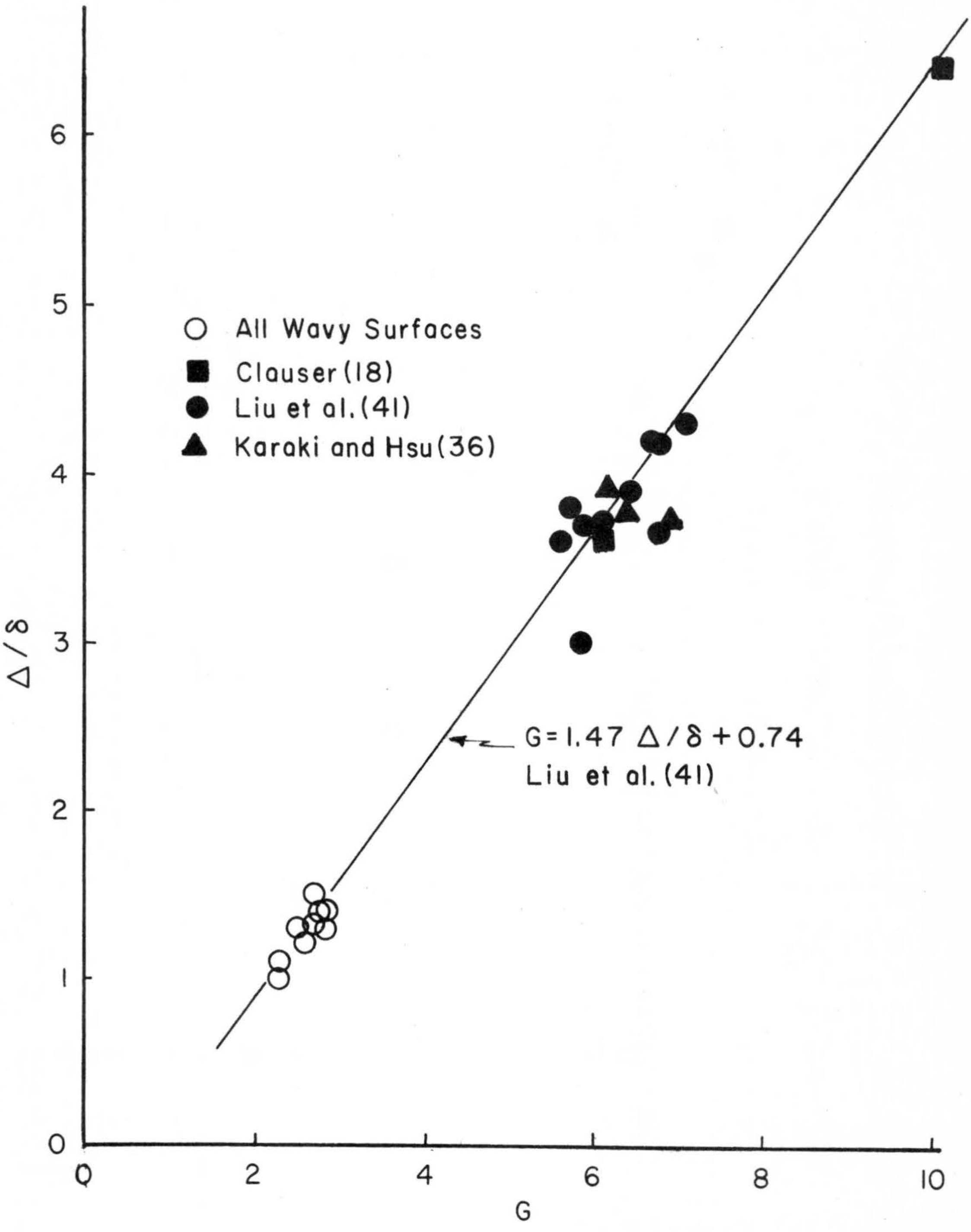

Fig. 29. Equilibrium boundary layers.

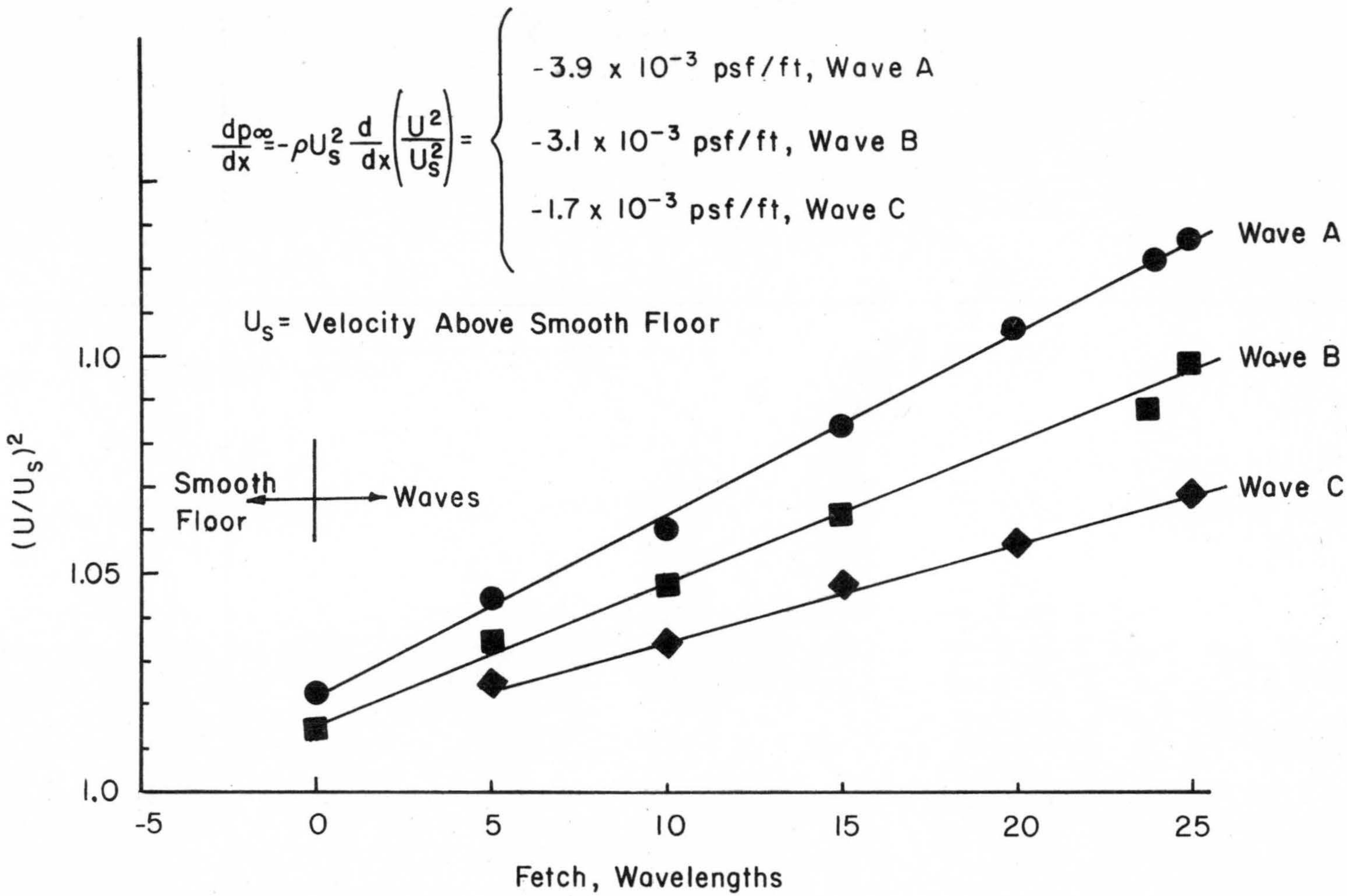

Fig. 30. Pressure gradients above wavy surface.

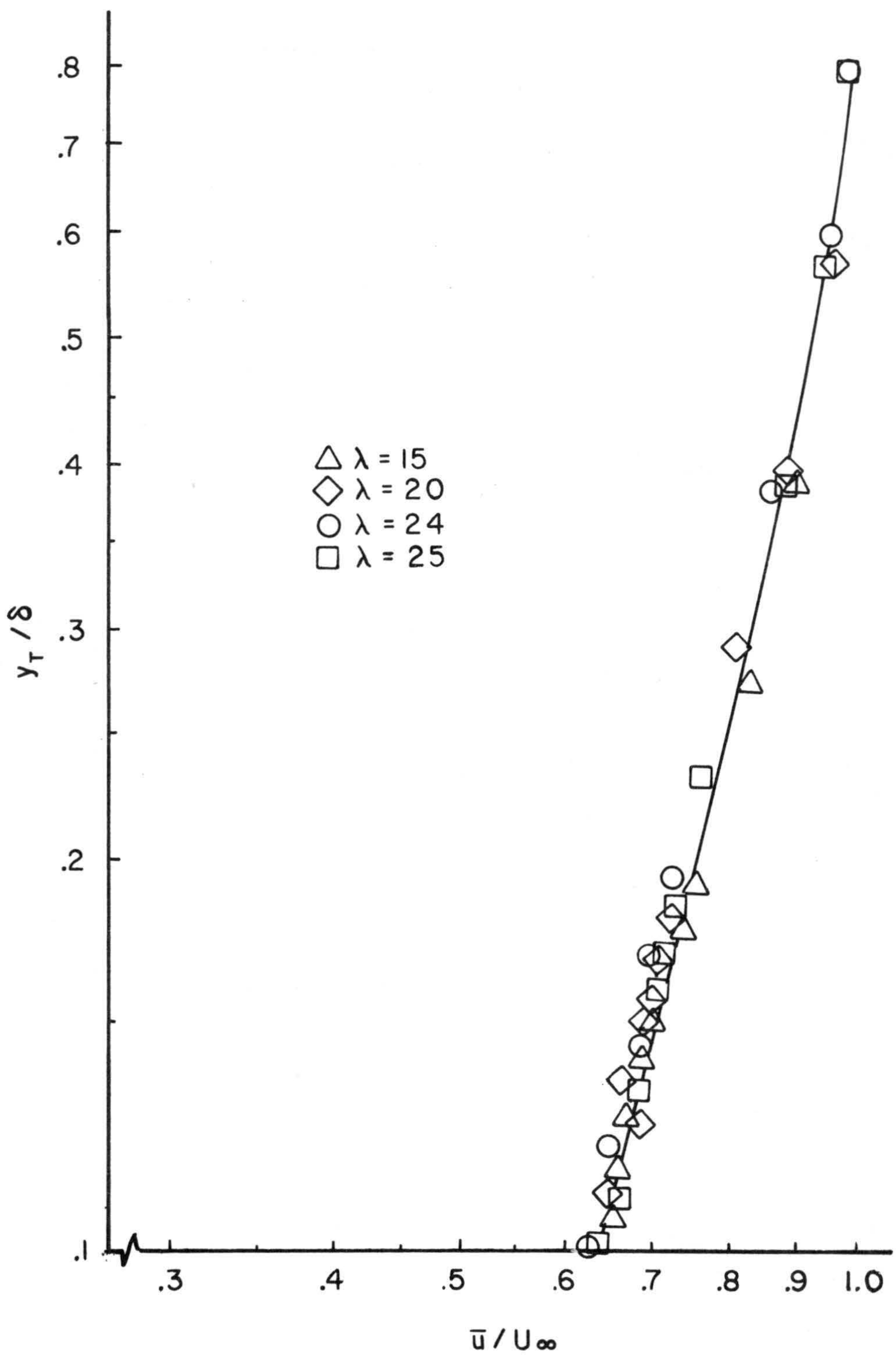

Fig. 31. Power law velocity profiles, Wave A.

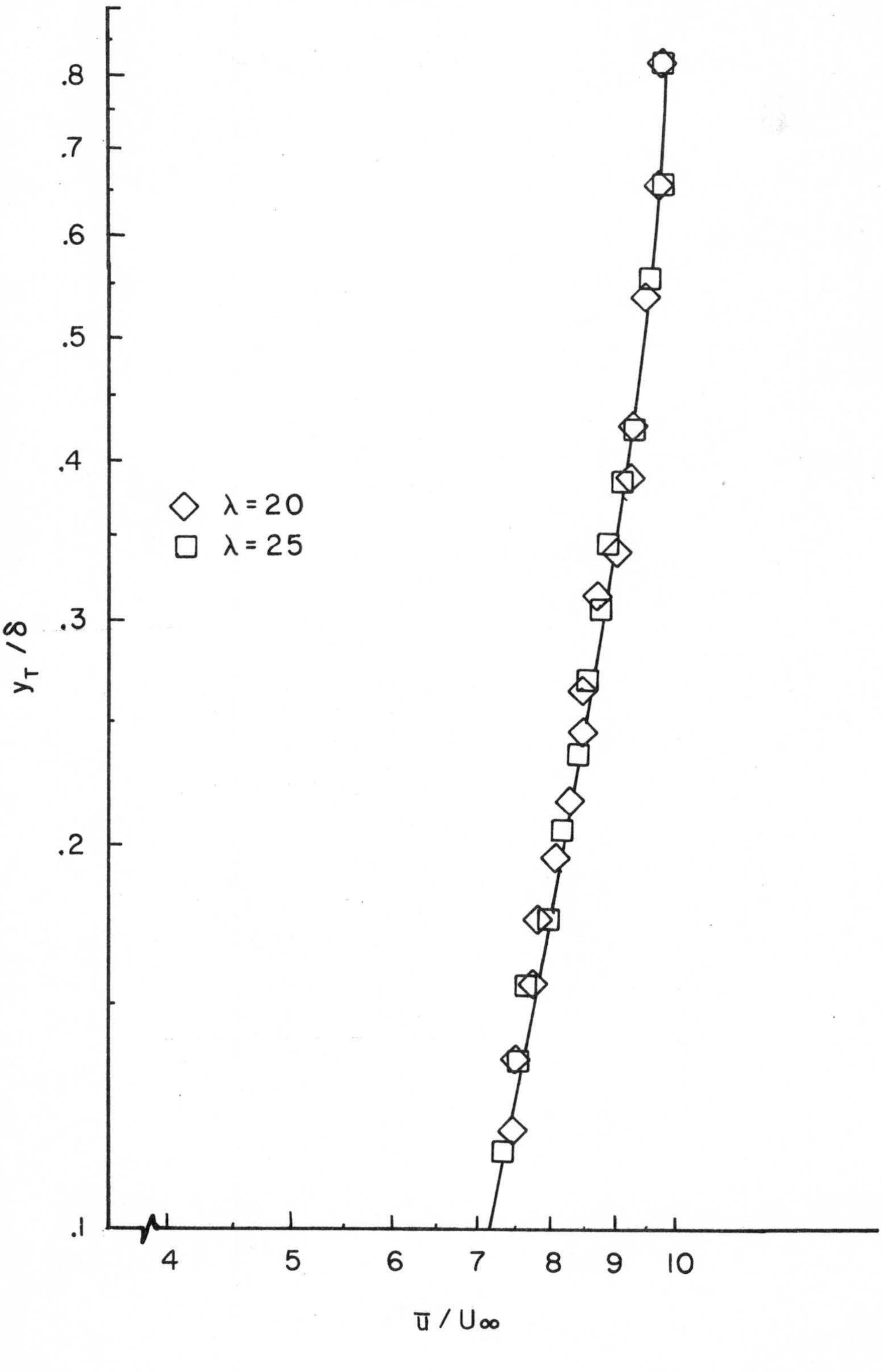

Fig. 32. Power law velocity profiles, Wave C.

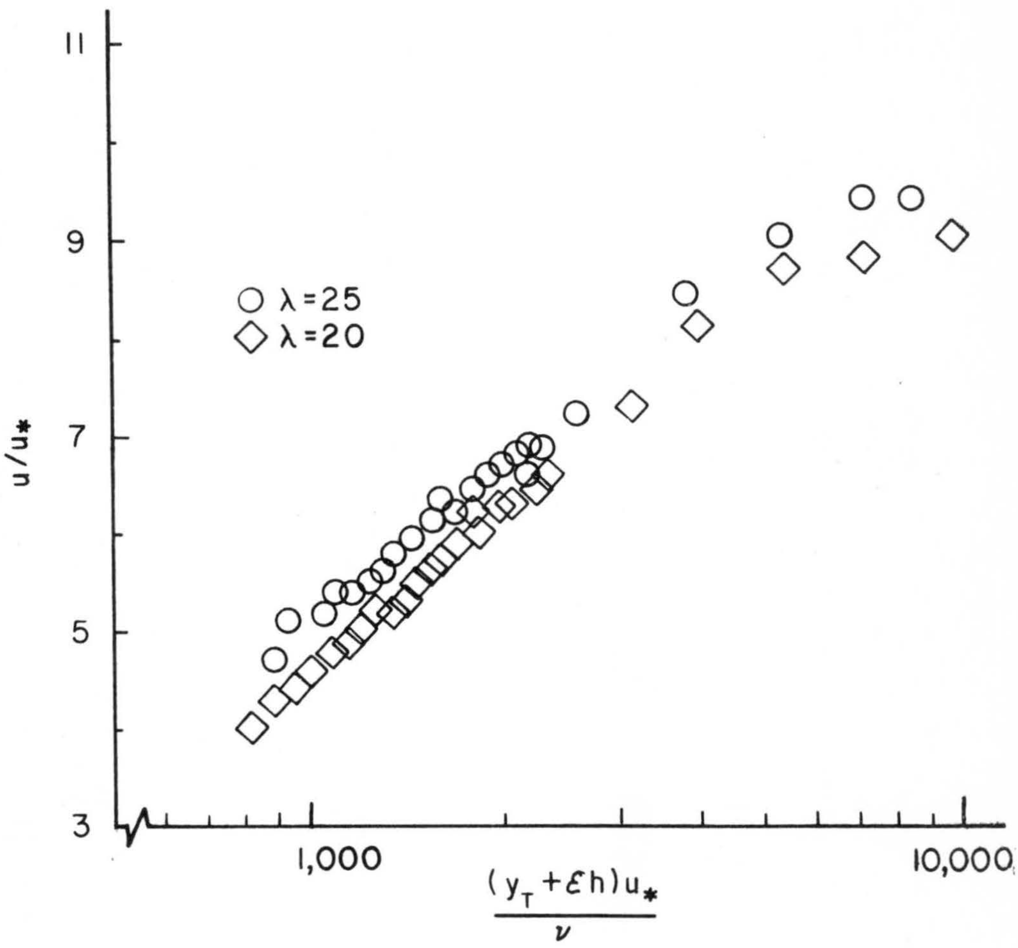

Fig. 33. Logarithmic velocity profiles, Wave A.

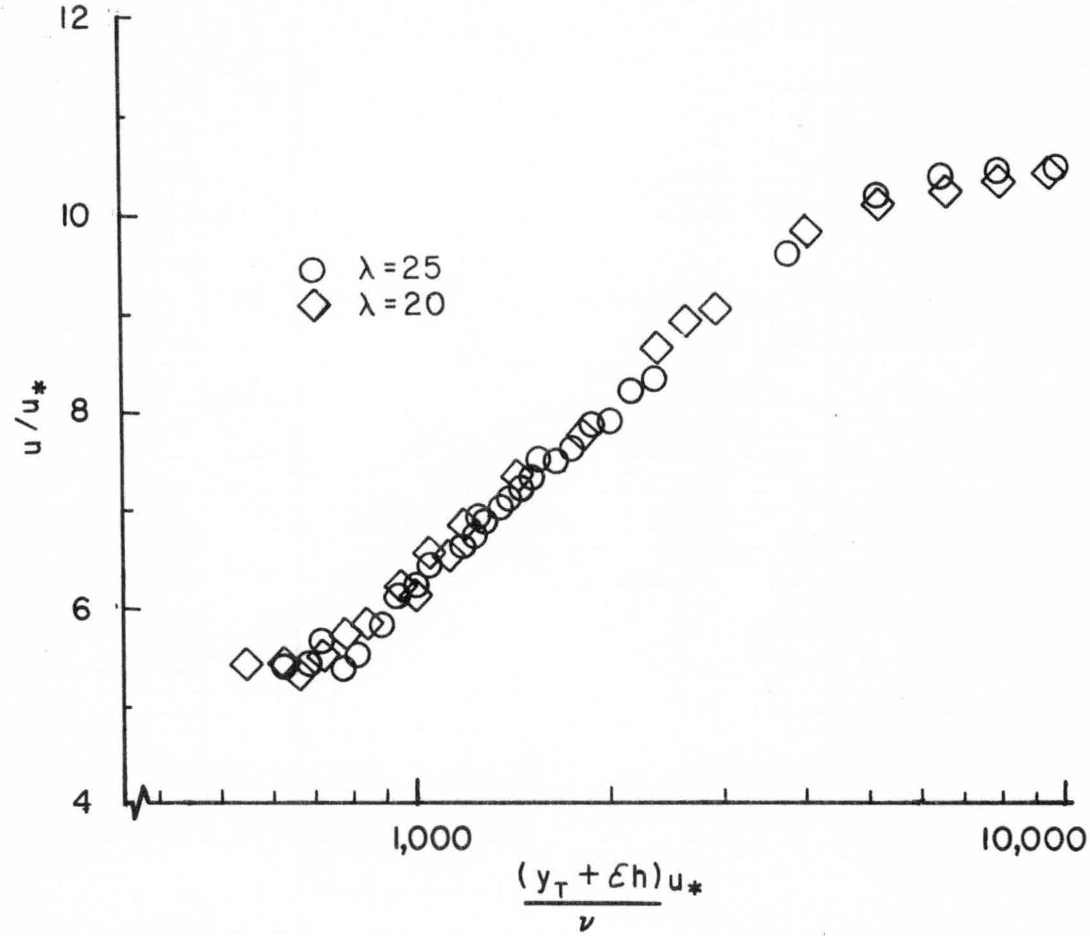

Fig. 34. Logarithmic velocity profiles, Wave B.

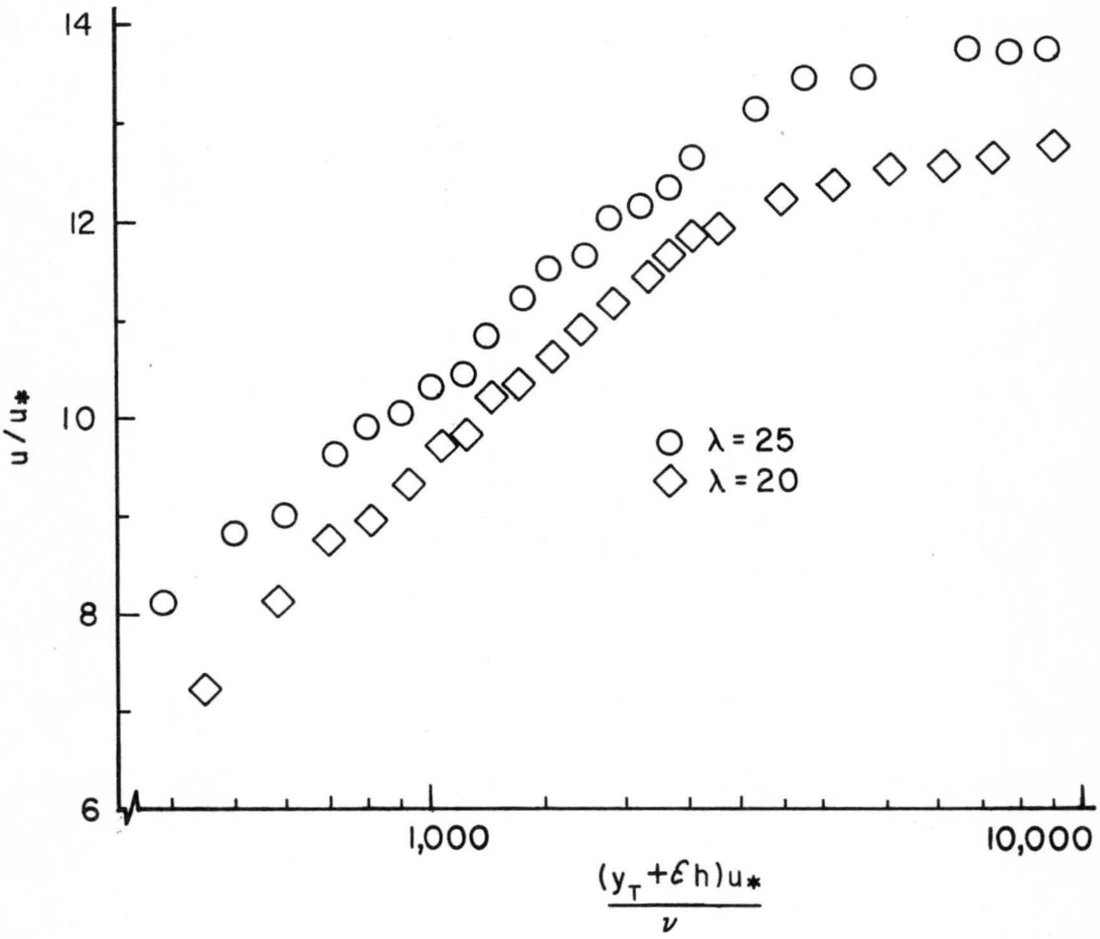

Fig. 35. Logarithmic velocity profiles, Wave C.

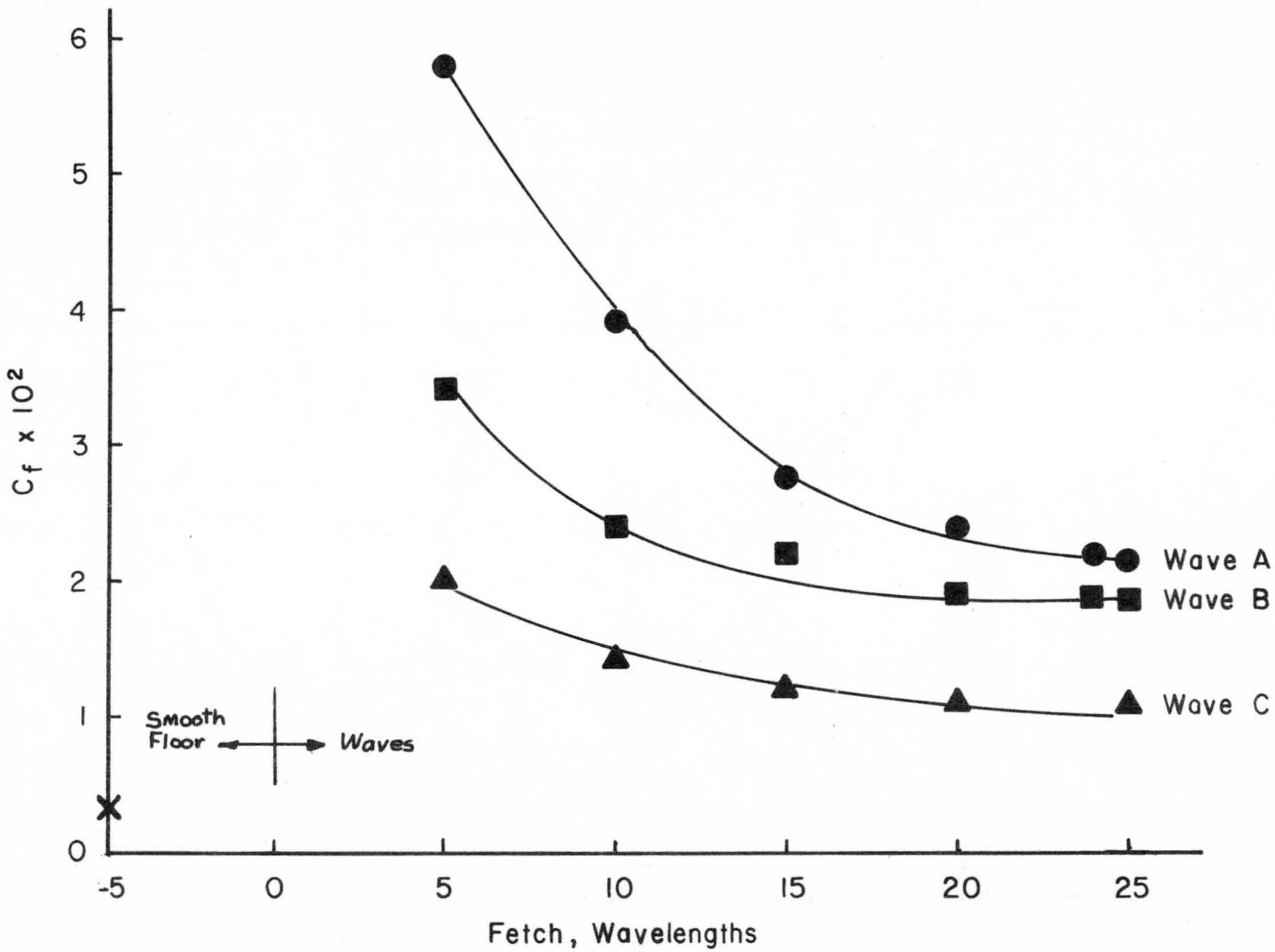

Fig. 36. Longitudinal variation of skin friction.

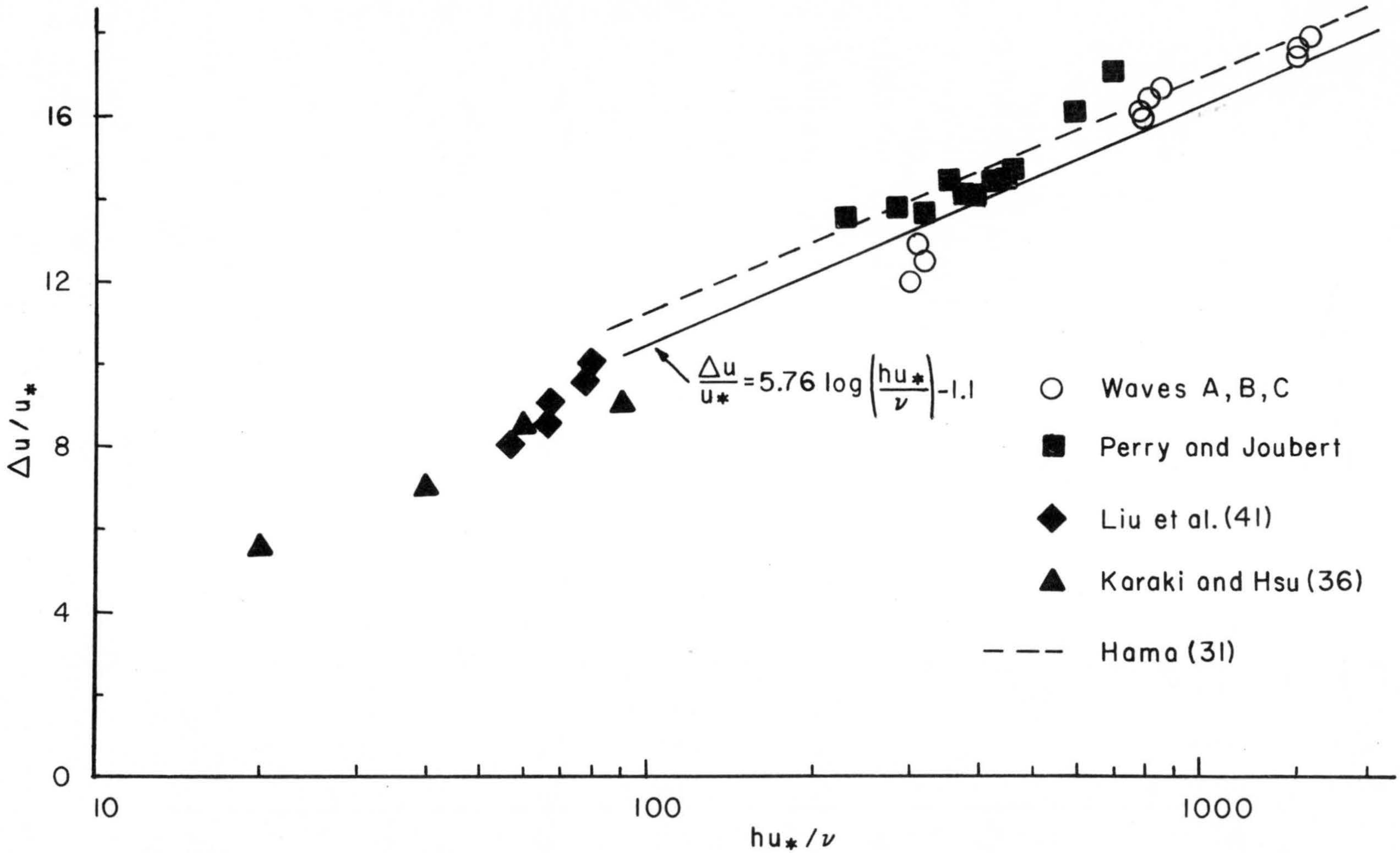

Fig. 37. Roughness function as a function of hu_*/ν.

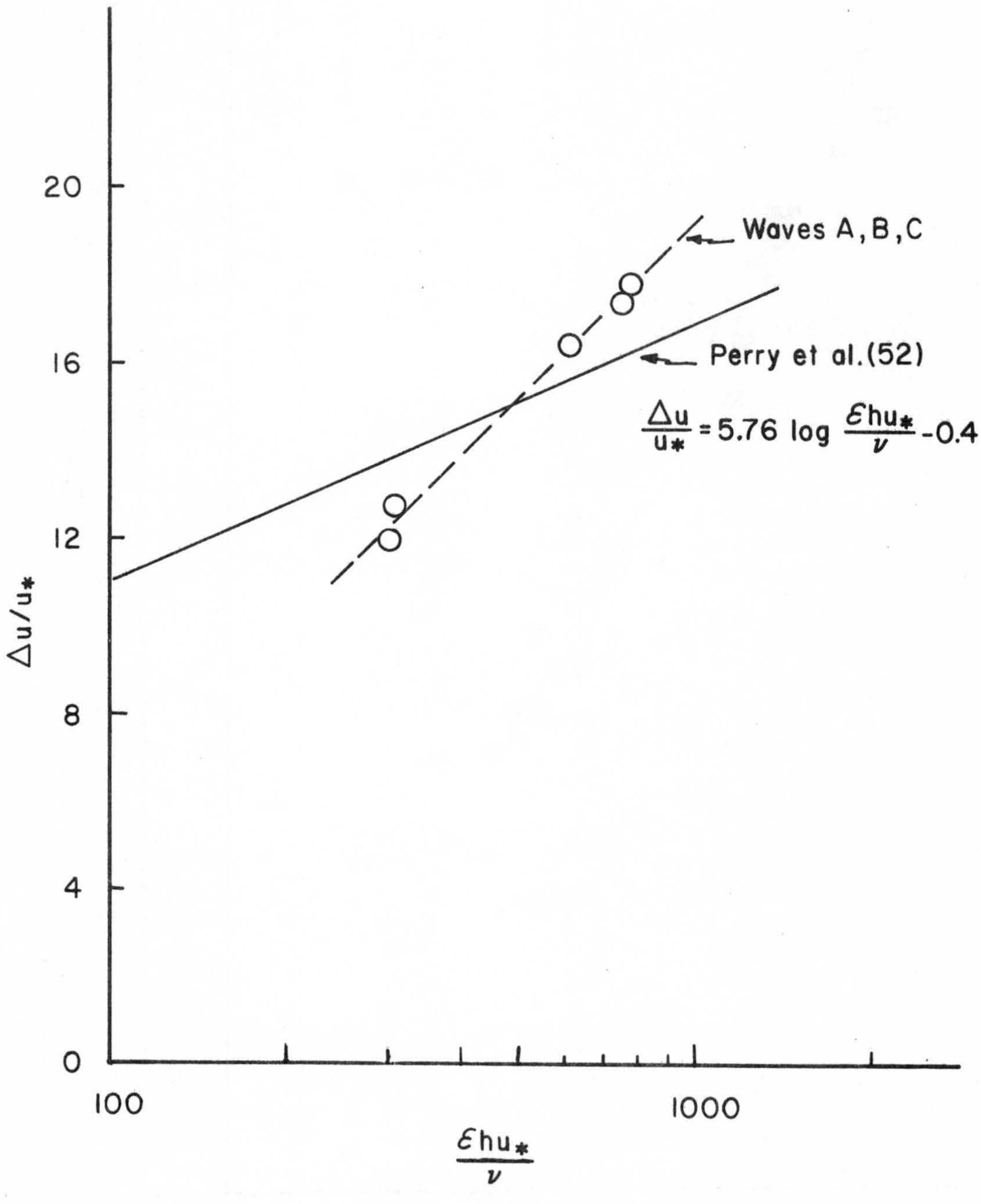

Fig. 38. Roughness function as a function of origin shift.

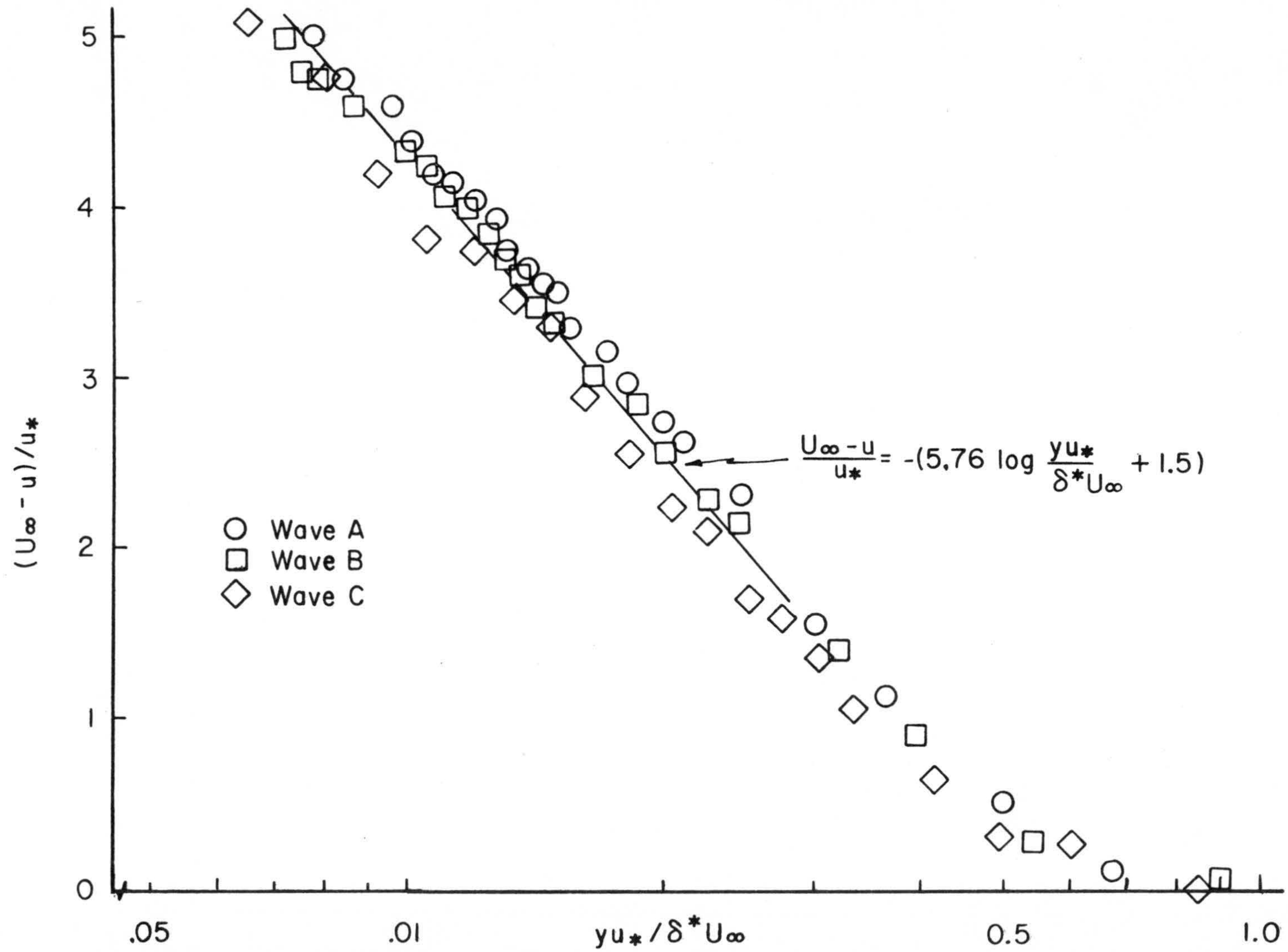

Fig. 39. Velocity defect profile (far downstream).

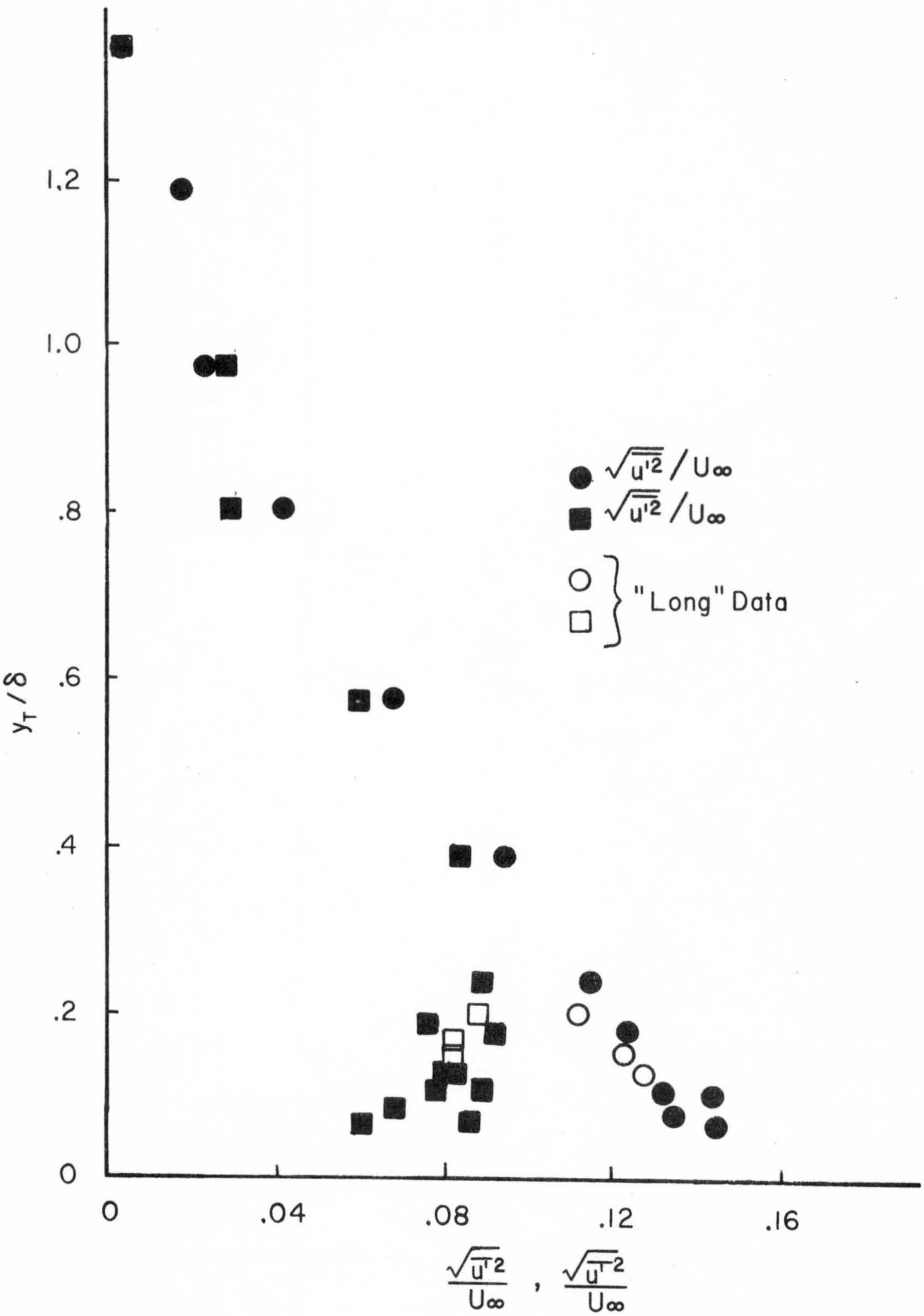

Fig. 40. Turbulence intensities, Wave A.

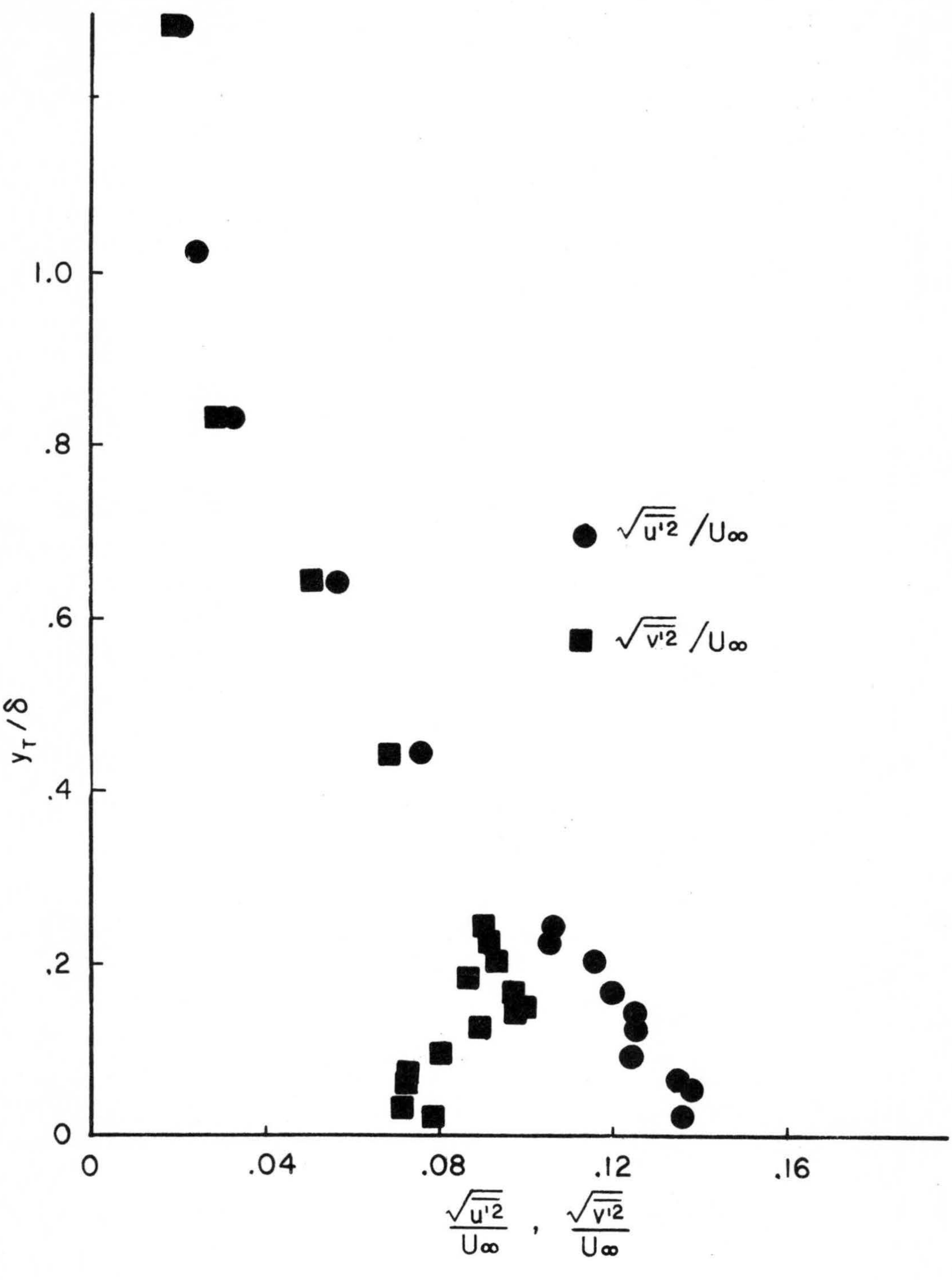

Fig. 41. Turbulence intensities, Wave B.

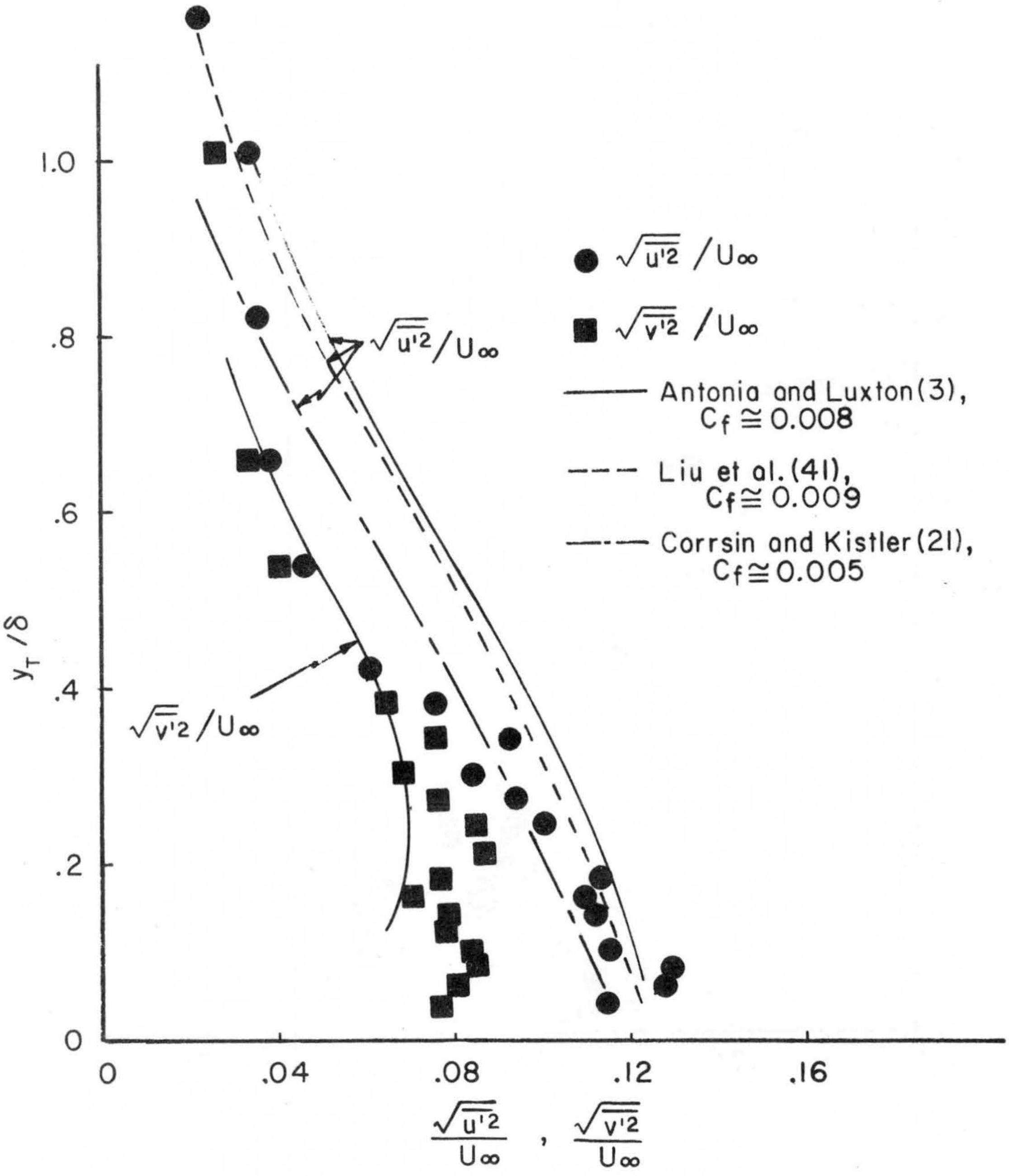

Fig. 42. Turbulence intensities, Wave C.

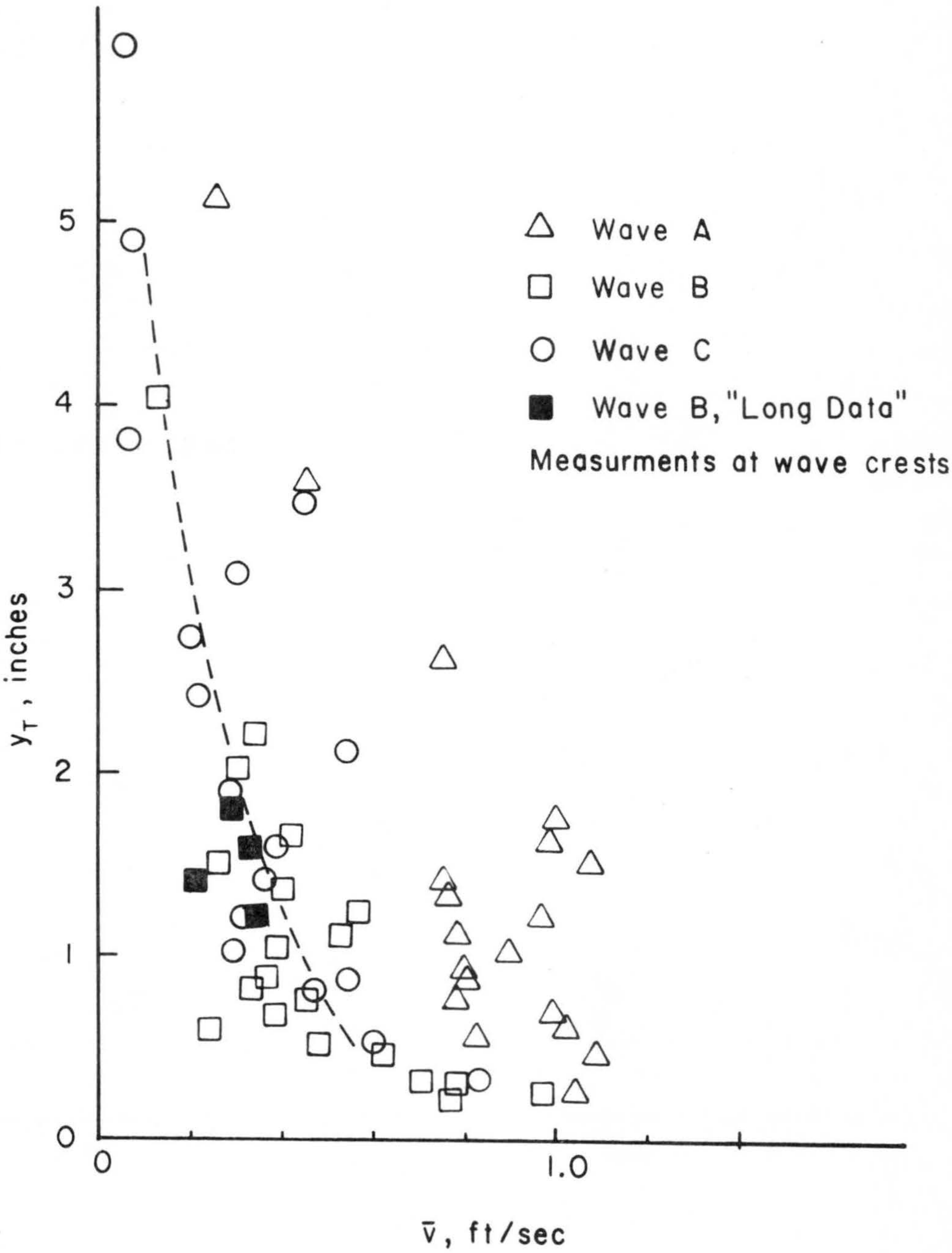

Fig. 43. Vertical velocity profiles.

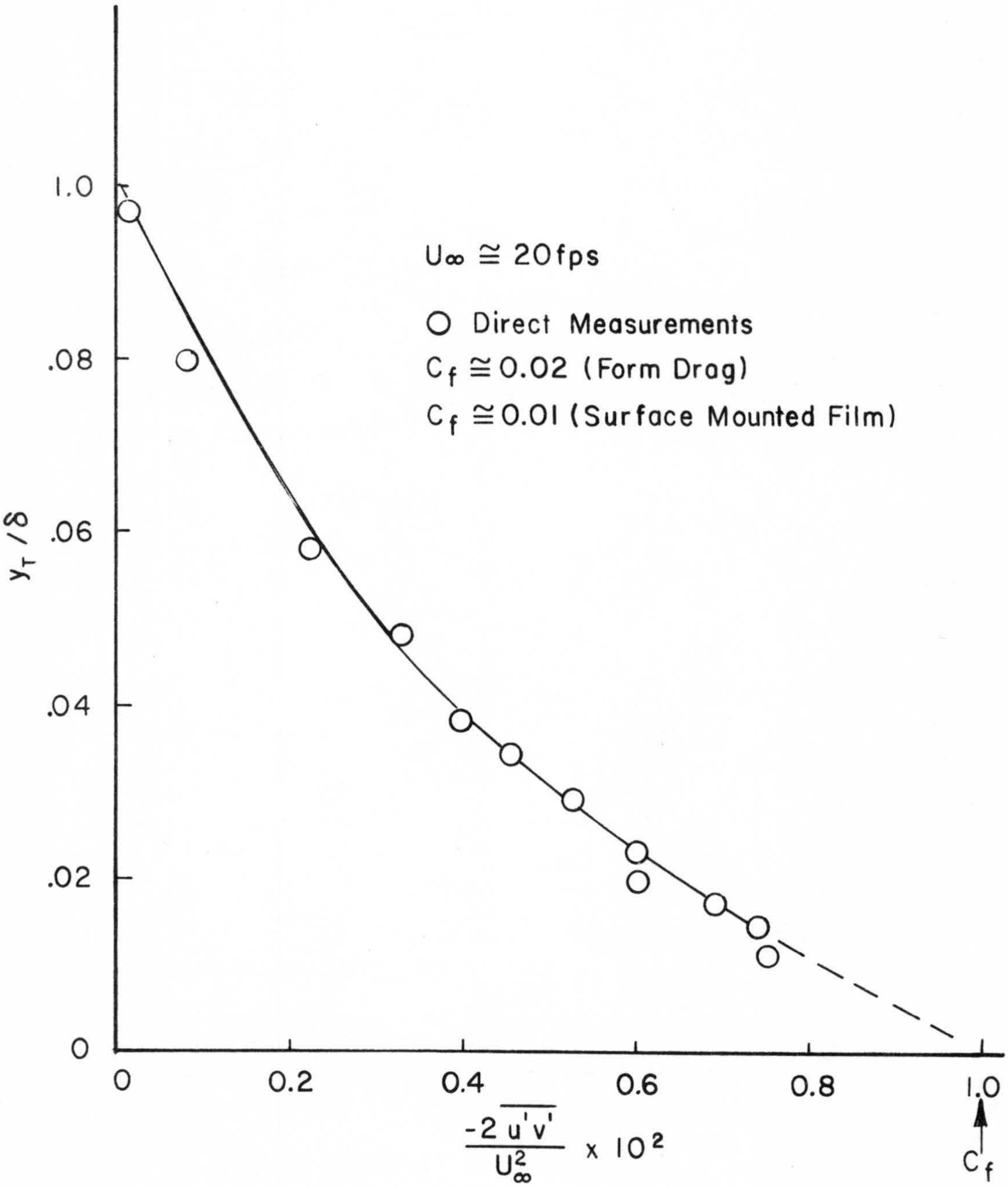

Fig. 44. Turbulent shear stress profile, Wave A.

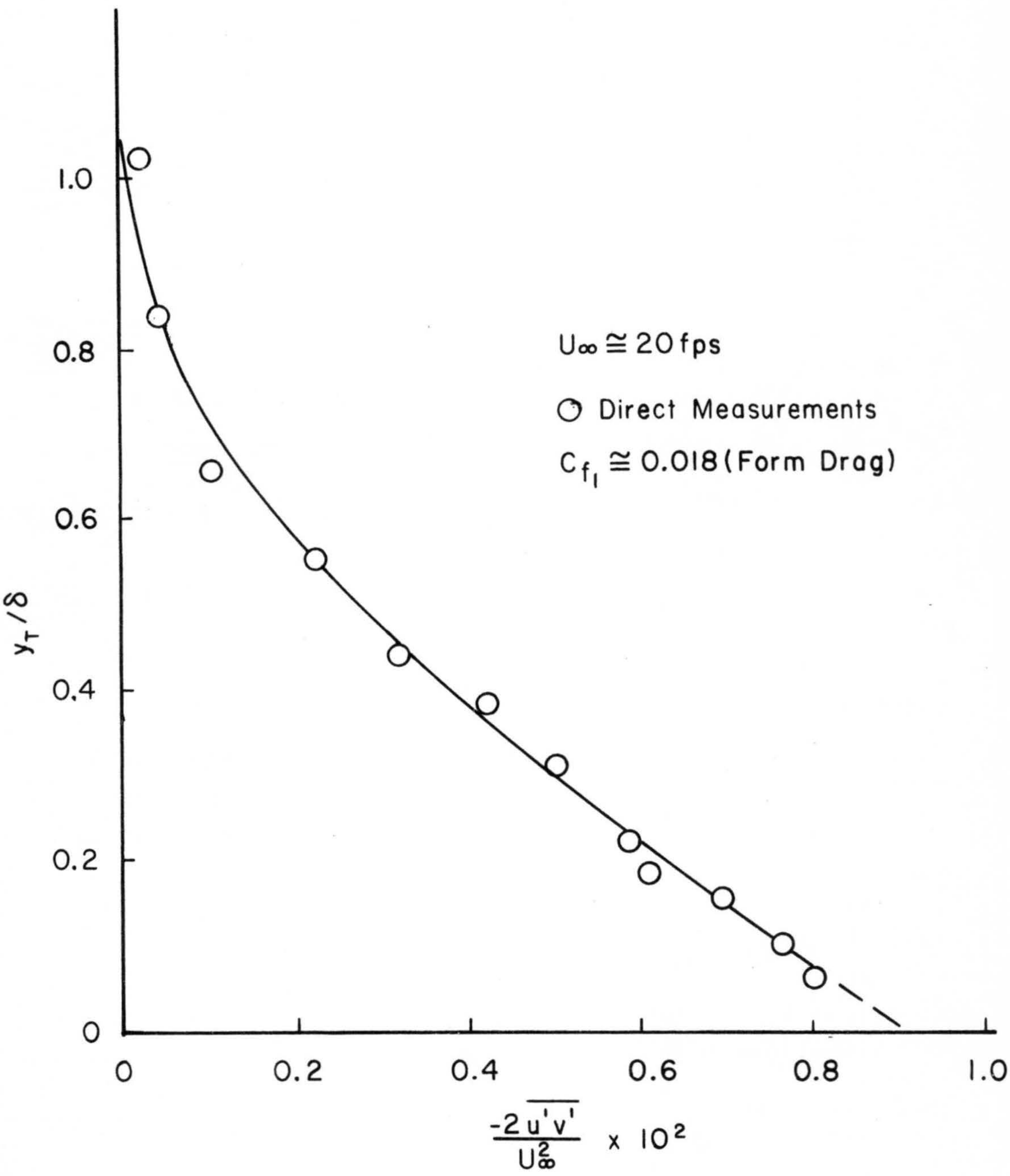

Fig. 45. Turbulent shear stress profile, Wave B.

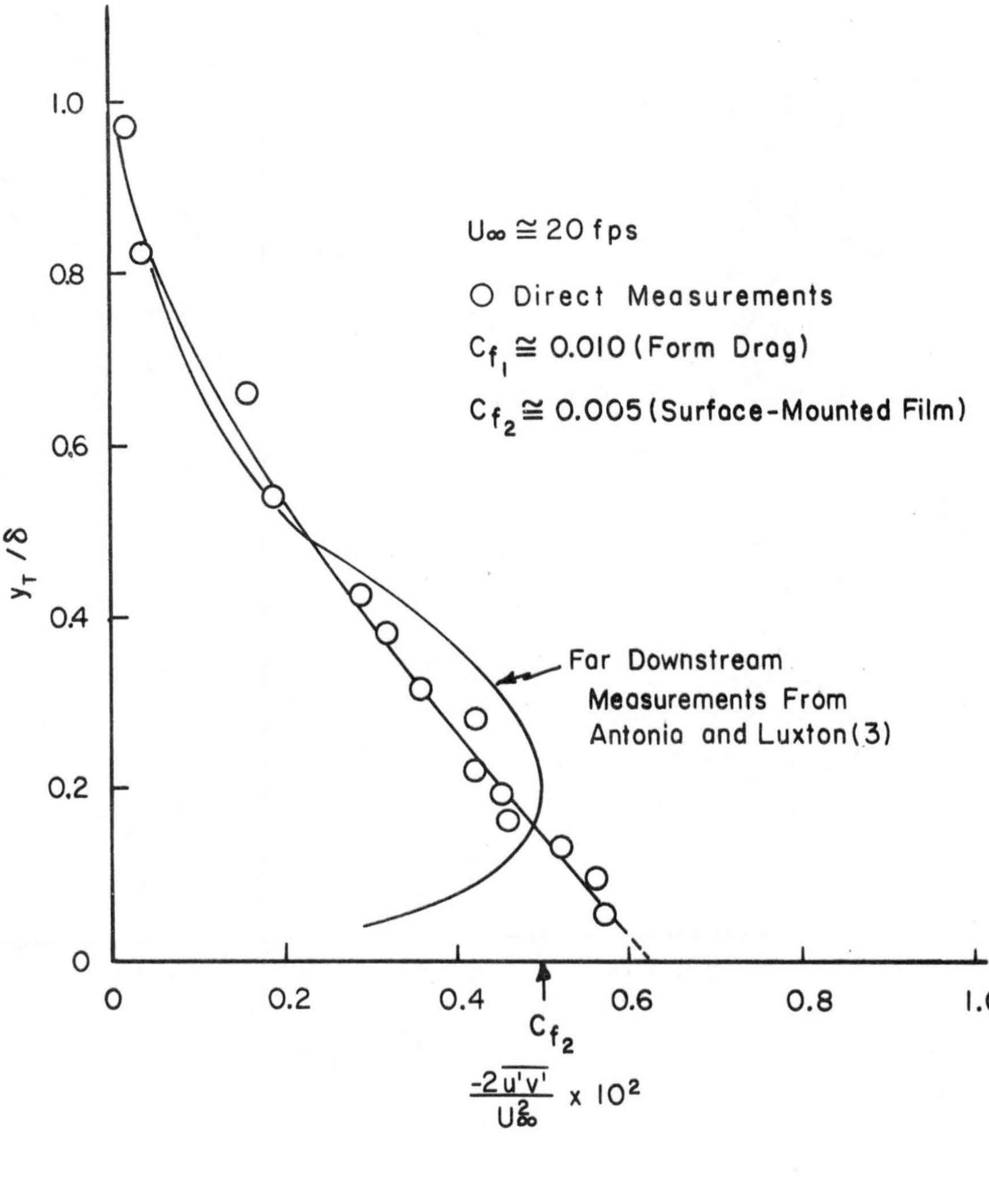

Fig. 46. Turbulent shear stress profile, Wave C.

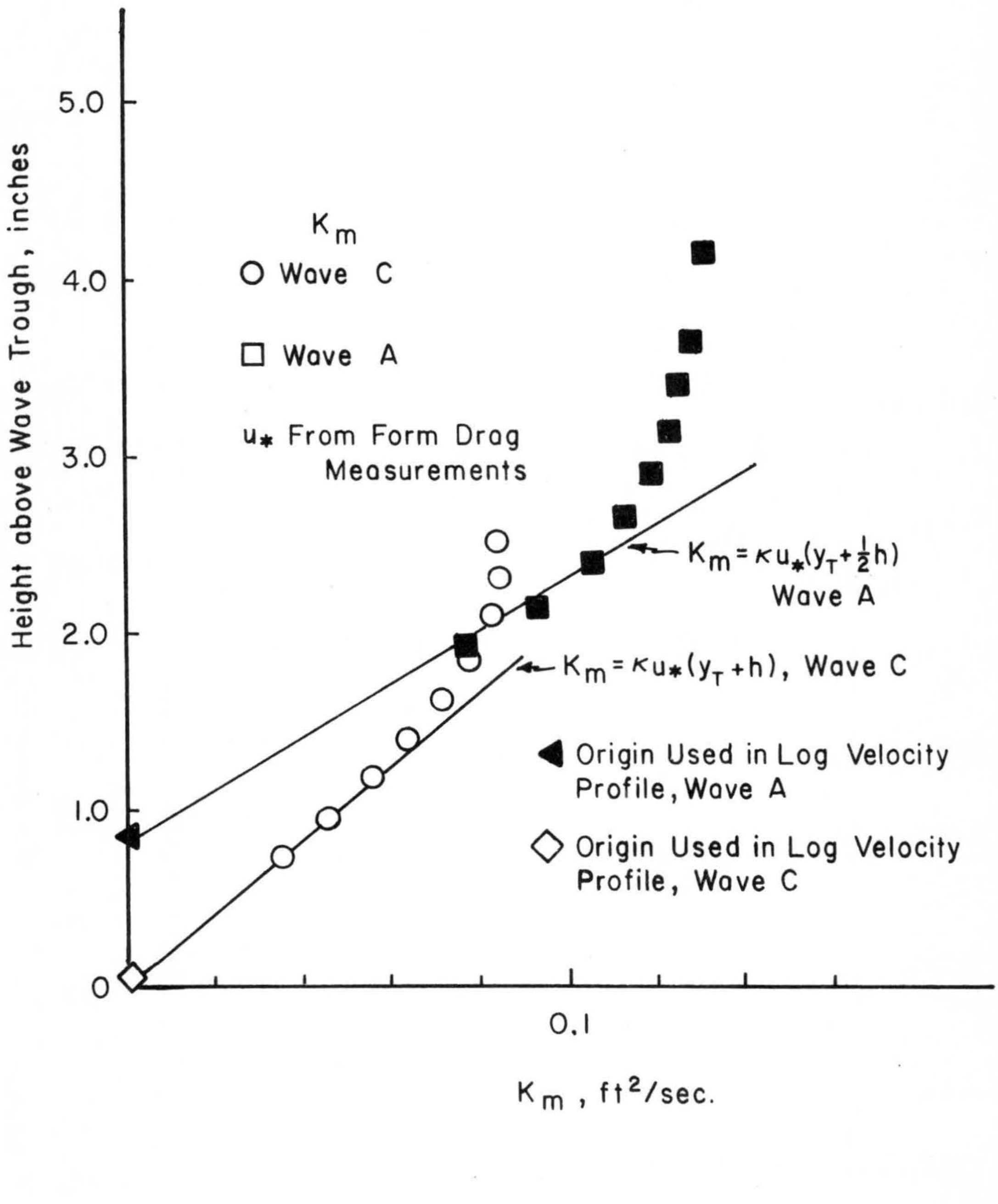

Fig. 47. Eddy viscosity variation for Waves A & C.

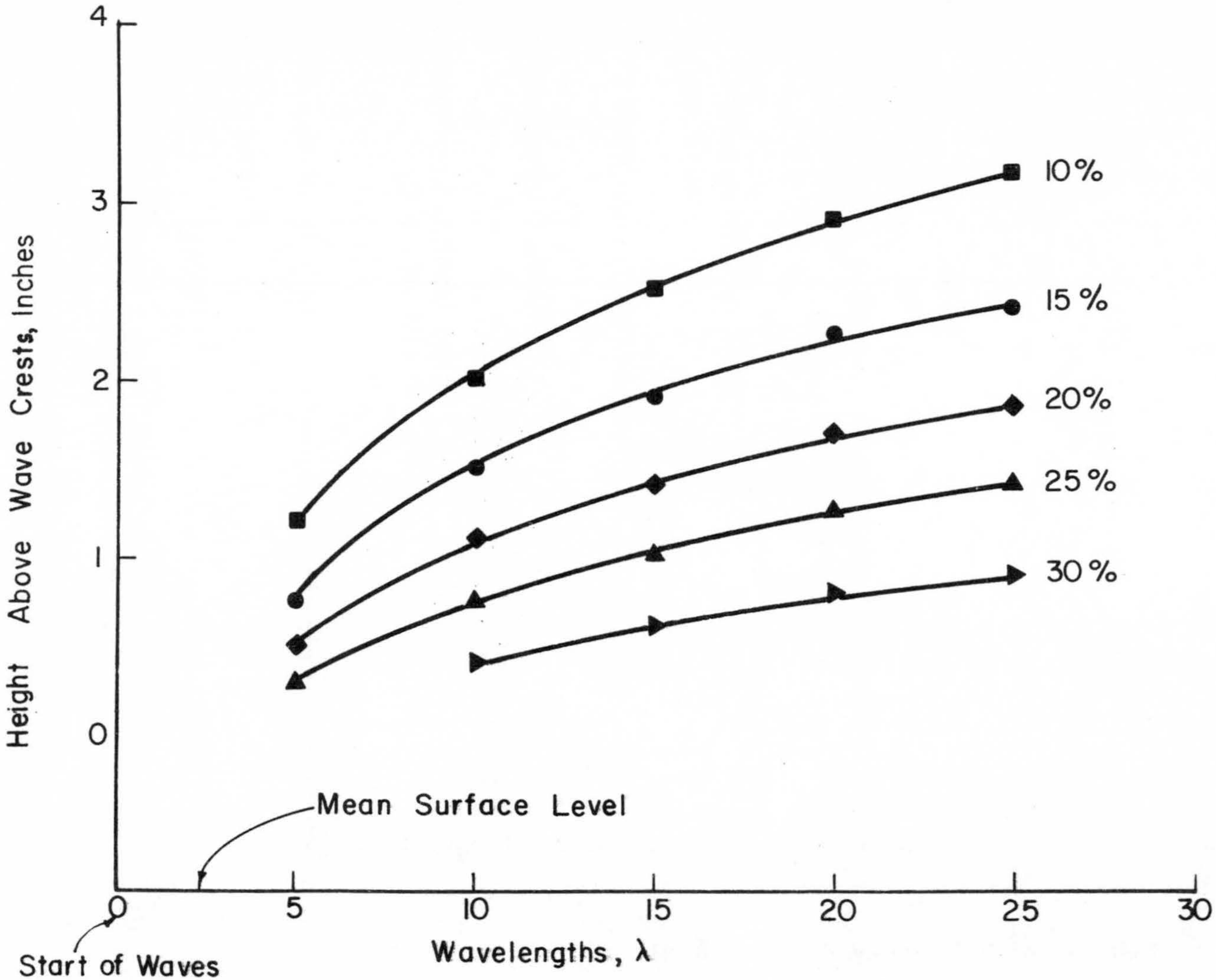

Fig. 48. Wind reduction factors, Wave A.

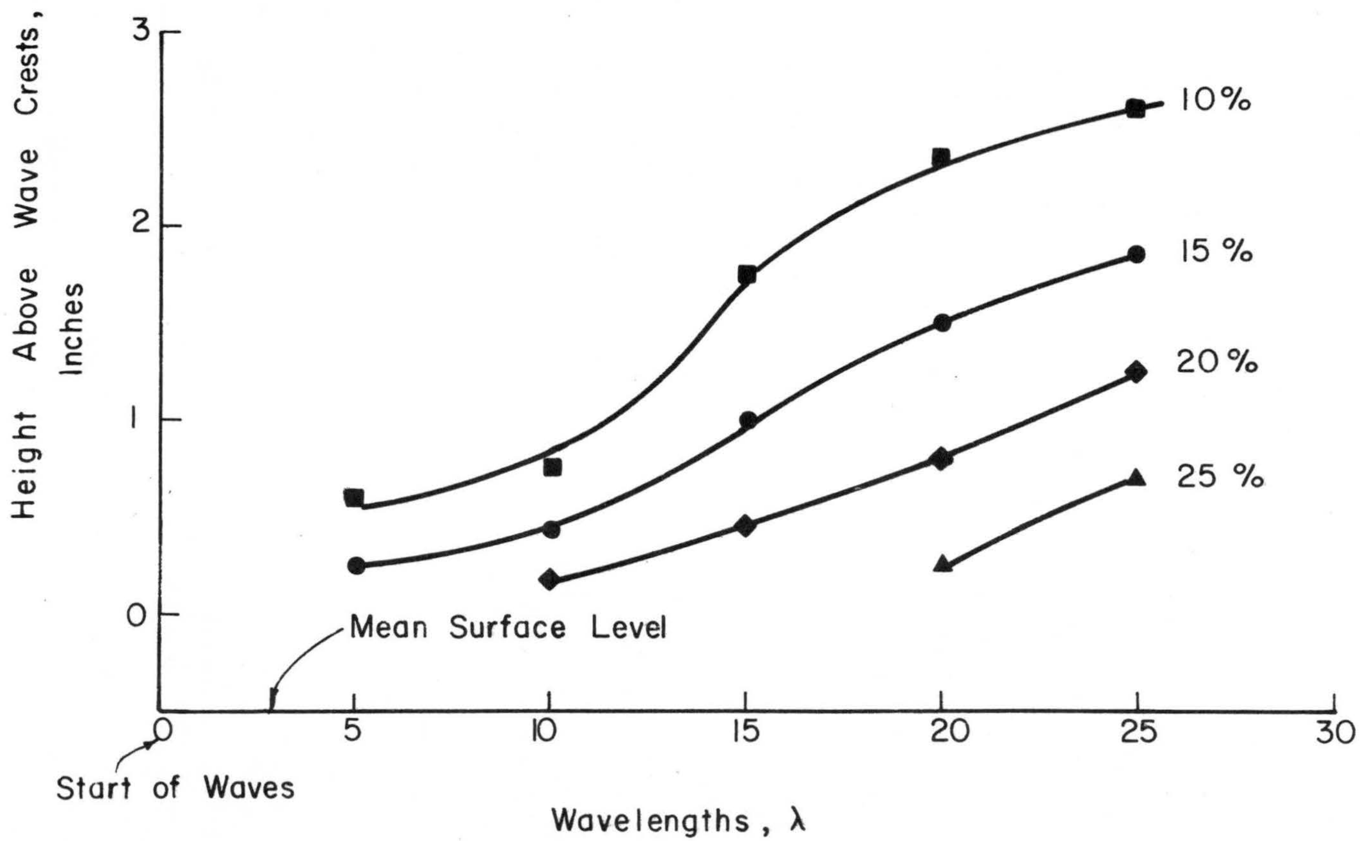

Fig. 49. Wind reduction factors, Wave B.

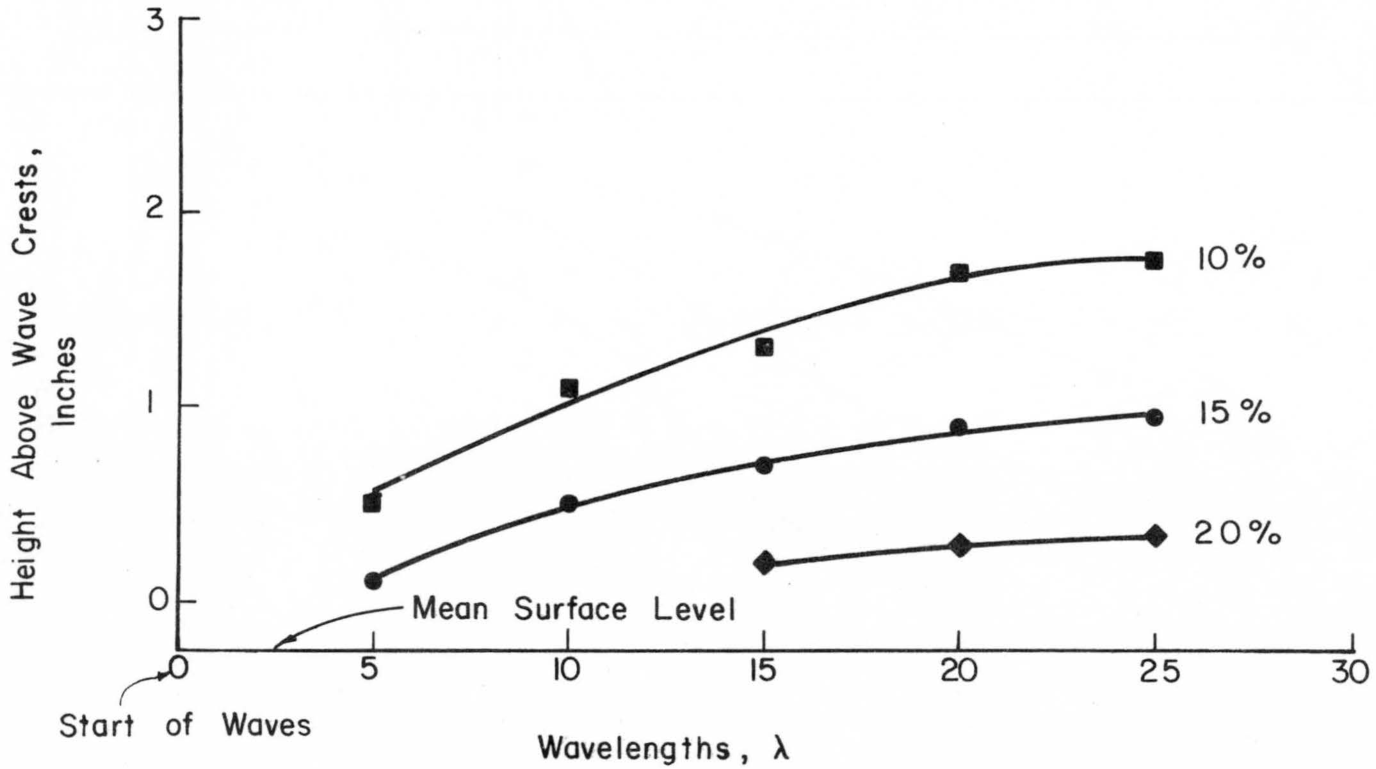

Fig. 50. Wind reduction factors, Wave C.

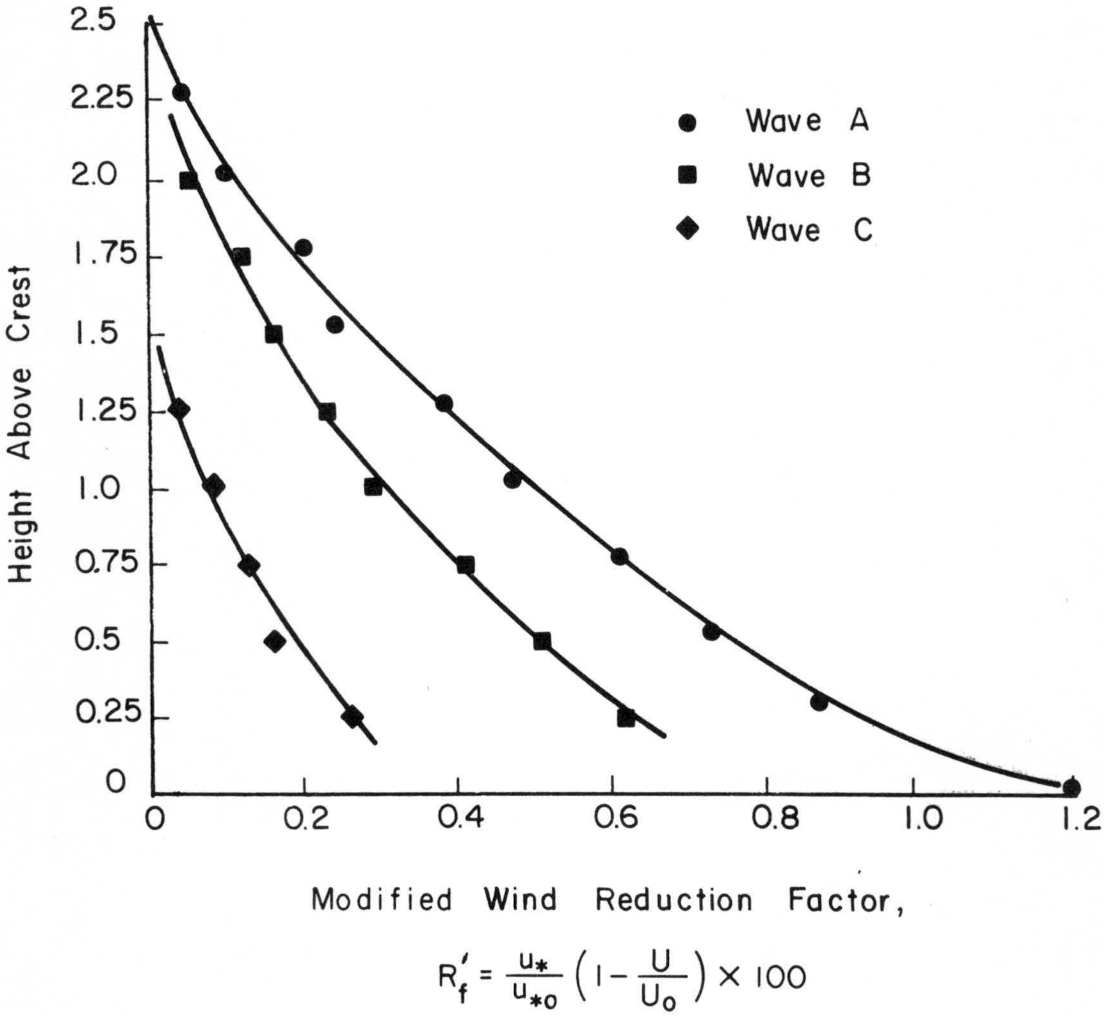

Fig. 51. Modified wind-reduction factors.

Security Classification

DOCUMENT CONTROL DATA - R & D	
(Security classification of title, body of abstract and indexing annotation must be entered when the overall report is classified)	
1. ORIGINATING ACTIVITY (Corporate author) Fluid Dynamics & Diffusion Laboratory College of Engineering, Colorado State University Fort Collins, Colorado 80521	2a. REPORT SECURITY CLASSIFICATION Unclassified 2b. GROUP
3. REPORT TITLE Turbulent Flow Over a Wavy Boundary	
4. DESCRIPTIVE NOTES (Type of report and inclusive dates) Technical Report	
5. AUTHOR(S) (First name, middle initial, last name) BEEBE, P. S. and CERMAK, J. E.	

6. REPORT DATE	7a. TOTAL NO. OF PAGES	7b. NO. OF REFS
May 1972	119	68

8a. CONTRACT OR GRANT NO. 14-01-0001	9a. ORIGINATOR'S REPORT NUMBER(S) CER71-72PSB-JEC44
b. PROJECT NO. N00014-68-A-0493-0001	
c.	9b. OTHER REPORT NO(S) (Any other numbers that may be assigned this report) Themis Technical Report No. 16
d.	
10. DISTRIBUTION STATEMENT Distribution of this report is unlimited.	
11. SUPPLEMENTARY NOTES	12. SPONSORING MILITARY ACTIVITY U.S. Department of Defense Office of Naval Research

13. ABSTRACT

An experimental study was made of turbulent flow over a wavy surface. Sinusoidal waves of three sizes were used to explore the variations of flow with wave size. Measurements of mean and turbulent velocities were taken with a two-wire method. Local heat transfer rates and pressures on the wavy surface were also measured.

An equilibrium turbulent boundary layer, which conforms to Rotta's and Clauser's self-preservation requirements, develops in the region far downstream from the first wave. In the lower portion of this layer, the mean velocity is represented by the logarithmic velocity profile when the form-drag measurements of skin friction are used to determine the shift-in-origin. The roughness function is related to the wave height since the wavy surface is shown to be a "k" type surface. The velocity defect profile in the logarithmic form extends to higher values of $yu_*/\delta^* U_\infty$ than those for smooth wall flows. Eddy viscosity results support the assumed logarithmic velocity variation in the lower part of the boundary layer. Measurements of shear stress by either the two-wire or the heated-film method disagree with the form drag measurements of skin friction.

The wavy surface is an extended surface windbreak since it reduces the overall wind speed above the surface and creates vortices between the waves. However, surface shear stresses are increased, and the erosion rate of field waves is a function of wave height.

DD FORM 1 NOV 65 1473

unclassified
Security Classification

14 KEY WORDS	LINK A		LINK B		LINK C	
	ROLE	WT	ROLE	WT	ROLE	WT
Turbulent Boundary Layer Rigid Wavy Boundary Shear Stress Measurement Wind Breaks						

April 1971

DISTRIBUTION LIST FOR UNCLASSIFIED
TECHNICAL REPORTS ISSUED UNDER
CONTRACT N00014-68-A 0493-0001 TASK 000-414

Defense Documentation Center
Cameron Station
Alexandria, Virginia 22314 (12)

Technical Library
Naval Ship Research and Development Laboratory
Annapolis, Maryland 21402

Professor Bruce Johnson
Engineering Department
Naval Academy
Annapolis, Maryland 21402

Library
Naval Academy
Annapolis, Maryland 21402

Professor W.R. Debler
Department of Engineering Mechanics
University of Michigan
Ann Arbor, Michigan 48108

Professor W.P. Graebel
Department of Engineering Mechanics
University of Michigan
College of Engineering
Ann Arbor, Michigan 48108

Professor Finn C. Michelsen
Naval Architecture and Marine Engineering
445 West Engineering Building
University of Michigan
Ann Arbor, Michigan 48108

Dr. Francis Ogilvie
Department of Naval Architecture and Marine Engineering
University of Michigan
Ann Arbor, Michigan 48108

Professor W.W. Willmarth
Department of Aerospace Engineering
University of Michigan
Ann Arbor, Michigan 48108

Dr. S.A. Piacsek
Argonne National Laboratory
Applied Mathematics Division
9700 S. Cass Avenue
Argonne, Illinois 60439

AFOSR (REM)
1400 Wilson Boulevard
Arlington, Virginia 22204

Professor S. Corrsin
Mechanics Department
The Johns Hopkins University
Baltimore, Maryland 20910

Professor L.S.G. Kovasznay
The Johns Hopkins University
Baltimore, Maryland 20910

Professor O.M. Phillips
The Johns Hopkins University
Baltimore, Maryland 20910

Librarian
Department of Naval Architecture
University of California
Berkeley, California 94720

Professor Israel Cornet
Department of Mechanical Engineering
University of California
Berkeley, California 94720

Professor M. Holt
Division of Aeronautical Sciences
University of California
Berkeley, California 94720

Professor E.V. Laitone
Department of Mechanical Engineering
University of California
Berkeley, California 94720

Professor P. Lieber
Department of Mechanical Engineering
University of California
Institute of Engineering Research
Berkeley, California 94720

Professor J.R. Paulling
Department of Naval Architecture
University of California
Berkeley, California 94720

Professor J.V. Wehausen
Department of Naval Architecture
University of California
Berkeley, California 94720

Professor E.R. van Driest
Virginia Polytechnic Institute and University
Department of Aerospace Engineering
Blacksburg, Virginia 24061

Commander
Boston Naval Shipyard
Boston, Massachusetts 02129

Director
Office of Naval Research Branch Office
495 Summer Street
Boston, Massachusetts 02210

Commander
Puget Sound Naval Shipyard
Bremerton, Washington 98314

Professor J.J. Foody
Chairman, Engineering Department
State University of New York
Maritime College
Bronx, New York 10465

Dr. Alfred Ritter
Assistant Head, Applied Mechanics Department
Cornell Aeronautical Laboratory, Inc.
Buffalo, New York 14221

Dr. J.W. Morris
Manager, Material Sciences Section
Advanced Materials Research
Bell Aerospace Company
P.O. Box 1
Buffalo, New York 14240

Professor G.H. Carrier
Department of Engineering and Applied Physics
Harvard University
Cambridge, Massachusetts 02138

Commanding Officer
NROTC Naval Administrative Unit
Massachusetts Institute of Technology
Cambridge, Massachusetts 02139

Professor M.A. Abkowitz
Department of Naval Architecture and Marine Engineering
Massachusetts Institute of Technology
Cambridge, Massachusetts 02139

Professor A.T. Ippen
Department of Civil Engineering
Massachusetts Institute of Technology
Cambridge, Massachusetts 02139

Professor L.N. Howard
Department of Mathematics
Massachusetts Institute of Technology
Cambridge, Massachusetts 02139

Professor E.W. Merrill
Department of Mathematics
Massachusetts Institute of Technology
Cambridge, Massachusetts 02139

Professor E. Mollo-Christensen
Room 54-1722
Massachusetts Institute of Technology
Cambridge, Massachusetts 02139

Professor N. Newman
Department of Naval Architecture and Marine Engineering
Massachusetts Institute of Technology
Cambridge, Massachusetts 02139

Professor A.H. Shapiro
Department of Mechanical Engineering
Massachusetts Institute of Technology
Cambridge, Massachusetts 02139

Commander
Charleston Naval Shipyard
U.S. Naval Base
Charleston, South Carolina 29408

A.R. Kuhlthau, Director
Research Laboratories for the Engineering Sciences
Thorton Hall, University of Virginia
Charlottesville, Virginia 22903

Director
Office of Naval Research Branch Office
536 South Clark Street
Chicago, Illinois 60605

Library
Naval Weapons Center
China Lake, California 93555

Professor J.M. Burgers
Institute of Fluid Dynamics and Applied Mathematics
University of Maryland
College Park, Maryland 20742

Professor Pai
Institute for Fluid Dynamics and Applied Mathematics
University of Maryland
College Park, Maryland 20740

Acquisition Director
NASA Scientific & Technical Information
P.O. Box 33
College Park, Maryland 20740

Technical Library
Naval Weapons Laboratory
Dahlgren, Virginia 22448

Computation & Analyses Laboratory
Naval Weapons Laboratory
Dahlgren, Virginia 22448

Dr. C.S. Wells, Jr.
Manager - Fluid Mechanics
Advanced Technology Center, Inc.
P.O. Box 6144
Dallas, Texas 75222

Dr. R.H. Kraichnan
Dublin, New Hampshire 03444

Commanding Officer
Army Research Office
Box CM, Duke Station
Durham, North Carolina 27706

Professor A. Charnes
The Technological Institute
Northwestern University
Evanston, Illinois 60201

Dr. Martin H. Bloom
Polytechnic Institute of Brooklyn
Graduate Center, Dept. of Aerospace
Engineering and Applied Mechanics
Farmingdale, New York 11735

Technical Documents Center
Building 315
U.S. Army Mobility Equipment
Research and Development Center
Fort Belvoir, Virginia 22060

Professor J.E. Cermak
College of Engineering
Colorado State University
Ft. Collins, Colorado 80521

Technical Library
Webb Institute of Naval Architecture
Glen Cove, Long Island, New York 11542

Professor E.V. Lewis
Webb Institute of Naval Architecture
Glen Cove, Long Island, New York 11542

Dr. B.N. Pridmore Brown
Northrop Corporation
NORAIR-Div.
Hawthorne, California 90250

Dr. J.P. Breslin
Stevens Institute of Technology
Davidson Laboratory
Hoboken, New Jersey 07030

Dr. D. Savitsky
Stevens Institute of Technology
Davidson Laboratory
Hoboken, New Jersey 07030

Mr. C.H. Henry
Stevens Institute of Technology
Davidson Laboratory
Hoboken, New Jersey 07030

Dr. J.P. Craven
University of Hawaii
1801 University Avenue
Honolulu, Hawaii 96822

Professor E.L. Resler
Graduate School of Aeronautical Engineering
Cornell University
Ithaca, New York 14851

Professor John Miles
c/o I.G.P.P.
University of California, San Diego
La Jolla, California 92038

Director
Scrippe Institution of Oceanography
University of California
La Jolla, California 92037

Professor A. Ellis
University of California, San Diego
Department of Aerospace & Mechanical Engineering
La Jolla, California 92037

Dr. B. Sternlicht
Mechanical Technology Incorporated
968 Albany-Shaker Road
Latham, New York 12110

Dr. Coda Pan
Mechanical Technology Incorporated
968 Albany-Shaker Road
Latham, New York 12110

Mr. P. Eisenberg, President
Hydronautics, Inc.
Pindell School Road
Howard County
Laurel, Maryland 20810

Mr. M.P. Tulin
Hydronautics, Inc.
Pindell School Road
Howard County
Laurel, Maryland 20810

Mr. Alfonso Alcedan L.,Director
Laboratorio Nacional De Hydraulics
Antigui Cameno A. Ancon
Casilla Jostal 682
Lima, Peru

Commander
Long Beach Naval Shipyard
Long Beach, California 90802

Professor John Laufer
Department of Aerospace Engineering
University Park
Los Angeles, California 90007

Professor J.M. Killen
St. Anthony Falls Hydraulic Lab.
University of Minnesota
Minneapolis, Minnesota 55414

Lorenz G. Straub Library
St. Anthony Falls Hydraulic Lab.
Mississippi River at 3rd Avenue S.E.
Minneapolis, Minnesota 55414

Professor J. Ripkin
St. Anthony Falls Hydraulic Lab.
University of Minnesota
Minneapolis, Minnesota 55414

Dr. W. Silberman
St. Anthony Falls Hydraulic Lab.
Mississippi River at 3rd Avenue S.E.
Minneapolis, Minnesota 55414

Superintendent
Naval Postgraduate School
Library Code 0212
Monterey, California 93940

Professor A.B. Metzner
University of Delaware
Newark, New Jersey 19711

Technical Library
Naval Underwater Systems Center
Newport, Rhode Island 02840

Professor Dudley D. Fuller
Department of Mechanical Engineering
Columbia University
New York, New York 10027

Professor V. Castelli
Department of Mechanical Engineering
Columbia University
New York, New York 10027

Professor H. Elrod
Department of Mechanical Engineering
Columbia University
New York, New York 10027

Professor J.J. Stoker
Institute of Mathematical Sciences
New York University
251 Mercer Street
New York, New York 10003

Society of Naval Architects and Marine Engineering
74 Trinity Place
New York, New York 10006

Engineering Societies Library
345 East 47th Street
New York, New York 10017

Office of Naval Research
New York Area Office
207 W. 24th Street
New York, New York 10011

Miss O.M. Leach, Librarian
National Research Council
Aeronautical Library
Montreal Road
Ottawa 7, Canada

Technical Library
Naval Ship Research and Development Center
Panama City, Florida 32401

Technical Library
Naval Undersea R & D Center
Pasadena Laboratory
3202 E. Foothill Boulevard
Pasadena, California 91107

Dr. Andrew Fabula
Naval Undersea Research & Development Center
Pasadena Laboratory
3202 E. Foothill Boulevard
Pasadena, California 91107

Dr. J.W. Hoyt
Naval Undersea R & D Center
Pasadena Laboratory
3202 E. Foothill Boulevard
Pasadena, California 91107

Professor A. Acosta
Department of Mechanical Engineering
California Institute of Technology
Pasadena, California 91109

Professor H. Liepmann
Department of Aeronautics
California Institute of Technology
Pasadena, California 91109

Professor M.S. Plesset
Engineering Division
California Institute of Technology
Pasadena, California 91109

Professor A. Roshko
California Institute of Technology
Pasadena, California 91109

Professor T.Y. Wu
Department of Engineering
California Institute of Technology
Pasadena, California 91109

Director
Office of Naval Research Branch Office
1030 E. Green Street
Pasadena, California 91101

Naval Ship Engineering Center
Philadelphia Division
Technical Library
Philadelphia, Pennsylvania 19112

Technical Library
Philadelphia Naval Shipyard
Philadelphia, Pennsylvania 19112

Professor R.C. Mac Camy
Department of Mathematics
Carnegie Institute of Technology
Pittsburgh, Pennsylvania 15213

Dr. Paul Kaplan
Oceanics, Inc.
Plainview, Long Island, New York 11803

Technical Library
Naval Missile Center
Point Mugu, California 93441

Technical Library
Naval Civil Engineering Laboratory
Port Hueneme, California 93041

Commander
Portsmouth Naval Shipyard
Portsmouth, New Hampshire 03801

Commander
Norfolk Naval Shipyard
Portsmouth, Virginia 23709

Professor F.E. Bisshopp
Division of Engineering
Brown University
Providence, Rhode Island 02912

Dr. William A. Gross, Vice President
Ampex Corporation
401 Broadway
Redwood City, California 94063

Dr. H.N. Abramson
Southwest Research Institute
8500 Culebra Road
San Antonio, Texas 78228

Editor
Applied Mechanics Review
Southwest Research Institute
8500 Culebra Road
San Antonio, Texas 78206

Office of Naval Research
San Francisco Area Office
50 Fell Street
San Francisco, California 94102

Library
Pearl Harbor Naval Shipyard
Box 400
FPO San Francisco, California 96610

Technical Library
Hunters Point Naval Shipyard
San Francisco, California 94135

Librarian
Naval Ordnance Laboratory
White Oak
Silver Spring, Maryland 20910

Fenton Kennedy Document Library
The Johns Hopkins University
Applied Physics Laboratory
8621 Georgia Avenue
Silver Spring, Maryland 20910

Professor E.Y. Hsu
Department of Civil Engineering
Stanford University
Stanford, California 94305

Dr. Byrne Perry
Department of Civil Engineering
Stanford University
Stanford, California 94305

Dr. R.L. Street
Department of Civil Engineering
Stanford University
Stanford, California 94305

Professor Milton Van Dyke
Department of Aeronautical Engineering
Stanford University
Stanford, California 94305

Professor R.C. Di Prima
Department of Mathematics
Rensselaer Polytechnic Institute
Troy, New York 12180

Professor J. Lumley
Ordnance Research Laboratory
Pennsylvania State University
University Park, Pennsylvania 16801

Dr. M. Sevik
Ordnance Research Laboratory
Pennsylvania State University
University Park, Pennsylvania 16801

Dr. J.M. Robertson
Department of Theoretical and Applied Mechanics
University of Illinois
Urbana, Illinois 61803

Technical Library
Mare Island Naval Shipyard
Vallejo, California 94592

Code 438
Office of Naval Research
Department of the Navy
Arlington, Virginia 22217 (3)

Code 461
Office of Naval Research
Department of the Navy
Arlington, Virginia 22217

Code 463
Office of Naval Research
Department of the Navy
Arlington, Virginia 22217

Code 472
Office of Naval Research
Department of the Navy
Arlington, Virginia 22217

Code 468
Office of Naval Research
Department of the Navy
Arlington, Virginia 22217

Code 473
Office of Naval Research
Department of the Navy
Arlington, Virginia 22217

Code 481
Office of Naval Research
Department of the Navy
Arlington, Virginia 22217

Code 2627
Naval Research Laboratory
Washington, D.C. 20390 (6)

Library, Code 2620 (ONRL)
Naval Research Laboratory
Washington, D.C. 20390 (6)

Code 6170
Naval Research Laboratory
Washington, D.C. 20390

Code 4000
Director of Research
Naval Research Laboratory
Washington, D.C. 20390

Code 8030 (Maury Center)
Naval Research Laboratory
Washington, D.C. 20390

Code 8040
Naval Research Laboratory
Washington, D.C. 20390

Code 031
Naval Ship Systems Command
Washington, D.C. 20390

Code 0341
Naval Ship Systems Command
Washington, D.C. 20390

Code 03412B (L. Benen)
Naval Ship Systems Command
Washington, D.C. 20390

Code 03412 (J. Schuler)
Naval Ship Systems Command
Washington, D.C. 20390

Code 2052
Naval Ship Systems Command
Washington, D. C. 20390

Code 6034
Naval Ship Engineering Center
Center Building
Prince George's Center
Hyattsville, Maryland 20782

Code 6110
Naval Ship Engineering Center
Center Building
Prince George's Center
Hyattsville, Maryland 20782

Code 6113
Naval Ship Engineering Center
Center Building
Prince George's Center
Hyattsville, Maryland 20782

Code 6114
Naval Ship Engineering Center
Center Building
Prince George's Center
Hyattsville, Maryland 20782

Code 6120E
Naval Ship Engineering Center
Center Building
Prince George's Center
Hyattsville, Maryland 20782

Code 6136
Naval Ship Engineering Center
Center Building
Prince George's Center
Hyattsville, Maryland 20782

Dr. A. Powell
Code 01
Naval Ship Research and Development Center
Washington, D.C. 20034

Mr. W.M. Ellsworth
Code 0H50
Naval Ship Research and Development Center
Washington, D.C. 20034

Central Library
Code L42
Naval Ship Research and Development Center
Washington, D.C. 20034

Dr. W.E. Cummins
Code 500
Naval Ship Research and Development Center
Washington, D.C. 20034

Mr. S.F. Crump
Code 513
Naval Ship Research and Development Center
Washington, D.C. 20034

Mr. R. Wermter
Code 520
Naval Ship Research and Development Center
Washington, D.C. 20034

Dr. P. Pien
Code 521
Naval Ship Research and Development Center
Washington, D.C. 20034

Dr. W.B. Morgan
Code 540
Naval Ship Research and Development Center
Washington, D.C. 20034

Mr. P. Granville
Code 541
Naval Ship Research and Development Center
Washington, D.C. 20034

Mr. J.B. Hadler
Code 560
Naval Ship Research and Development Center
Washington, D.C. 20034

Dr. H.R. Chaplin
Code 600
Naval Ship Research and Development Center
Washington, D.C. 20034

Mr. G.H. Gleissner
Code 800
Naval Ship Research and Development Center
Washington, D.C. 20034

Dr. M. Strasberg
Code 901
Naval Ship Research and Development Center
Washington, D.C. 20034

Mr. J. McCarthy
Code 552
Naval Ship Research and Development Center
Washington, D.C. 20034

Code 03
Naval Air Systems Command
Washington, D.C. 20360

AIR 5301
Naval Air Systems Command
Department of the Navy
Washington, D.C. 20360

Code ORD 03
Naval Ordnance Systems Command
Washington, D.C. 20360

Code ORD 035
Naval Ordnance Systems Command
Washington, D.C. 20360

Code ORD 05413
Naval Ordnance Systems Command
Washington, D.C. 20360

Code ORD 9132
Naval Ordnance Systems Command
Washington, D.C. 20360

Oceanographer of the Navy
Washington, D.C. 20390

Commander
Naval Oceanographic Office
Washington, D.C. 20390

Chief Scientist (CNM PM-1)
Strategic Systems Project Office
Department of the Navy
Washington, D.C. 20360

Technical Division (CNM PM 11-20)
Deep Submergence Systems Project Office
Department of the Navy
Washington, D.C. 20360

Dr. A.L. Slafkosky
Scientific Advisor
Commandant of the Marine Corps (Code AX)
Washington, D.C. 20380

Librarian Station 5-2
Coast Guard Headquarters
NASSIF Building
400 7th Street, S.W.
Washington, D.C. 20591

Office of Research and Development
Maritime Administration
441 G. Street, N.W.
Washington, D.C. 20235

Division of Ship Design
Maritime Administration
441 G. Street, N.W.
Washington, D.C. 20235

National Science Foundation
Engineering Division
1800 G. Street, N.W.
Washington, D.C. 20550

Dr. G. Kulin
National Bureau of Standards
Washington, D.C. 20234

Science & Technology Division
Library of Congress
Washington, D.C. 20540

Chief of Research & Development
Office of Chief of Staff
Department of the Army
The Pentagon, Washington, D.C. 20310

Professor A. Thiruvengadam
Department of Mechanical Engineering
The Catholic University of America
Washington, D.C. 20017

Professor G. Birkhoff
Department of Mathematics
Harvard University
Cambridge, Massachusetts 02138

AIR 604
Naval Air Systems Command
Department of the Navy
Washington, D.C. 20360

Dr. A.S. Iberall, President
General Technical Services, Inc.
451 Penn Street
Yeadon, Pennsylvania 19050

Professor J.F. Kennedy, Director
Iowa Institute of Hydraulic Research
State University of Iowa
Iowa City, Iowa 52240

Professor L. Landweber
Iowa Institute of Hydraulic Research
State University of Iowa
Iowa City, Iowa 52240

Dr. Lee Segel
Department of Mathematics
Rensselaer Polytechnic Institute
Troy, New York 12180

Code 6101E
Naval Ship Engineering Center
Center Building
Prince George's Center
Hyattsville, Maryland 20782